



Copernicus Global Land Operations - Scientific quality evaluation cross-cutting consistency - January-December 2019

Jean-Christophe Calvet, Clément Albergel, Bertrand Bonan, Catherine Meurey, Yongjun Zheng

► To cite this version:

Jean-Christophe Calvet, Clément Albergel, Bertrand Bonan, Catherine Meurey, Yongjun Zheng. Copernicus Global Land Operations - Scientific quality evaluation cross-cutting consistency - January-December 2019. CGLOPS Lot 1 consortium. 2020. meteo-04168132

HAL Id: meteo-04168132

<https://meteofrance.hal.science/meteo-04168132v1>

Submitted on 21 Jul 2023

HAL is a multi-disciplinary open access archive for the deposit and dissemination of scientific research documents, whether they are published or not. The documents may come from teaching and research institutions in France or abroad, or from public or private research centers.

L'archive ouverte pluridisciplinaire **HAL**, est destinée au dépôt et à la diffusion de documents scientifiques de niveau recherche, publiés ou non, émanant des établissements d'enseignement et de recherche français ou étrangers, des laboratoires publics ou privés.

Copernicus Global Land Operations

“Vegetation and Energy”

”CGLOPS-1”

Framework Service Contract N° 199494 (JRC)

SCIENTIFIC QUALITY EVALUATION

CROSS-CUTTING CONSISTENCY

JANUARY - DECEMBER 2019



ISSUE I1.00

Organization name of lead contractor for this deliverable: Meteo-France

Book Captain:	Jean-Christophe Calvet (Meteo-France)
Contributing authors:	Clément Albergel (Meteo-France)
	Bertrand Bonan (Meteo-France)
	Catherine Meurey (Meteo-France)
	Yongjun Zheng (Meteo-France)

Dissemination Level		
PU	Public	X
PP	Restricted to other programme participants (including the Commission Services)	
RE	Restricted to a group specified by the consortium (including the Commission Services)	
CO	Confidential, only for members of the consortium (including the Commission Services)	

DOCUMENT RELEASE SHEET

Book Captain:	J.-C. Calvet	Date: 13.03.2020	Sign. 
Approval:	R. Lacaze	Date: 22.04.2020	Sign. 
Endorsement:	M. Cherlet	Date:	Sign.
Distribution:	Public		

CHANGE RECORD

Issue/Revision	Date	Page(s)	Description of Change	Release
	13.03.2020	All	Final version	I1.00

TABLE OF CONTENT

<i>Executive Summary</i>	20
<i>1 Background</i>	22
1.1 Scope and Objectives	22
1.2 Content of the Document	22
1.3 Related Documents	22
1.3.1 Applicable documents	22
1.3.2 Input documents	22
<i>2 Methods</i>	24
2.1 LDAS-Monde.....	24
2.2 Input products	25
2.3 Evaluation Metrics.....	27
2.3.1 Scores	27
2.3.2 Increments	28
<i>3 Results at a global scale</i>	30
<i>4 Results for LAI V1</i>	34
<i>5 Results for FAPAR V1</i>	44
<i>6 Results for Surface Albedo</i>	53
<i>7 Results for SWI-001</i>	62
<i>8 Results for LST</i>	80
<i>9 LDAS statistics</i>	107
9.1 Increments and impacts of the assimilation on water and carbon fluxes	107
9.2 Transition between SPOT-VGT and PROBA-V	118
9.3 LAI Version 1 (GEOV1) vs. LAI Version 2 (GEOV2).....	121
9.4 Accuracy assessment.....	123
9.5 Number of observations.....	128
<i>10 Conclusions</i>	131
<i>11 References</i>	133

LIST OF FIGURES

<i>Figure 1: Mean observed LAI for 2010-2019 (top) at a global scale, model open-loop vs. observation RMSD (middle), analysis vs. observation RMSD (bottom).</i>	31
<i>Figure 2: Continental potential hot spots for droughts and heat waves at a global scale. Regions considered in this report affected by severe conditions in 2019 are indicated: Southern Africa, and the Murray-Darling basin in Australia.</i>	32
<i>Figure 3: Mean observed monthly (left) SSM and (right) LAI values in 2019 with respect to the minimum, mean and maximum values from 2010 to 2018 over (top) Southern Africa ("SAFR") and (bottom) the Murray-Darling basin ("MUDA").</i>	33
<i>Figure 4: Monthly average values of LAI over Southern Africa at 0.25° spatial resolution from January (top) to June 2019 (bottom). From left to right: model, satellite product, analysis, analysis-model difference. The latter shows the impact of assimilating LAI and SWI-001 on the simulated LAI. The color scale range of LAI values is 0 to 1.5 m²m⁻². Areas with vegetation cover fraction less than 0.1 are left blank.</i>	34
<i>Figure 5: Monthly average values of LAI over Southern Africa at 0.25° spatial resolution July (top) to December 2019 (bottom). From left to right: model, satellite product, analysis, analysis-model difference. The latter shows the impact of assimilating LAI and SWI-001 on the simulated LAI. The color scale range of LAI values is 0 to 1.5 m²m⁻². Areas with vegetation cover fraction less than 0.1 are left blank.</i>	35
<i>Figure 6: Monthly average values of LAI over the Murray-Darling basin at 0.25° spatial resolution from January (top) to June 2019 (bottom). From left to right: model, satellite product, analysis, analysis-model difference. The latter shows the impact of assimilating LAI and SWI-001 on the simulated LAI. The color scale range of LAI values is 0 to 1.5 m²m⁻². Areas with vegetation cover fraction less than 0.1 are left blank.</i>	36
<i>Figure 7: Monthly average values of LAI over the Murray-Darling basin at 0.25° spatial resolution from July (top) to December 2019 (bottom). From left to right: model, satellite product, analysis, analysis-model difference. The latter shows the impact of assimilating LAI and SWI-001 on the simulated LAI. The color scale range of LAI values is 0 to 1.5 m²m⁻². Areas with vegetation cover fraction less than 0.1 are left blank.</i>	37
<i>Figure 8: Monthly average values over Southern Africa of LAI (top) and root-zone soil moisture (bottom) from 1 January 2010 to 31 December 2019: model (blue line), satellite product (green circles), analysis (red line). Analysis-Model differences show the impact of assimilating LAI and SWI-001 on the simulated LAI and root-zone soil moisture.</i>	38

Figure 9: Monthly average values over the Murray-Darling basin of LAI (top) and root-zone soil moisture (bottom) from 1 January 2010 to 31 December 2019: model (blue line), satellite product (green circles), analysis (red line). Analysis-Model differences show the impact of assimilating LAI and SWI-001 on the simulated LAI and root-zone soil moisture.39

Figure 10: Monthly LAI scores of the model (blue) and analysis (red) when compared to the observations over Southern Africa at 0.25° spatial resolution: from 2010 to 2018 (dashed lines), with N ranging from 27,274 in December to 28,323 in January-March, August-November; and for 2019 (solid lines), with N ranging from 3,101 in July to 3,122 in January. The monthly N values are indicated in the legend Table. Analysis-Model differences show the impact of assimilating LAI and SWI-001 on the simulated LAI. Shaded areas are between minimum and maximum score values recorded from 2010 to 2018.40

Figure 11: Monthly LAI scores of the model (blue) and analysis (red) when compared to the observations over the Murray-Darling basin at 0.25° spatial resolution: from 2010 to 2018 (dashed lines), with N ranging from 45,149 in December to 46,892 in October; and for 2019 (solid lines), with N ranging from 5,074 in June to 5,203 in January. The monthly N values are indicated in the legend Table. Analysis-Model differences show the impact of assimilating LAI and SWI-001 on the simulated LAI. Shaded areas are between minimum and maximum score values recorded from 2010 to 2018. ..41

Figure 12: Monthly average values of FAPAR over Southern Africa at 0.25° spatial resolution from January (top) to June 2019 (bottom). From left to right: model, satellite product, analysis, analysis-model difference. The latter shows the impact of assimilating LAI and SWI-001 on the simulated FAPAR. The color scale range of FAPAR values is 0 to 1.0. Areas with vegetation cover fraction less than 0.1 are left blank.44

Figure 13: Monthly average values of FAPAR over Southern Africa at 0.25° spatial resolution July (top) to December 2019 (bottom). From left to right: model, satellite product, analysis, analysis-model difference. The latter shows the impact of assimilating LAI and SWI-001 on the simulated FAPAR. The color scale range of FAPAR values is 0 to 1.0. Areas with vegetation cover fraction less than 0.1 are left blank.45

Figure 14: Monthly average values of FAPAR over the Murray-Darling basin at 0.25° resolution January (top) to June 2019 (bottom). From left to right: model, satellite product, analysis, analysis-model difference. The latter shows the impact of assimilating LAI and SWI-001 on the simulated FAPAR. The color scale range of FAPAR values is 0 to 1.0. Areas with vegetation cover fraction less than 0.1 are left blank.46

Figure 15: Monthly average values of FAPAR over the Murray-Darling basin at 0.25° resolution July (top) to December 2019 (bottom). From left to right: model, satellite product, analysis, analysis-model difference. The latter shows the impact of assimilating LAI and SWI-001 on the simulated FAPAR. The color scale range of FAPAR values is 0 to 1.0. Areas with vegetation cover fraction less than 0.1 are left blank.47

<i>Figure 16: Monthly average values of FAPAR over Southern Africa (top) from 2010 to 2018, the Murray-Darling basin (bottom) from 2010 to 2018: model (blue line), satellite product (green circles), analysis (red line). Analysis-Model differences show the impact of assimilating LAI and SWI-001 on the simulated FAPAR.</i>	48
<i>Figure 17: Monthly FAPAR scores of the model (blue) and analysis (red) when compared to the observations over Southern Africa at a 0.25° spatial resolution: from 2010 to 2018 (dashed lines), with N ranging from 28,315 in June to 28,323 in January-April, August-December; and for 2019 (solid lines), with N ranging from 3,145 in June to 3,150 in January, February, September-December. The monthly N values are indicated in the legend Table. Analysis-Model differences show the impact of assimilating LAI and SWI-001 on the simulated FAPAR. Shaded areas are between minimum and maximum score values recorded from 2010 to 2018.</i>	49
<i>Figure 18: Monthly FAPAR scores of the model (blue) and analysis (red) when compared to the observations over the Murray-Darling basin at 0.25° spatial resolution: from 2010 to 2018 (dashed lines), with N ranging from 46,630 in July to 46,893 in November; and for 2019 (solid lines), with N ranging from 5,164 in July to 5,211 in November. The monthly N values are indicated in the legend Table. Analysis-Model differences show the impact of assimilating LAI and SWI-001 on the simulated FAPAR. Shaded areas are between minimum and maximum score values recorded from 2010 to 2018.</i>	50
<i>Figure 19: Monthly average values of Surface Albedo over Southern Africa at 0.25° spatial resolution from January (top) to June 2019 (bottom). From left to right: model, satellite product, analysis, analysis-model difference. The latter shows the impact of assimilating LAI and SWI-001 on the simulated SA. The color scale range of SA values is 0 to 0.5. Areas with missing data are left blank.</i>	53
<i>Figure 20: Monthly average values of Surface Albedo over Southern Africa at 0.25° spatial resolution from July (top) to December 2019 (bottom). From left to right: model, satellite product, analysis, analysis-model difference. The latter shows the impact of assimilating LAI and SWI-001 on the simulated SA. The color scale range of SA values is 0 to 0.5. Areas with missing data are left blank.</i>	54
<i>Figure 21: Monthly average values of Surface albedo over the Murray-Darling basin at 0.25° spatial resolution from January (top) to June 2019 (bottom). From left to right: model, satellite product, analysis, analysis-model difference. The latter shows the impact of assimilating LAI and SWI-001 on the simulated SA. The color scale range of SA values is 0 to 0.5. Areas with missing data are left blank.</i>	55
<i>Figure 22: Monthly average values of Surface albedo over the Murray-Darling basin at 0.25° spatial resolution from July (top) to December 2019 (bottom). From left to right: model, satellite product, analysis, analysis-model difference. The latter shows the impact of assimilating LAI and SWI-001 on the simulated SA. The color scale range of SA values is 0 to 0.5. Areas with missing data are left blank.</i>	56

Figure 23: Monthly average values of SA over Southern Africa (top) from 2010 to 2019, the Murray-Darling basin (bottom) from 2010 to 2019: model (blue line), satellite product (green circles), analysis (red line). Analysis-Model differences show the impact of assimilating LAI and SWI-001 on the simulated SA. (Note that model and analysis curves are often superimposed).	57
Figure 24: Monthly SA scores of the model (blue) and analysis (red) when compared to the observations over Southern Africa at a 0.25° spatial resolution: from 2010 to 2018 (dashed lines), with N ranging from 27,291 in January to 30,750 in September; and for January to December 2019 (solid lines), with N ranging from 2,686 in June to 3,490 in February. The monthly N values are indicated in the legend Table. Analysis-Model differences show the impact of assimilating LAI and SWI-001 on the simulated SA. (Note that model and analysis curves are nearly completely superimposed).	58
Figure 25: Monthly SA scores of the model (blue) and analysis (red) when compared to the observations over the Murray-Darling basin at 0.25° spatial resolution: from 2010 to 2018 (dashed lines), with N ranging from 36,703 in December to 42,707 in April; and for January to December 2019 (solid lines), with N ranging from 1,357 in June to 2,828 in December. The monthly N values are indicated in the legend Table. Analysis-Model differences show the impact of assimilating LAI and SWI-001 on the simulated SA. (Note that model and analysis curves are often superimposed).	59
Figure 26: Monthly average values of SSM over Southern Africa at 0.25° spatial resolution from January (top) to June 2019 (bottom). From left to right: model, rescaled satellite product after CDF matching, analysis, analysis-model difference. The latter shows the impact of assimilating LAI and SWI-001 on the simulated SSM. The color scale range of SSM values is 0 to 0.3 m ³ m ⁻³	62
Figure 27: Monthly average values of SSM over Southern Africa at 0.25° spatial resolution from July (top) to December 2019 (bottom). From left to right: model, rescaled satellite product after CDF matching, analysis, analysis-model difference. The latter shows the impact of assimilating LAI and SWI-001 on the simulated SSM. The color scale range of SSM values is 0 to 0.3 m ³ m ⁻³	63
Figure 28: Monthly average values of SSM over the Murray-Darling basin at 0.25° spatial resolution from January (top) to June 2019 (bottom). From left to right: model, rescaled satellite product after CDF matching, analysis, analysis-model difference. The latter shows the impact of assimilating LAI and SWI-001 on the simulated SSM. The color scale range of SSM values is 0 to 0.3 m ³ m ⁻³ . Areas with missing data are left blank.	64
Figure 29: Monthly average values of SSM over the Murray-Darling basin at 0.25° spatial resolution from July (top) to December 2019 (bottom). From left to right: model, rescaled satellite product after CDF matching, analysis, analysis-model difference. The latter shows the impact of assimilating LAI and SWI-001 on the simulated SSM. The color scale range of SSM values is 0 to 0.3 m ³ m ⁻³ . Areas with missing data are left blank.	65
Figure 30: Monthly correlation maps between the rescaled SWI-001 product time series after CDF matching and the modeled SSM (left), and the analyzed SSM (middle) over Southern Africa at 0.25°	

<i>spatial resolution from January (top) to June 2019 (bottom). Analysis-Model differences show the impact of assimilating LAI and SWI-001 on the simulated SSM. The color scale range of R values is -1.0 to 1.0.....</i>	66
<i>Figure 31: Monthly correlation maps between the rescaled SWI-001 product time series after CDF matching and the modeled SSM (left), and the analyzed SSM (middle) over Southern Africa at 0.25° spatial resolution from July (top) to December 2019 (bottom). Analysis-Model differences show the impact of assimilating LAI and SWI-001 on the simulated SSM. The color scale range of R values is -1.0 to 1.0.....</i>	67
<i>Figure 32: Monthly correlation maps between the rescaled SWI-001 product time series after CDF matching and the modeled SSM (left), and the analyzed SSM (middle) over the Murray-Darling basin at 0.25° spatial resolution from January (top) to June 2019 (bottom). Analysis-Model differences show the impact of assimilating LAI and SWI-001 on the simulated SSM. The color scale range of R values is -1.0 to 1.0. Areas with missing data are left blank.</i>	68
<i>Figure 33: Monthly correlation maps between the rescaled SWI-001 product time series after CDF matching and the modeled SSM (left), and the analyzed SSM (middle) over the Murray-Darling basin at 0.25° spatial resolution from July (top) to December 2019 (bottom). Analysis-Model differences show the impact of assimilating LAI and SWI-001 on the simulated SSM. The color scale range of R values is -1.0 to 1.0. Areas with missing data are left blank.</i>	69
<i>Figure 34: Yearly correlation maps between the rescaled SWI-001 product time series after CDF matching and the modeled SSM (left), and the analyzed SSM (middle) over Southern Africa at 0.25° resolution from 2010 to 2019. Analysis-Model differences show the impact of assimilating LAI and SWI-001 on the simulated SSM. The color scale range of R values is -1.0 to 1.0.</i>	70
<i>Figure 35: Yearly correlation maps between the rescaled SWI-001 product time series after CDF matching and the modeled SSM (left), and the analyzed SSM (middle) over the Murray-Darling basin at 0.25° resolution from 2010 to 2019. Analysis-Model differences show the impact of assimilating LAI and SWI-001 on the simulated SSM. The color scale range of R values is -1.0 to 1.0. Areas with missing data are left blank.</i>	71
<i>Figure 36: Monthly average values of SSM over Southern Africa from 2010 to 2019. Top panel: original SWI-001 (red), model SSM used for CDF-matching (blue), rescaled SWI-001 product (green). Bottom panel: model (blue, same as on the top graph), rescaled SWI-001 product (green), analysis (red). Analysis-Model differences show the impact of assimilating LAI and SWI-001 on the simulated SSM.</i>	72
<i>Figure 37: Monthly average values of SSM over the Murray-Darling basin from 2010 to 2019. Top panel: original SWI-001 (red), model SSM used for CDF-matching (blue), rescaled SWI-001 product (green). Bottom panel: model (blue, same as on the top graph), rescaled SWI-001 observations (green), analysis (red). Analysis-Model differences show the impact of assimilating LAI and SWI-001 on the simulated SSM.</i>	73

Figure 38: Monthly SSM scores of the model (blue) and analysis (red) when compared to the rescaled SWI-001 over Southern Africa at 0.25° spatial resolution: for all data from 2010 to 2018 (dashed lines), with N ranging from 39,163 in January to 2,448,876 in August, and for data in 2019 (solid lines), with N ranging from 1,530 in February to 41,868 in July. The monthly N values are indicated in the legend Table. Analysis-Model differences show the impact of assimilating LAI and SWI-001 on the simulated SSM. Shaded areas are between minimum and maximum score values recorded from 2010 to 2018.74

Figure 39: Monthly SSM scores of the model (blue) and analysis (red) when compared to the rescaled SWI-001 over the Murray-Darling basin at 0.25° spatial resolution: for all data from 2010 to 2018 (dashed lines), with N ranging from 118,513 in February to 169,957 in November, and for data in 2019 (solid lines), with N ranging from 39,454 in February to 44,720 in October. The monthly N values are indicated in the legend Table. Analysis-Model differences show the impact of assimilating LAI and SWI-001 on the simulated SSM. Shaded areas are between minimum and maximum score values recorded from 2010 to 2018.75

Figure 40: Annual scores of the model (blue) and analysis (red) when compared to the rescaled SWI-001 over Southern Africa at 0.25° spatial resolution, with N ranging from 140,118 in 2011 to 260,019 in 2019. The yearly N values are indicated in the legend Table. Analysis-Model differences show the impact of assimilating LAI and SWI-001 on the simulated SSM.....76

Figure 41: Annual scores of the model (blue) and analysis (red) when compared to the rescaled SWI-001 over the Murray-Darling basin at 0.25° spatial resolution, with N ranging from 82,588 in 2014 to 511,044 in 2018. The yearly N values are indicated in the legend Table. Analysis-Model differences show the impact of assimilating LAI and SWI-001 on the simulated SSM.77

Figure 42: Monthly average values of LST at 1200 UTC over Southern Africa at 0.25° spatial resolution from January to June 2019. From left to right: model, satellite product, analysis, analysis-model difference. The latter shows the impact of assimilating LAI and SWI-001 on the simulated LST. The color scale range of LST values is 0 to 60 °C.80

Figure 43: Monthly average values of LST at 1200 UTC over Southern Africa at 0.25° spatial resolution from July to December 2019. From left to right: model, satellite product, analysis, analysis-model difference. The latter shows the impact of assimilating LAI and SWI-001 on the simulated LST. The color scale range of LST values is 0 to 60 °C.81

Figure 44: Monthly average values of LST at 0600 UTC over Southern Africa at 0.25° spatial resolution from January to June 2019. From left to right: model, satellite product, analysis, analysis-model difference. The latter shows the impact of assimilating LAI and SWI-001 on the simulated LST. The color scale range of LST values is 0 to 60 °C.82

Figure 45: Monthly average values of LST at 0600 UTC over Southern Africa at 0.25° spatial resolution from July to December 2019. From left to right: model, satellite product, analysis, analysis-

<i>model difference. The latter shows the impact of assimilating LAI and SWI-001 on the simulated LST. The color scale range of LST values is 0 to 60 °C.</i>	83
<i>Figure 46: Monthly average values of LST at 0300 UTC (~noon) over the Murray-Darling basin at 0.25° spatial resolution from January to June 2019: model (left), satellite (middle) product, and analysis (right). Analysis-Model differences show the impact of assimilating LAI and SWI-001 on the simulated LST. The color scale range of LST values is 0 to 60 °C.</i>	84
<i>Figure 47: Monthly average values of LST at 0300 UTC (~noon) over the Murray-Darling basin at 0.25° spatial resolution from July to December 2019: model (left), satellite (middle) product, and analysis (right). Analysis-Model differences show the impact of assimilating LAI and SWI-001 on the simulated LST. The color scale range of LST values is 0 to 60 °C.</i>	85
<i>Figure 48: Monthly average values of LST at 2100 UTC (~dawn) over the Murray-Darling basin at 0.25° spatial resolution from January to June 2019: model (left), satellite (middle) product, and analysis (right). Analysis-Model differences show the impact of assimilating LAI and SWI-001 on the simulated LST. The color scale range of LST values is 0 to 60 °C.</i>	86
<i>Figure 49: Monthly average values of LST at 2100 UTC (~dawn) over the Murray-Darling basin at 0.25° spatial resolution from July to December 2019: model (left), satellite (middle) product, and analysis (right). Analysis-Model differences show the impact of assimilating LAI and SWI-001 on the simulated LST. The color scale range of LST values is 0 to 60 °C.</i>	87
<i>Figure 50: Monthly bias for LST at 1200 UTC over Southern Africa at 0.25° spatial resolution from January to December 2019. From left to right: model, analysis, analysis-model difference. The latter shows the impact of assimilating LAI and SWI-001 on the simulated LST. The color scale range of LST bias values is -15 to 15 °C.</i>	88
<i>Figure 51: Monthly bias for LST at 0600 UTC over Southern Africa at 0.25° spatial resolution from January to December 2019. From left to right: model, analysis, analysis-model difference. The latter shows the impact of assimilating LAI and SWI-001 on the simulated LST. The color scale range of LST bias values is -5.2 to 5.2 °C.</i>	89
<i>Figure 52: Monthly bias for LST at 0300 UTC (~noon) over the Murray-Darling basin at 0.25° spatial resolution from January to December 2019. From left to right: model, analysis, analysis-model difference. The latter shows the impact of assimilating LAI and SWI-001 on the simulated LST. The color scale range of LST bias values is -13 to 13 °C.</i>	90
<i>Figure 53: Monthly bias for LST at 2100 UTC (~dawn) over the Murray-Darling basin at 0.25° spatial resolution from January to December 2019. From left to right: model, analysis, analysis-model difference. The latter shows the impact of assimilating LAI and SWI-001 on the simulated LST. The color scale range of LST bias values is -5 to 5 °C.</i>	91

<i>Figure 54: Monthly correlation for LST at 1200 UTC over Southern Africa at 0.25° spatial resolution from January to December 2019. From left to right: model, analysis, analysis-model difference. The latter shows the impact of assimilating LAI and SWI-001 on the simulated LST.</i>	92
<i>Figure 55: Monthly correlation for LST at 0600 UTC over Southern Africa at 0.25° spatial resolution from January to December 2019. From left to right: model, analysis, analysis-model difference. The latter shows the impact of assimilating LAI and SWI-001 on the simulated LST.</i>	93
<i>Figure 56: Monthly correlation for LST at 0300 UTC (~noon) over the Murray-Darling basin at 0.25° spatial resolution from January to December 2019. From left to right: model, analysis, analysis-model difference. The latter shows the impact of assimilating LAI and SWI-001 on the simulated LST.</i>	94
<i>Figure 57: Monthly correlation for LST at 2100 UTC (~dawn) over the Murray-Darling basin at 0.25° spatial resolution from January to December 2019. From left to right: model, analysis, analysis-model difference. The latter shows the impact of assimilating LAI and SWI-001 on the simulated LST.</i>	95
<i>Figure 58: Monthly LST scores at 1200 UTC of the model (blue) and analysis (red) when compared to observations over Southern Africa at 0.25° spatial resolution: from 2010 to 2018 (dashed lines), with N ranging from 46,003 in December to 89,644 in March; and 2019 (solid lines), with N ranging from 3,518 in January to 15,793 in May. The monthly N values are indicated in the legend Table. Analysis-Model differences show the impact of assimilating LAI and SWI-001 on the simulated LST. Shaded areas are between minimum and maximum score values recorded from 2010 to 2018.</i>	96
<i>Figure 59: Monthly LST scores at 0600 UTC of the model (blue) and analysis (red) when compared to observations over Southern Africa at 0.25° spatial resolution: from 2010 to 2018 (dashed lines), with N ranging from 65,939 in November to 121,511 in March; and 2019 (solid lines), with N ranging from 4,617 in January to 23,143 in July. The monthly N values are indicated in the legend Table. Analysis-Model differences show the impact of assimilating LAI and SWI-001 on the simulated LST. Shaded areas are between minimum and maximum score values recorded from 2010 to 2018.</i>	97
<i>Figure 60: Monthly LST scores at 0300 UTC (~noon) of the model (blue) and analysis (red) when compared to observations over the Murray-Darling basin at 0.25° spatial resolution: from 2010 to 2018 (dashed lines), with N ranging from 244,461 in March to 312,367 in September; and 2019 (solid lines), with N ranging from 31,304 in December to 43,018 in August. The monthly N values are indicated in the legend Table. Analysis-Model differences show the impact of assimilating LAI and SWI-001 on the simulated LST. Shaded areas are between minimum and maximum score values recorded from 2010 to 2018.</i>	98
<i>Figure 61: Monthly LST scores at 2100 UTC (~dawn) of the model (blue) and analysis (red) when compared to observations over the Murray-Darling basin at 0.25° spatial resolution: from 2010 to 2018 (dashed lines), with N ranging from 286,934 in February to 367,991 in August; and 2019 (solid lines), with N ranging from 34,959 in January to 48,635 in August. The monthly N values are indicated in the legend Table. Analysis-Model differences show the impact of assimilating LAI and</i>	

<i>SWI-001 on the simulated LST. Shaded areas are between minimum and maximum score values recorded from 2010 to 2018.</i>	99
<i>Figure 62: LST 3-hourly bias of the analysis over Southern Africa at 0.25° spatial resolution from January to June from 2010 to 2018 (green line) and for 2019 (blue line).</i>	100
<i>Figure 63: LST 3-hourly bias of the analysis over Southern Africa at 0.25° spatial resolution from July to December from 2010 to 2018 (green line) and for 2019 (blue line).</i>	101
<i>Figure 64: LST 3-hourly bias of the analysis over the Murray-Darling basin at 0.25° spatial resolution from January to June from 2010 to 2018 (green line) and for 2019 (blue line). [Note that 0300 UTC is close to noon at these longitudes.]</i>	102
<i>Figure 65: LST 3-hourly bias of the analysis over the Murray-Darling basin at 0.25° spatial resolution from July to December from 2010 to 2018 (green line) and for 2019 (blue line). [Note that 0300 UTC is close to noon at these longitudes.]</i>	103
<i>Figure 66: Monthly maps over Southern Africa from January to June of LAI (1st column), root-zone soil moisture (2nd column) increments: averages over 2010–2018 (left), and for 2019 (right).</i>	107
<i>Figure 67: Monthly maps over Southern Africa from July to December of LAI (1st column), root-zone soil moisture (2nd column) increments: averages over 2010–2018 (left), and for 2019 (right).</i>	108
<i>Figure 68: Monthly maps over Southern Africa from January to June of the differences (Analysis-Model) for evapotranspiration (ET, 1st column) and drainage fluxes (2nd column): averages over 2010–2018 (left), and for 2019 (right).</i>	109
<i>Figure 69: Monthly maps over Southern Africa from July to December of the differences (Analysis-Model) for evapotranspiration (ET, 1st column) and drainage fluxes (2nd column): averages over 2010–2018 (left), and for 2019 (right).</i>	110
<i>Figure 70: Monthly maps over Southern Africa from January to December of the differences (Analysis-Model) for NEE (1st column), GPP (2nd column) and Reco fluxes (3rd column): averages over 2010–2018 (left), and for 2019 (right).</i>	111
<i>Figure 71: Monthly maps over the Murray-Darling basin from January to June of LAI (1st column), root-zone soil moisture (2nd column) increments: averages over 2010–2018 (left), and for 2019 (right).</i>	112
<i>Figure 72: Monthly maps over the Murray-Darling basin from July to December of LAI (1st column), root-zone soil moisture (2nd column) increments: averages over 2010–2018 (left), and for 2019 (right).</i>	113
<i>Figure 73: Monthly maps over the Murray-Darling basin from January to June of the differences (Analysis-Model) for evapotranspiration (ET, 1st column) and drainage fluxes (2nd column): averages over 2010–2018 (left), and for 2019 (right).</i>	114

<i>Figure 74: Monthly maps over the Murray-Darling basin from July to December of the differences (Analysis-Model) for evapotranspiration (ET, 1st column) and drainage fluxes (2nd column): averages over 2010–2018 (left), and for 2019 (right).</i>	115
<i>Figure 75: Monthly maps over the Murray-Darling basin from January to December of the differences (Analysis-Model) for NEE (1st column), GPP (2nd column) and Reco fluxes (3rd column): averages over 2010–2018 (left), and for 2019 (right).</i>	116
<i>Figure 76: RZSM and LAI mean increments which result from the assimilation of both SWI-001 and LAI observations over Southern Africa (top) from 2010 to 2019, over the Murray-Darling basin (bottom) from 2010 to 2019.</i>	117
<i>Figure 77: LAI scores for the time periods of SPOT-VGT observations over Southern Africa (top) (2010-2013, dashed lines) and the Murray-Darling basin (bottom) (2010-2013, dashed lines) and of PROBA-V observations (2015-2019, solid lines). Model performances are in blue and analysis performances are in red w.r.t. the appropriate observations. [NB: 2014 was not considered since it was the year of transition between the two instruments]</i>	119
<i>Figure 78: SA scores for the time periods of SPOT-VGT observations over Southern Africa (top) (2010-2013, dashed lines) and the Murray-Darling basin (bottom) (2010-2013, dashed lines) and of PROBA-V observations (2015-2019, solid lines). Model performances are in blue and analysis performances are in red w.r.t. the appropriate observations. [NB: 2014 was not considered since it was the year of transition between the two instruments]</i>	120
<i>Figure 79: LAI GEOV2 vs. GEOV1 yearly RMSD score over Southern Africa for each year from 2010 to 2019, in m²m⁻². Year 2019 is indicated.</i>	121
<i>Figure 80: LAI GEOV2 vs. GEOV1 yearly RMSD score over the Murray-Darling basin for each year from 2010 to 2019, in m²m⁻². Year 2019 is indicated.</i>	122
<i>Figure 81: Relative analysis RMSD (RMSD divided by value) (top) and analysis RMSD (bottom) of LAI (left) and FAPAR (right) on average over Southern Africa. Dashed red line indicates the target accuracies: max(20%,0.5) for LAI and max(10%,0.05) for FAPAR. Shaded areas indicate 1 standard deviation.</i>	124
<i>Figure 82: Relative analysis RMSD (RMSD divided by value) (top) and analysis RMSD (bottom) of LAI (left) and FAPAR (right) on average over the Murray-Darling basin. Dashed red line indicates the target accuracies: max(20%,0.5) for LAI and max(10%,0.05) for FAPAR. Shaded areas indicate 1 standard deviation.</i>	125
<i>Figure 83: Maps over Southern Africa showing (in green) where GCOS accuracy requirements could be met (LAI: max(20%,0.5), FAPAR: max(10%,0.05)) or may have not be met (in red) for 2019. ...</i>	126

<i>Figure 84: Maps over the Murray-Darling basin showing (in green) where GCOS accuracy requirements could be met (LAI: $\max(20\%, 0.5)$, FAPAR: $\max(10\%, 0.05)$) or may have not be met (in red) for 2019.</i>	127
<i>Figure 85: Annual number of SWI-001 observations available over Southern Africa (only METOP-A until July 20, 2015; after July 21, 2015 both METOP-A and B are used)</i>	129
<i>Figure 86: Annual number of SWI-001 observations available over the Murray-Darling basin (only METOP-A until July 20, 2015; after July 21, 2015 both METOP-A and B are used)</i>	130

LIST OF TABLES

<i>Table 1: Surface State Flag values of the SWI product.....</i>	26
<i>Table 2: Continental hot spots for droughts and heat waves and number of monthly low SSM and LAI records in 2019 with respect to the 2010-2018 period</i>	32
<i>Table 3: Model and analysis LAI scores from 2010 to 2018 and for 2019 over Southern Africa (top), from 2010 to 2018 and for 2019 over the Murray-Darling basin (bottom). Analysis-Model differences show the impact of assimilating LAI and SWI-001 on the simulated LAI. Mean bias, RMSD and SDD are in m^2m^{-2}.....</i>	42
<i>Table 4: Model and analysis FAPAR scores from 2010 to 2018 and for 2019 over Southern Africa (top), from 2010 to 2018 and for 2019 over the Murray-Darling basin (bottom). Analysis-Model differences show the impact of assimilating LAI and SWI-001 on the simulated FAPAR.....</i>	51
<i>Table 5: Model and analysis SA scores from 2010 to 2018 and for 2019 over Southern Africa (top), the Murray-Darling basin (bottom). Analysis-Model differences show the impact of assimilating LAI and SWI-001 on the simulated SA.</i>	60
<i>Table 6: Annual score values of the model and analysis w.r.t. the rescaled SWI-001 over Southern Africa (top) from 2010 to 2019, the Murray-Darling basin (bottom) from 2010 to 2019. Model-analysis differences show the impact of assimilating LAI and SWI-001 on the simulated SSM.</i>	78
<i>Table 7: LST annual scores of the model and analysis w.r.t. the LST observations at 1200 UTC (top) and 0600 UTC (bottom) over Southern Africa. Analysis-Model differences show the impact of assimilating LAI and SWI-001 on the simulated LST. The relatively unbiased average LST at 0600 UTC hides marked spatial and seasonal patterns (Figure 51 and Figure 59).....</i>	104
<i>Table 8: LST annual scores of the model and analysis w.r.t. the LST observations at 0300 UTC (~noon) (top) and at 2100 UTC (~dawn) (bottom) over the Murray-Darling basin. Analysis-Model differences show the impact of assimilating LAI and SWI-001 on the simulated LST. The relatively unbiased average LST at 0600 UTC hides marked spatial and seasonal patterns (Figure 53 and Figure 61).....</i>	105

ACRONYM LIST

ALBH	Bi-hemispherical albedo
ASCAT	Advanced Scatterometer
ATBD	Algorithmic Theoretical Basis Document
C3S	Copernicus Climate Change Service
CCR	Cross-cutting Consistency Report
CDF	Cumulative Distribution Function
CGLS	Copernicus Global Land Service
ECMWF	European Centre for Medium-Range Weather Forecasts
ERA	ECMWF Reanalysis
ET	Evapotranspiration
FAPAR	Fraction of Absorbed Photosynthetically Active Radiation
GCOS	Global Climate Observing System
GPP	Gross Primary Production (photosynthesis)
ISBA	Interactions between Soil, Biosphere, and Atmosphere
LAI	Leaf Area Index
LDAS	Land Data Assimilation System
LSM	Land Surface Model
LST	Land Surface Temperature
MODIS	Moderate Resolution Imaging Spectroradiometer
NEE	Net Ecosystem Exchange of CO ₂
PROBA-V	Project for On-Board Autonomy – Vegetation
PUM	Product User Manual
QF	Quality flag
R	Pearson correlation coefficient
Reco	Ecocystem respiration
RMSE	Root Means Square Difference
RZSM	Root Zone Soil Moisture
SA	Surface Albedo
SDD	Standard Deviation of Differences
SSM	Surface Soil Moisture
SPOT	Satellite Pour l'Observation de la Terre
SQE	Scientific Quality Evaluation
SSF	Surface State Flag
SURFEX	Surface Externalisée (externalized surface models)
SVP	Service Validation Plan
SWI	Soil Water Index

UTC	Universal Time Coordinated
VGT	Vegetation sensor on SPOT satellite

EXECUTIVE SUMMARY

The Copernicus Global Land Service (CGLS) is earmarked as a component of the Land service to operate “a *multi-purpose service component*” that provides a series of biogeophysical products on the status and evolution of land surface at global scale. Production and delivery of the parameters take place in a timely manner and are complemented by the constitution of long-term time series.

The most advanced indirect validation technique consists in integrating the products into a land surface model (LSM) using a data assimilation scheme. The obtained reanalysis accounts for the synergies of the various upstream products and provides statistics which can be used to monitor the quality of the assimilated observations.

Meteo-France develops the ISBA-A-gs generic LSM, able to represent the diurnal cycle of the surface fluxes together with the seasonal, inter-annual and decadal variability of the vegetation biomass. The LSM is embedded in the SURFEX modeling platform together with a simplified extended Kalman filter. These tools form a Land Data Assimilation System (LDAS). The current version of the LDAS (LDAS-Monde) is able to assimilate SPOT-VGT and PROBA-V Leaf Area Index (LAI) and ASCAT surface soil moisture (SSM) satellite products at a global scale at a spatial resolution of at least $0.25^\circ \times 0.25^\circ$. This permits the active monitoring of LAI and SSM variables. A passive monitoring of Surface Albedo (SA), Fraction of Absorbed Photosynthetically Active Radiation (FAPAR) and Land Surface Temperature (LST) is performed (i.e., the simulated values are compared with the satellite products), as these quantities are not assimilated yet. The LDAS generates statistics whose trends can be analyzed in order to detect possible drifts in the quality of the products: (1) for LAI and SSM, metrics derived from the active monitoring (i.e. assimilation) such as innovations (observations vs. model), residuals (observations vs. analysis), and increments (analysis vs. model); (2) for SA, FAPAR and LST, metrics derived from the passive monitoring. In both cases, the Pearson correlation coefficient (R), the root mean square difference (RMSD), the standard deviation of difference (SDD), and mean bias skill scores are used.

In this report, results are presented for the **January-December 2019** period over Southern Africa and over the Murray-Darling basin. Note that the last data from SPOT-VGT were used on 13th May 2014. After this date, new LAI / FAPAR / SA products from PROBA-V are used.

For **LAI**, over both Southern Africa and the Murray-Darling basin, the scores tend to present better values during the dry spells of 2019 than during previous years from 2010 to 2018. The RMSD scores of consolidated estimate of LAI Version 2 and LAI Version 1 are

comparable in 2019. The impact on analyzed LAI of transitioning from SPOT-VGT to PROBA-V is neutral to positive.

For **FAPAR**, over both Southern Africa and the Murray-Darling basin, the scores tend to present slightly better values during the dry spells of 2019 than during previous years from 2010 to 2018. Overall conclusions for FAPAR are similar to those for LAI.

For **SA**, a striking result is that a large increase in the mean bias value is observed after the transition from SPOT-VGT to PROBA-V, of about 0.02 for both Southern Africa and for the Murray-Darling basin. There is a clear discontinuity in the SA time series, not observed for LAI nor for FAPAR.

For **SWI-001**, the impact of the seasonal SSM CDF-matching performed prior the assimilation is particularly striking for Southern Africa. Without a seasonal CDF-matching, the original SSM information would be misleading over Southern Africa.

For **LST**, the model tends to underestimate LST, especially at daytime. Over the Murray-Darling basin, the mean yearly bias is about -8°C in 2019 (a dry year), against -4°C in 2010 (a wet year). This result shows that daytime LST biases are more pronounced in dry conditions. Possible causes of the spatial, diurnal and seasonal patterns of the LST bias are hot-spot phenomenon (more sunlit than shaded elements are seen by the satellite), biases in the incoming solar and infrared radiation data used to force the model.

LDAS analyses were also used to assess the accuracy of LAI and FAPAR observations, with respect to GCOS requirements. It is showed that small values of LAI observations tend to meet the GCOS requirements more often than large values of LAI observations and of FAPAR observations, for both Southern Africa and the Murray-Darling basin. Overall, low FAPAR values present more uncertainties than low LAI values.

1 BACKGROUND

1.1 SCOPE AND OBJECTIVES

The objective of this report is to present an evaluation of the consistency of LAI, SSM (SWI-001), SA, FAPAR and LST over Southern Africa and the Murray-Darling basin for the **January-December 2019** period, with respect to past years (2010-2018). This task was performed by Meteo-France, using the LDAS-Monde tool (Albergel et al., 2017).

1.2 CONTENT OF THE DOCUMENT

The cross-cutting validation method is described in Chapter 2 together with the input products. Chapter 3 presents results at a global scale and the selection of two regions for this report. Chapters 4 to 8 present the results for LAI V1, FAPAR V1, SA, SWI-001, and LST, respectively. Chapter 9 presents the LDAS statistics from **January to December 2019**, vs. past periods of time (2010-2018), together with the impact on LAI and SA scores of switching from SPOT-VGT to PROBA-V in 2014, and with a comparison between consolidated estimate (RT6) of Version 2 LAI and the NRT Version 1 LAI. Chapter 10 summarizes the main conclusions. The references are listed in Chapter 11.

1.3 RELATED DOCUMENTS

1.3.1 *Applicable documents*

AD1: Annex I – Technical Specifications JRC/IPR/2015/H.5/0026/OC to Contract Notice 2015/S 151-277962 of 7th August 2015

AD2: Appendix 1 – Copernicus Global land Component Product and Service Detailed Technical requirements to Technical Annex to Contract Notice 2015/S 151-277962 of 7th August 2015

AD3: GIO Copernicus Global Land – Technical User Group – Service Specification and Product Requirements Proposal – SPB-GIO-3017-TUG-SS-004 – Issue I1.0 – 26 May 2015.

1.3.2 *Input documents*

CGLOPS1_SVP : Service Validation Plan of the Copernicus Global Land Service

GIOGL1_ATBD_SWIV3 Algorithm Theoretical Basis Document of the Soil Water

	Index Version 3 derived from Metop/ASCAT.
CGLOPS1_ATBD_SA1km-V1	Algorithm Theoretical Basis Document of the Surface Albedo Collection 1km Version 1
GIOGL1_ATBD_FAPAR1km-V1	Algorithm Theoretical Basis Document of the FAPAR Collection 1km Version 1
GIOGL1_ATBD_LAI1km-V1	Algorithm Theoretical Basis Document of the LAI Collection 1km Version 1
CGLOPS1_ATBD_FAPAR1km-V2	Algorithm Theoretical Basis Document of the FAPAR Collection 1km Version 2
CGLOPS1_ATBD_LAI1km-V2	Algorithm Theoretical Basis Document of the LAI Collection 1km Version 2
CGLOPS1_ATBD_LST	Algorithm Theoretical Basis Document of the LST derived from geostationary sensors
CGLOPS1_PUM_LAI1km-V1	Product User Manual of LAI Collection 1km Version 1
CGLOPS1_PUM_FAPAR1km-V1	Product User Manual of FAPAR Collection 1km Version 1
CGLOPS1_PUM_SA1km-V1	Product User Manual of Surface Albedo Collection 1km Version 1
CGLOPS1_PUM_LAI1km-V2	Product User Manual of LAI Collection 1km Version 2
CGLOPS1_PUM_FAPAR1km-V2	Product User Manual of FAPAR Collection 1km Version 2
CGLOPS1_PUM_SWIV3-SWI10-SWI-TS	Product User Manual of Soil Water Index Version 3
CGLOPS1_PUM_LST	Product User Manual of Land Surface Temperature

All these documents are available on the Copernicus Global Land Service website (<http://land.copernicus.eu/global>) under the respective products pages.

2 METHODS

2.1 LDAS-MONDE

The LDAS-Monde platform was initially developed over France at a spatial resolution of 8 km × 8 km (Barbu et al., 2014). The extension of the LDAS at the global scale was implemented by Albergel et al. (2017) and results from LDAS-Monde over Southern Africa (26°S-35°S, 14°E-26°E) and over the Murray-Darling basin (26°S-37°S, 140°E-150°E) are showed here.

The LDAS-Monde platform is able to jointly assimilate remotely sensed surface soil moisture (SWI-001) derived from ASCAT backscatter data [GIOGL1_ATBD_SWIV3] and the LAI Collection 1km V1 [GIOGL1_ATBD_LAI1km-V1] provided by the Copernicus Global Land service, into the ISBA-A-gs land surface model (LSM) within the SURFEX modelling platform. ISBA-A-gs is a version of the ISBA model able to simulate photosynthesis and plant growth. In this report, the global ERA-5 analysis (Hersbach and Dee, 2016) was used to force LSM simulations over Southern Africa and over the Murray-Darling basin, at 0.25° x 0.25° spatial resolution, from 2010 to 2019. ERA-5 is developed through the Copernicus Climate Change Service (C3S). ERA-5 uses one of the most recent versions of the Earth system model and data assimilation methods applied at ECMWF, which makes it able to use modern parameterizations of Earth processes compared to older versions used in ERA-Interim. Two other important features of ERA-5 are the improved temporal and spatial resolution, from 6-hourly in ERA-Interim to hourly analysis in ERA-5, and from 79 km in the horizontal dimension and 60 levels in the vertical, to 31 km and 137 levels in ERA-5.

The Copernicus Global Land Service ASCAT **SWI-001** product is used, as it is equivalent to SSM. The SWI-001 product is generated using an exponential filter with a characteristic time length of one day [GIOGL1_ATBD_SWIV3]. Since (1) soil moisture is a model-dependent variable, (2) the SWI-001 product ranges between 0 (dry) and 1 (saturated), the SWI-001 data need to be bias corrected with respect to the model climatology. A seasonal-based CDF (Cumulative Distribution Function) matching technique is used. It consists of a linear transformation (2 parameters) and produces model equivalent volumetric SSM in m³m⁻³. **The two CDF matching parameters are calculated monthly using a three-month moving window from 2010 to 2018, for each model grid-cell. Therefore, a single set of 12 pairs of parameters is obtained for the whole 2010-2018 period. Moreover, only points with more than 30 observations for each three-month-period were considered so that the CDF matching is assumed to be reliable.** The set of parameters is used to rescale and bias-correct the whole SWI-001 time series from 2010 to 2019.

A major difference with Barbu et al. (2014) is that a new version of the ISBA-A-gs model is used (SURFEX version 8.1 instead of version 7.2). This new version allows the prognostic simulation of FAPAR, thanks to an enhanced radiative transfer model within the vegetation canopy (Carrer et al., 2013). Another difference is that the snow-free surface albedo values used in the model are now based on a more realistic climatology derived from the MODIS albedo product (MCD43GF) over a 10-year period. A spatially complete albedo is produced using an ecosystem-reliant temporal interpolation technique that retrieves missing data with 3–8% error (Carrer et al., 2014). While the old albedo of a given biome consisted of a constant value (Faroux et al., 2013), the new snow-free albedo has a seasonal component related to the vegetation cover fraction of crops. The vegetation cover fraction of forests and grasslands is constant through time.

In the SURFEX version 8.1 used in this report, the standard deviation of errors of LAI Collection 1km V1 is assumed to be 20% of LAI. The same assumption is made for the standard deviation of errors of the modelled LAI (20% of modelled LAI) for modelled LAI values higher than $2 \text{ m}^2 \text{ m}^{-2}$. For modeled LAI values lower than $2 \text{ m}^2 \text{ m}^{-2}$, a constant error of $0.4 \text{ m}^2 \text{ m}^{-2}$ is assumed. This error configuration was found best in Barbu et al., 2011 (option 3).

Note that the simulated FAPAR and Surface Albedo (SA) are instantaneous values at 09:00 UTC and include the direct and diffuse solar radiation (“blue-sky”). The satellite-derived observations may differ from these conditions. In particular, the CGLS FAPAR corresponds to direct solar radiation conditions (“black-sky”) at 10:00 UTC.

2.2 INPUT PRODUCTS

The following Copernicus Global Land Service products are considered, over the 2010-2019 period:

- Leaf Area Index (LAI), 10 days updates, 1 km, version 1.4 from SPOT-VGT and version 1.5 from PROBA-V, NRT, used in all LAI Figures and Tables of this report
- Leaf Area Index (LAI), 10 days updates, 1 km, version 2, consolidated after 60 days (RT6), used for comparison with version 1
- Fraction of Absorbed Photosynthetically Active Radiation (FAPAR), 10 days updates, 1 km, version 1.4 from SPOT-VGT and version 1.5 from PROBA-V, NRT
- Soil Water Index (SWI), daily, 0.1° , version 3.02, only the SWI-001 field
- Land Surface Temperature (LST), hourly, 5 km, version 1.2

- Surface albedo (SA), broadband bi-hemispheric reflectance over total spectrum (ALBH extracted from the SA product), 10 days updates, 1 km, version 1.4 from SPOT-VGT and version 1.5 from PROBA-V, NRT

The LAI, FAPAR and SA data are provided at a temporal resolution of 10 days. A quality check based on the Quality Flag fields is performed. The data are kept only if all the quality flags are set to 0 (flags for land/water detection, snow presence, aerosol contamination) [CGLOPS1_PUM_LAI1km-V1, CGLOPS1_PUM_FAPAR1km-V1, CGLOPS1_PUM_SA1km-V1].

For the SWI product, a quality flag (QF) related to the number of available SSM measurements used for calculation of Soil Water Index (SWI) is given for each time scale (T). The Surface State Flag (SSF) is provided as in Table 1 [CGLOPS1_PUM_SWIV3].

Table 1: Surface State Flag values of the SWI product

SSF value	Detected surface state
0	unknown
1	unfrozen
2	frozen
3	temporary melting / water on the surface
255	missing value

Before projecting the SWI-001 data onto the ERA5 grid, the observations are screened to remove the observations with a quality flag (QF) lower than 80% and only the data flagged SSF=0 or SSF=1 are used. The 80% QF threshold value is chosen in order to avoid any persistence effect (i.e. the same value being automatically prescribed when observations are missing). The chosen QF threshold value has an impact on the number of used observations, especially at low latitudes, but it was checked that changes in this value have little impact on the scores given in this report. After projection, additional masks for urban regions, steep mountainous terrain, and frozen instances indicated by the model simulations but not detected by ASCAT, are applied.

For LST product, the GLOBE netcdf files are used. Only the LST values corresponding to a QF indicating cloud free pixels (clear sky > 90%) are processed [CGLOPS1_PUM_LST].

After screening for quality flags, the remaining data are projected onto a 0.25° grid, for all the products. The observations are then aggregated over the model grid cell (using a simple arithmetic average) when, at least, half of the observation grid points are present. For 1 km

LAI, FAPAR and SA products, this represents at least 312 observations; for the 0.044° LST product, this represents at least 16 observations; for the 0.1° SWI product, this represents at least 3 observations.

We downloaded the products through a subscription on the Copernicus Global Land Service access portal (<https://land.copernicus.vgt.vito.be/PDF/portal/Application.html#Home>).

2.3 EVALUATION METRICS

The LDAS performs the active monitoring of SSM and LAI (these quantities are assimilated into the model), and the passive monitoring of SA, FAPAR, and LST (these quantities are not assimilated into the model). For the five considered variables, the observations are compared to the model simulations after the integration of LAI and SSM observations (i.e. the analysis), and to the model without assimilation (i.e. the open-loop). Several scores are calculated. For the actively monitored variables (SSM and LAI) other LDAS statistics such as the assimilation increments of the analyzed variables (root-zone soil moisture (RZSM) and LAI) can be considered.

2.3.1 Scores

In this report, an indirect validation is made. In a direct validation, in situ reference observations are used as a ground truth. Instead, we use independent model simulations, together with model and observation uncertainty estimates, to monitor the consistency between the seasonal and inter-annual variability of the products and the model.

The LAI and SWI-001 products are assimilated into the ISBA-A-gs model using the LDAS-Monde infrastructure described in Sect. 2.1. Numerical models contain errors that increase with time due to model imperfections and uncertainties in initial and boundary conditions. Data assimilation minimizes these errors by correcting the model statistics using new observations. Integrating observations into a land surface model is also a way to assess and monitor the observation errors. The result of the assimilation is an analysis, i.e. a new model simulation incorporating the information brought by the LAI and SWI-001 products. A rather small impact of the assimilation is observed on SSM. On the other hand, the assimilation has a marked impact on the simulated LAI and on the simulated root-zone soil moisture (RZSM). All the products (the rescaled SWI-001, LAI, FAPAR, SA, LST) are compared with the open-loop model simulation and with the analysis. The impact of the assimilation on RZSM is assessed comparing the open-loop simulation to the analyzed RZSM.

Four metrics are used to compare the satellite products (*sat*) with the model simulations or analyses (*mod*):

- Correlation Coefficient

- Bias
- Standard Deviation of Differences (SDD)
- Root Mean Square Difference (RMSD)

These quantities are defined as:

$$CC = \frac{\sum_{k=1}^N (sat_k - \overline{sat})(mod_k - \overline{mod})}{\sqrt{\sum_{k=1}^N (sat_k - \overline{sat})^2 \sum_{k=1}^N (mod_k - \overline{mod})^2}}$$

$$\text{with } \overline{sat} = \frac{1}{N} \sum_{k=1}^N sat_k ; \quad \overline{mod} = \frac{1}{N} \sum_{k=1}^N mod_k ;$$

N represents the number of gridded observations (equal to the number of different gridded model estimates) used in the calculation of the scores at several dates.

$$Bias = \frac{1}{N} \sum_{k=1}^N (mod_k - sat_k)$$

$$SDD = \sqrt{\frac{1}{N} \sum_{k=1}^N (mod_k - sat_k - Bias)^2}$$

$$RMSD = \sqrt{\frac{1}{N} \sum_{k=1}^N (mod_k - sat_k)^2}$$

2.3.2 Increments

Increments are defined by Eq. (2) in Barbu et al. (2014). They correspond to the difference between the analyzed variables (i.e. after the assimilation of satellite observations) and the model prediction (prior the assimilation):

$$\Delta x = \mathbf{K} [y^0 - H(x)]$$

where x is the state vector (RZSM and LAI), y^0 the observation vector (SSM and LAI), H is the linearized observation operator, and K is the Kalman gain. The $y = H(x)$ term represents the model counterpart (SSM and LAI) of the observations.

The increments on the state variables impact several key variables such as the carbon (photosynthesis through Gross Primary Production (GPP), net ecosystem exchange (NEE), ecosystem respiration (Reco)) and water (evapotranspiration (ET), drainage) fluxes.

3 RESULTS AT A GLOBAL SCALE

LDAS-Monde was operated at a global scale, at $0.25^\circ \times 0.25^\circ$ spatial resolution, from 2010 to 2019. Figure 1 presents the mean observed LAI V1 (hereafter called GEOV1) values together with the RMSD between the observations and the model (open-loop and analysis). Because LAI observations are integrated into the model, the assimilation tends to reduce the LAI RMSD values. Rather large LAI RMSD values ($> 1.5 \text{ m}^2\text{m}^{-2}$) can remain after the assimilation, especially in forested areas.

In order to perform the cross-cutting evaluation over contrasting areas, 19 regions across the globe known for being potential hot spots for droughts and heat waves were selected. They are listed in Table 2 and presented in Figure 2.

Not all regions can be considered in detail in this report. We select regions affected by severe conditions in 2019 using the SSM and LAI observations. Namely, we focus on regions tending to present smallest values of monthly mean SSM and LAI observations in 2019, rather than in previous years (2010-2018). For each region, Table 2 shows the number of monthly SSM and LAI low records in 2019 together with the number of months with SSM and LAI lower than the mean of previous years.

The Southern Africa area presents 2 SSM low monthly records and 1 LAI low monthly record in 2019 and lower than average values are found for nearly all months (Table 2). This result can be related to precipitation below normal in 2019 (<https://earthobservatory.nasa.gov/images/146015/drought-threatens-millions-in-southern-africa>).

It appears that the Murray-Darling basin in Australia experienced severe conditions in 2019, with 6 SSM low monthly records and 3 LAI low monthly records and lower than average values are found for all months (Table 2). The Australian Bureau of Meteorology repeatedly reported low records of precipitation for this area (see for example the water bulletin for August 2019, <http://www.bom.gov.au/water/monthly-water-update/IDA30006.2019-08/murray-darling-basin/>). This drought event was also marked by warmest temperatures on record for a large part of this area (<http://www.bom.gov.au/climate/current/annual/aus/>).

Therefore in this report, the Southern Africa and the Murray-Darling regions are considered. Figure 3 illustrates the SSM and LAI records observed in these areas with respect to previous years.

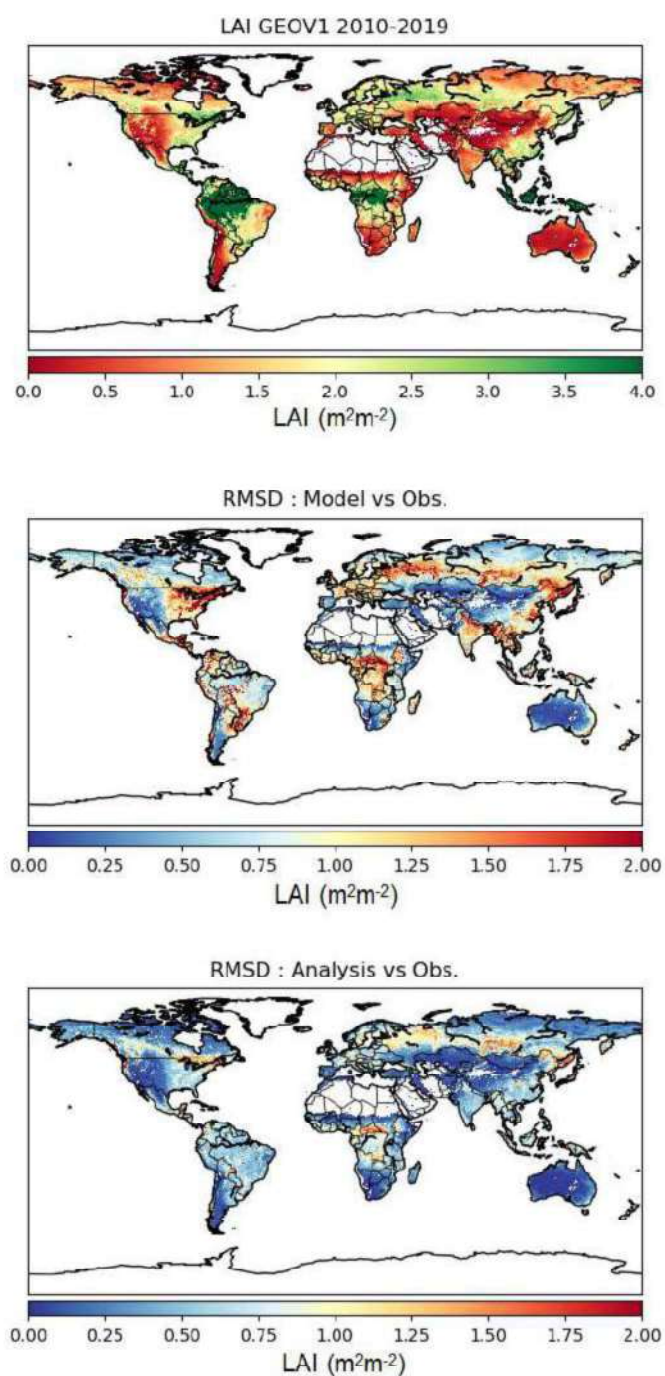


Figure 1: Mean observed LAI for 2010-2019 (top) at a global scale, model open-loop vs. observation RMSD (middle), analysis vs. observation RMSD (bottom).

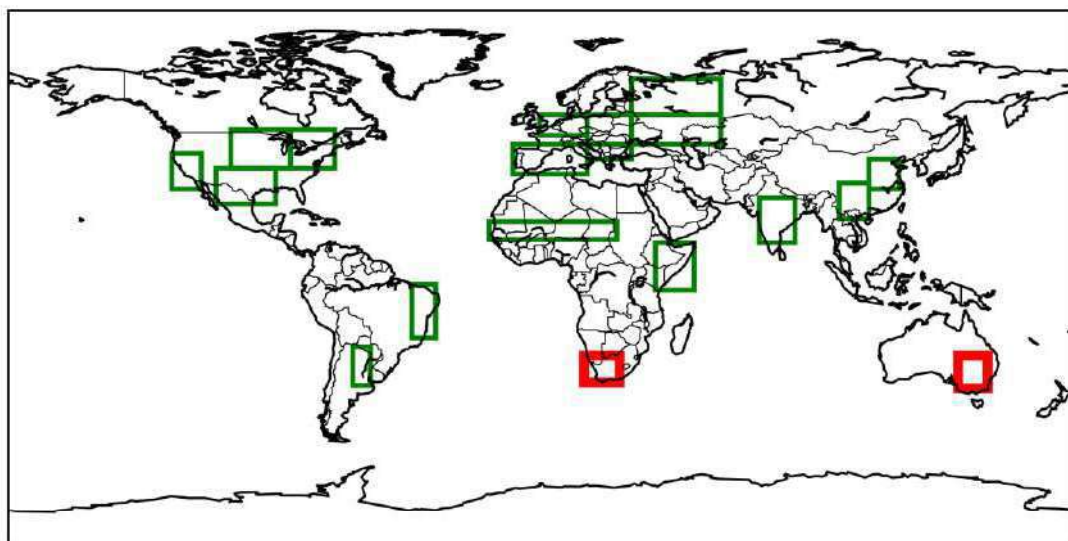


Figure 2: Continental potential hot spots for droughts and heat waves at a global scale.
 Regions considered in this report affected by severe conditions in 2019 are indicated:
 Southern Africa, and the Murray-Darling basin in Australia.

Table 2: Continental hot spots for droughts and heat waves and number of monthly low SSM and LAI records in 2019 with respect to the 2010-2018 period

Region name	Abbrev.	LON-W	LON-E	LAT-S	LAT-N	Number of months with SSM ...		Number of months with LAI ...	
						low records	smaller than the mean of previous years	low record	smaller than the mean of previous years
Western Europe	WEUR	-1	15	48	55	0	7	0	4
Western Mediterranean	WMED	-10	15	35	45	0	5	0	3
Eastern Europe	EEUR	15	30	45	55	1	6	1	7
Balkans	BALK	15	30	40	45	0	4	0	8
Western Russia	WRUS	30	60	55	67	1	2	3	7
Lower Volga	LVOL	30	60	45	55	0	9	0	4
India	INDI	73	85	12	27	0	2	0	2
Southwestern China	SWCH	100	110	20	32	0	3	0	0
Northern China	NRCH	110	120	30	40	0	6	0	4
Murray-Darling	MUDA	140	150	-37	-26	6	12	3	12
California	CALF	-125	-115	30	42	0	2	1	4
Southern Plains	SPLN	-110	-90	25	37	0	0	0	1
Midwest	MIDW	-105	-85	37	50	0	2	0	3
Eastern North	ENRT	-85	-70	37	50	0	4	3	7
Nordeste	NDST	-44	-36	-20	-2	0	3	0	0
Pampas	PAMP	-64	-58	-36	-23	0	4	0	0
Sahel	SAHL	-18	25	13	19	0	1	0	6
East Africa	EAFR	38	51	-4	12	0	5	0	4
Southern Africa	SAFR	14	26	-35	-26	2	11	1	12

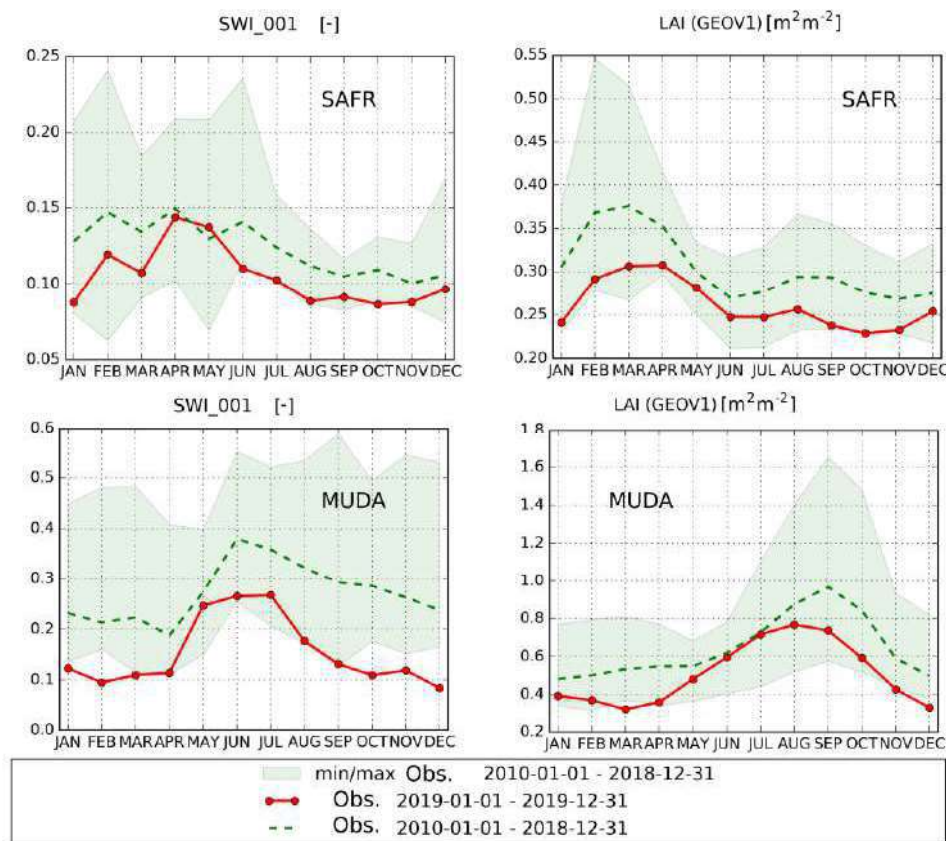


Figure 3: Mean observed monthly (left) SSM and (right) LAI values in 2019 with respect to the minimum, mean and maximum values from 2010 to 2018 over (top) Southern Africa ("SAFR") and (bottom) the Murray-Darling basin ("MUDA").

Conclusion for results at a global scale:

LDAS-Monde was operated at a global scale from 2010 to 2019 and particularly severe conditions were identified in 2019 over two regions: Southern Africa, and the Murray-Darling basin in Australia. Figure 3 shows that LAI values were systematically smaller than the mean LAI of previous years in Southern Africa, and over the Murray-Darling basin. Except for May 2019 in Southern Africa, the SSM values were systematically smaller than the mean SSM of previous years.

4 RESULTS FOR LAI V1

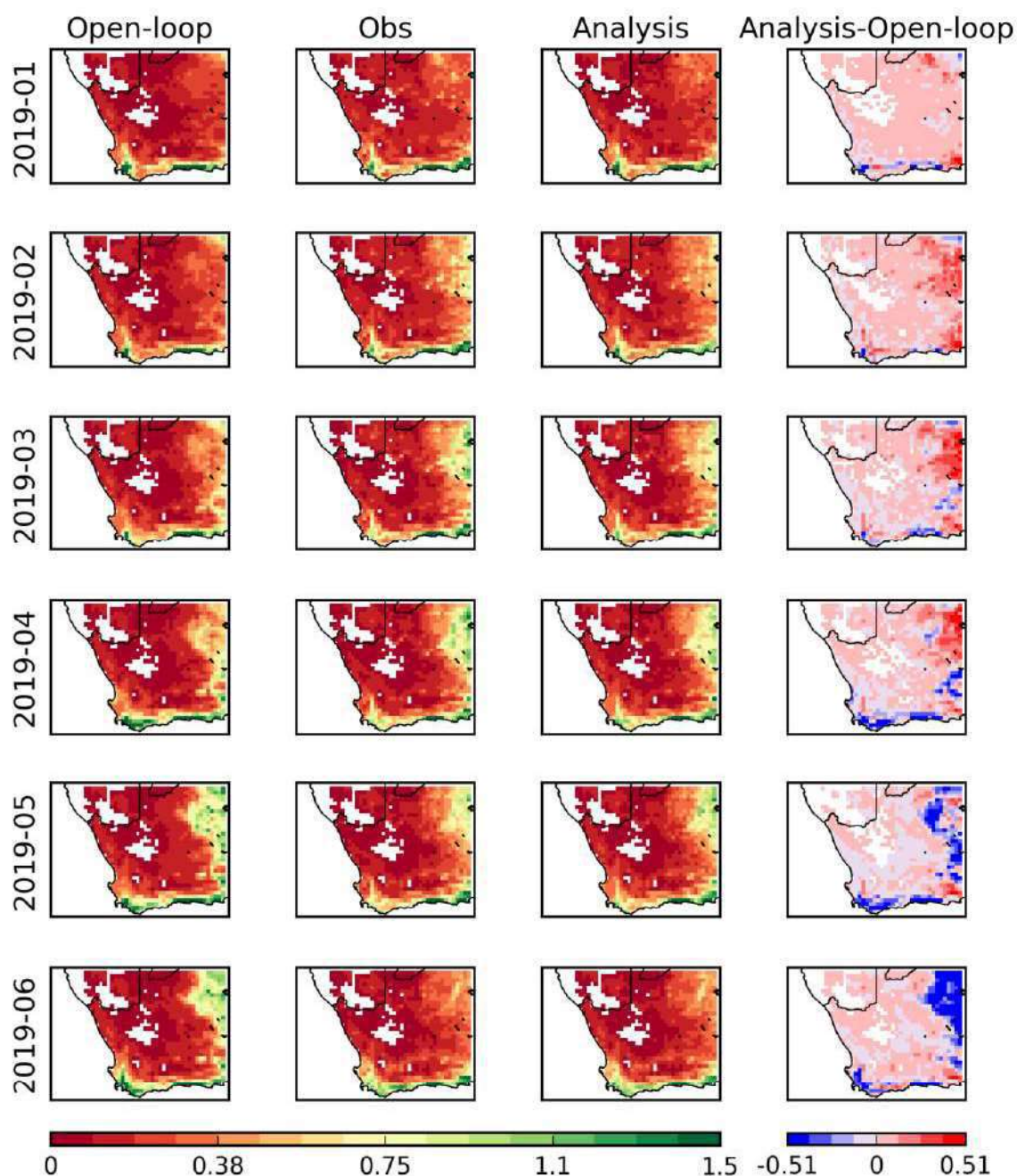


Figure 4: Monthly average values of LAI over Southern Africa at 0.25° spatial resolution from January (top) to June 2019 (bottom). From left to right: model, satellite product, analysis, analysis-model difference. The latter shows the impact of assimilating LAI and SWI-001 on the simulated LAI. The color scale range of LAI values is 0 to 1.5 m^2m^{-2} . Areas with vegetation cover fraction less than 0.1 are left blank.

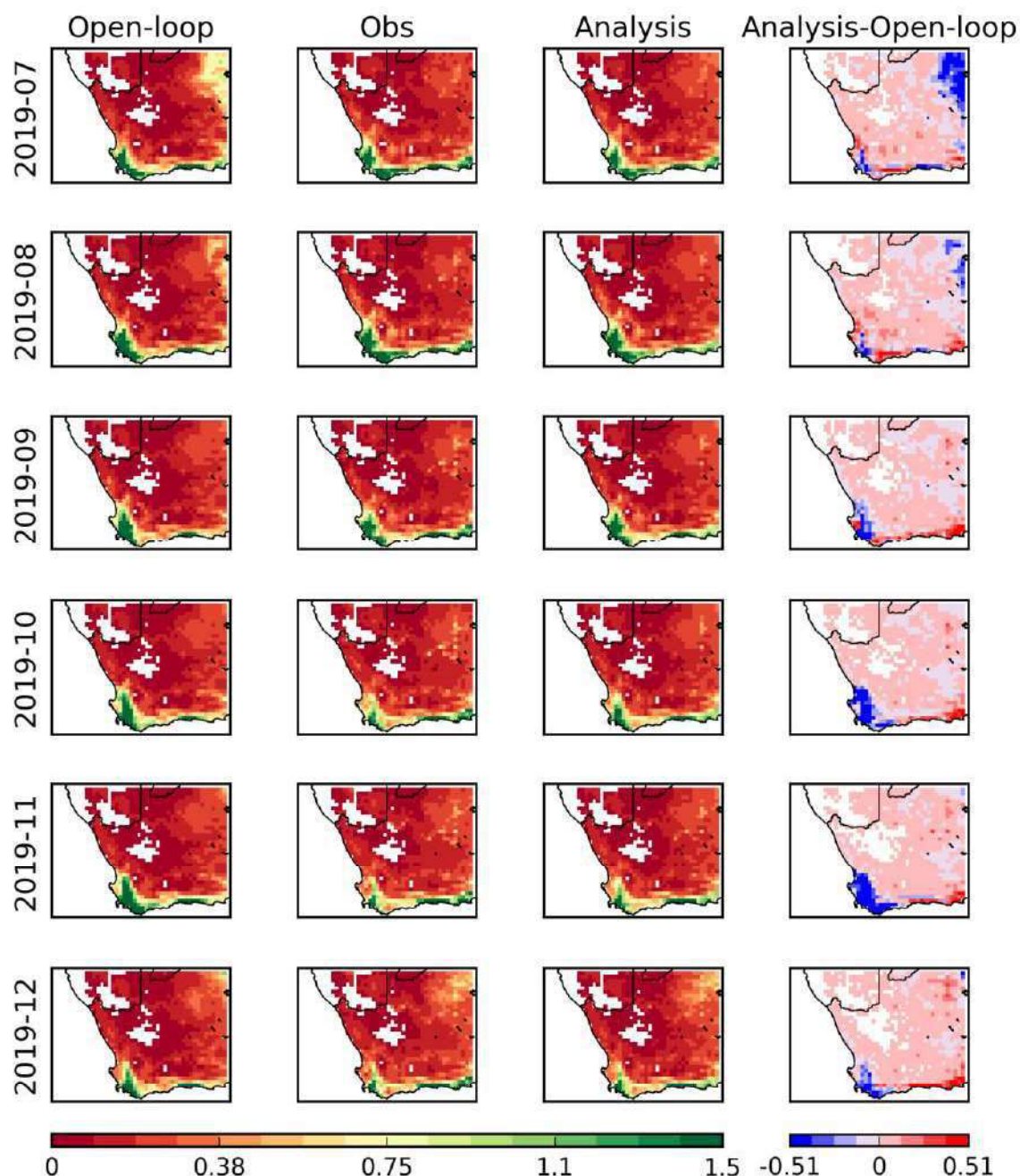


Figure 5: Monthly average values of LAI over Southern Africa at 0.25° spatial resolution July (top) to December 2019 (bottom). From left to right: model, satellite product, analysis, analysis-model difference. The latter shows the impact of assimilating LAI and SWI-001 on the simulated LAI. The color scale range of LAI values is 0 to 1.5 m^2m^{-2} . Areas with vegetation cover fraction less than 0.1 are left blank.

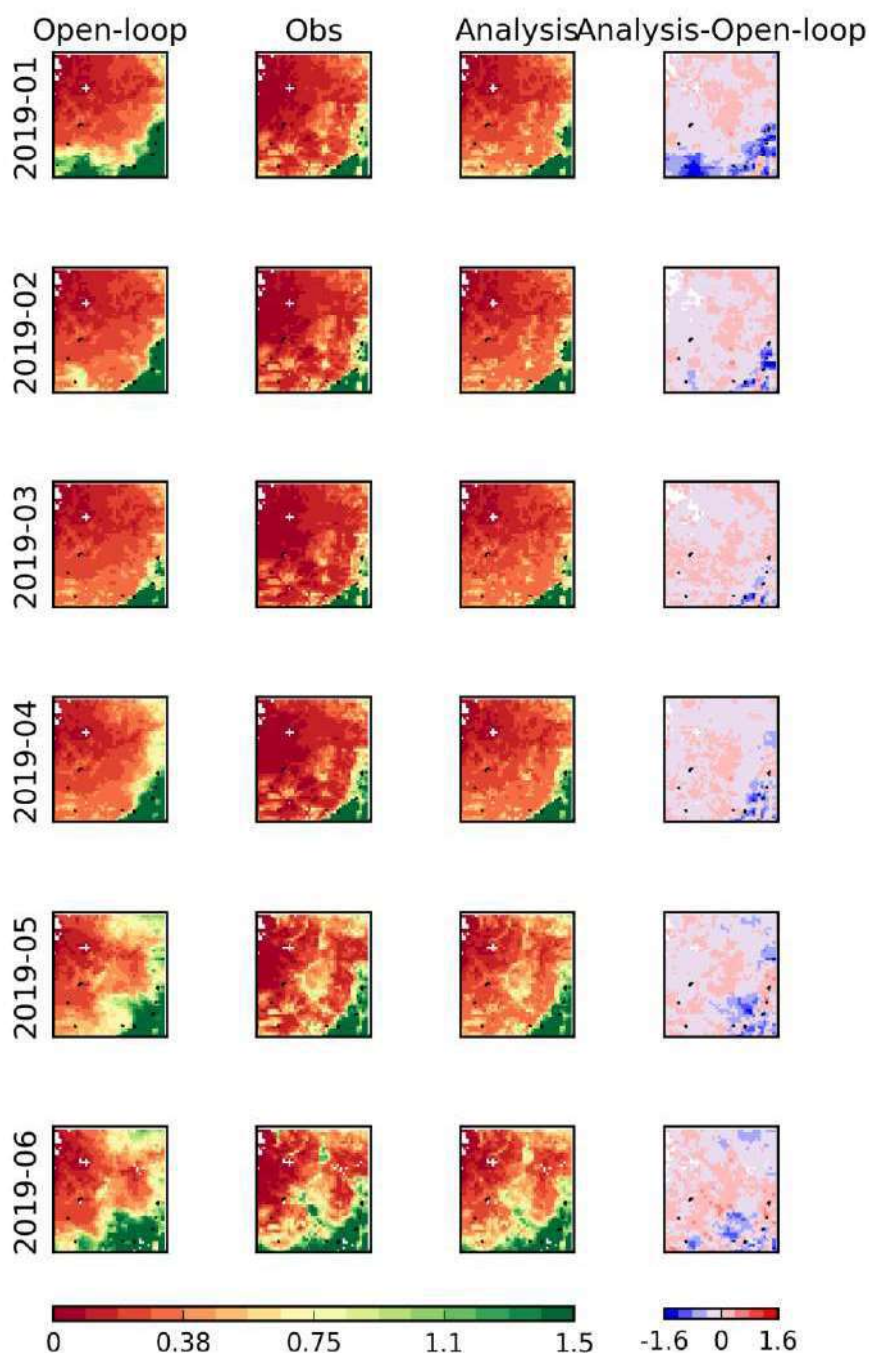


Figure 6: Monthly average values of LAI over the Murray-Darling basin at 0.25° spatial resolution from January (top) to June 2019 (bottom). From left to right: model, satellite product, analysis, analysis-model difference. The latter shows the impact of assimilating LAI and SWI-001 on the simulated LAI. The color scale range of LAI values is 0 to 1.5 m²m⁻². Areas with vegetation cover fraction less than 0.1 are left blank.

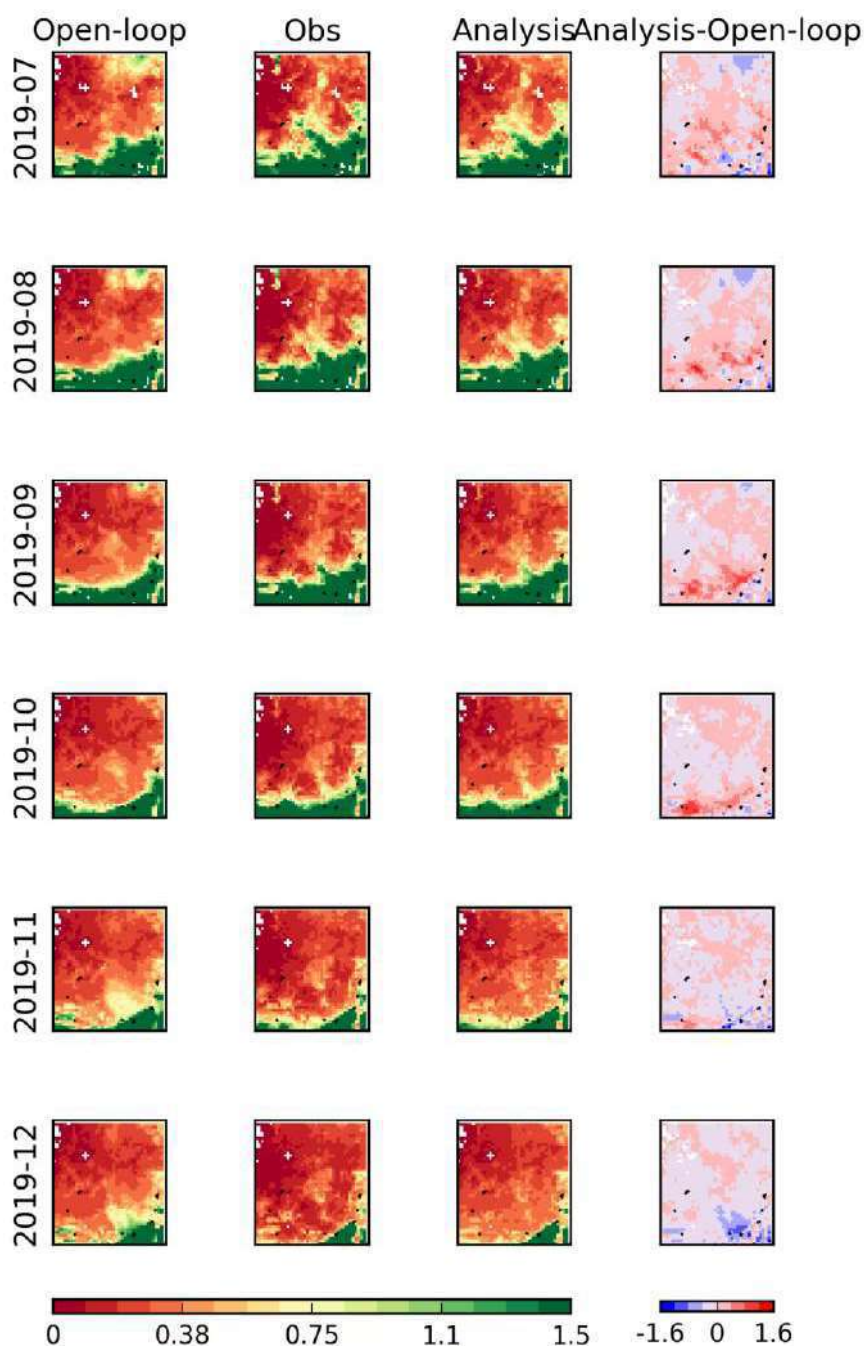


Figure 7: Monthly average values of LAI over the Murray-Darling basin at 0.25° spatial resolution from July (top) to December 2019 (bottom). From left to right: model, satellite product, analysis, analysis-model difference. The latter shows the impact of assimilating LAI and SWI-001 on the simulated LAI. The color scale range of LAI values is 0 to 1.5 m²m⁻². Areas with vegetation cover fraction less than 0.1 are left blank.

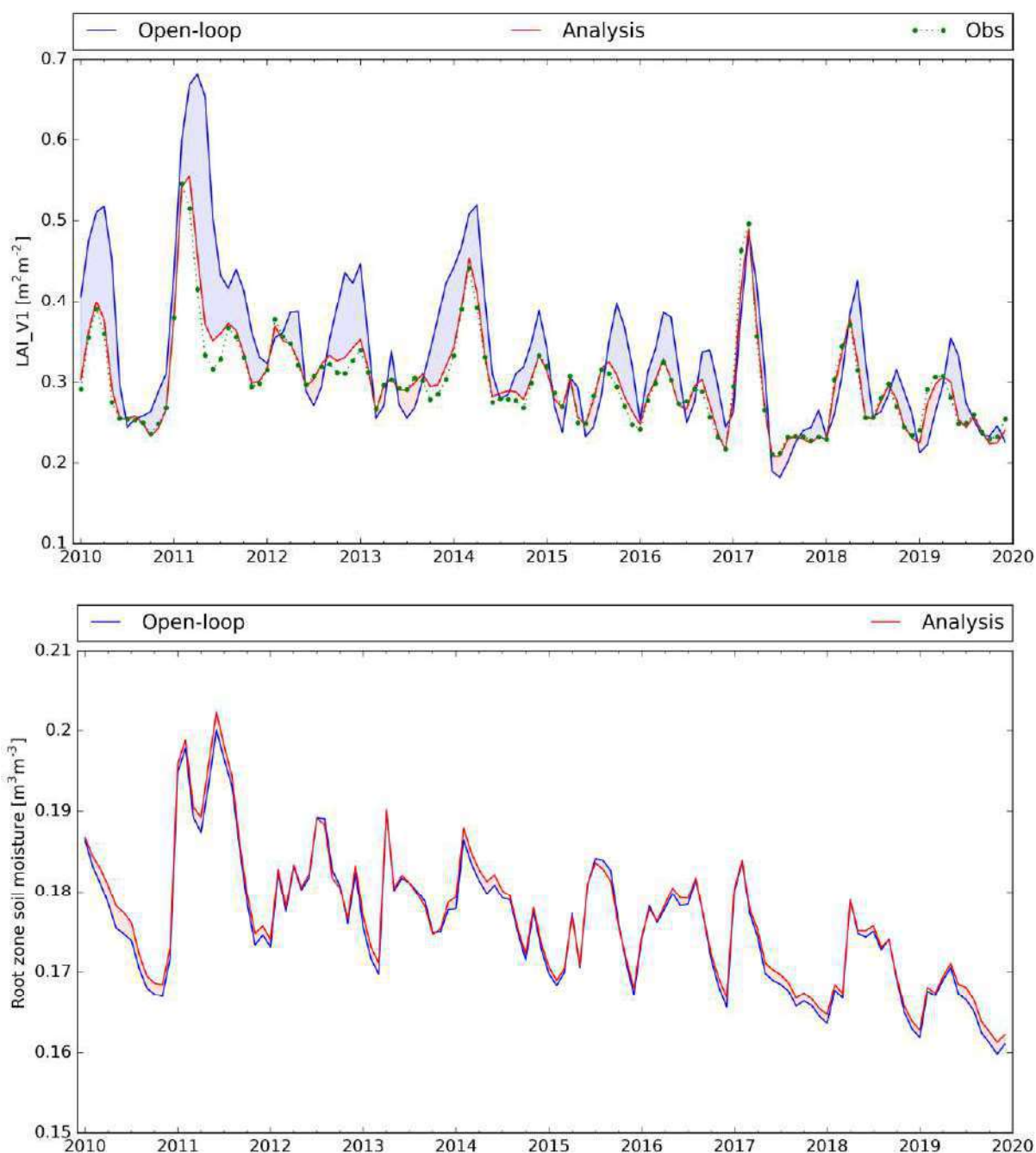


Figure 8: Monthly average values over Southern Africa of LAI (top) and root-zone soil moisture (bottom) from 1 January 2010 to 31 December 2019: model (blue line), satellite product (green circles), analysis (red line). Analysis-Model differences show the impact of assimilating LAI and SWI-001 on the simulated LAI and root-zone soil moisture.

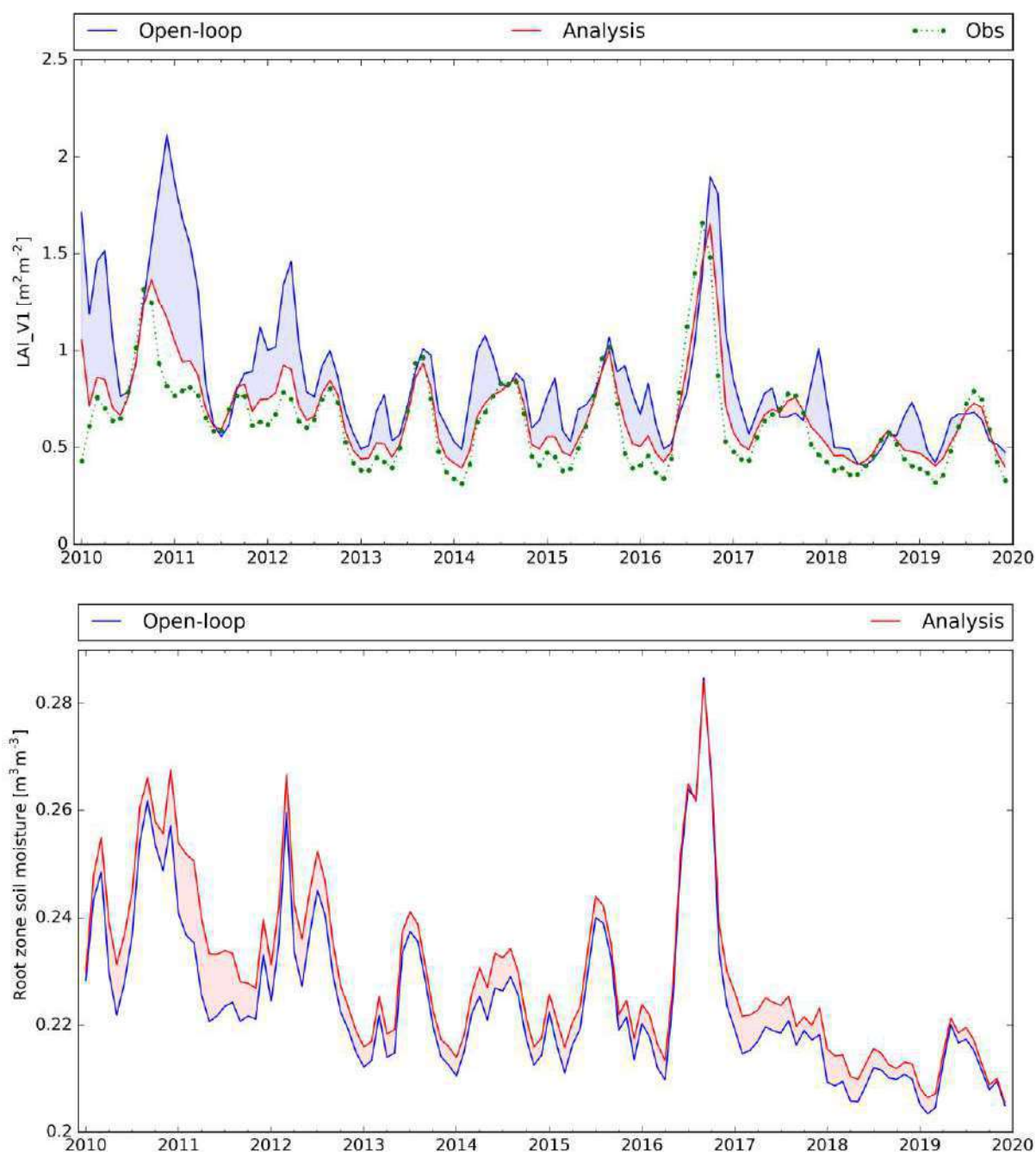


Figure 9: Monthly average values over the Murray-Darling basin of LAI (top) and root-zone soil moisture (bottom) from 1 January 2010 to 31 December 2019: model (blue line), satellite product (green circles), analysis (red line). Analysis-Model differences show the impact of assimilating LAI and SWI-001 on the simulated LAI and root-zone soil moisture.

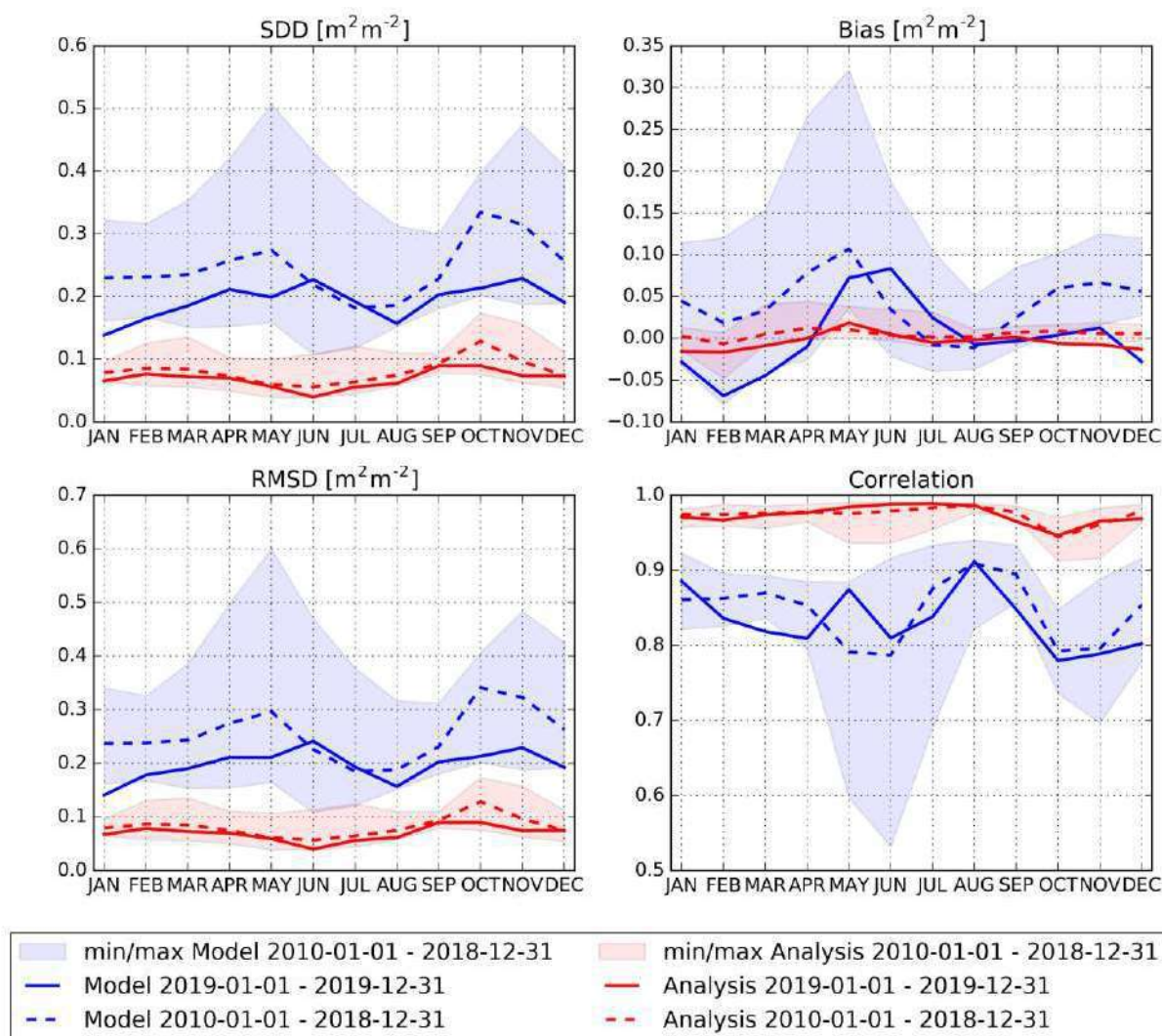
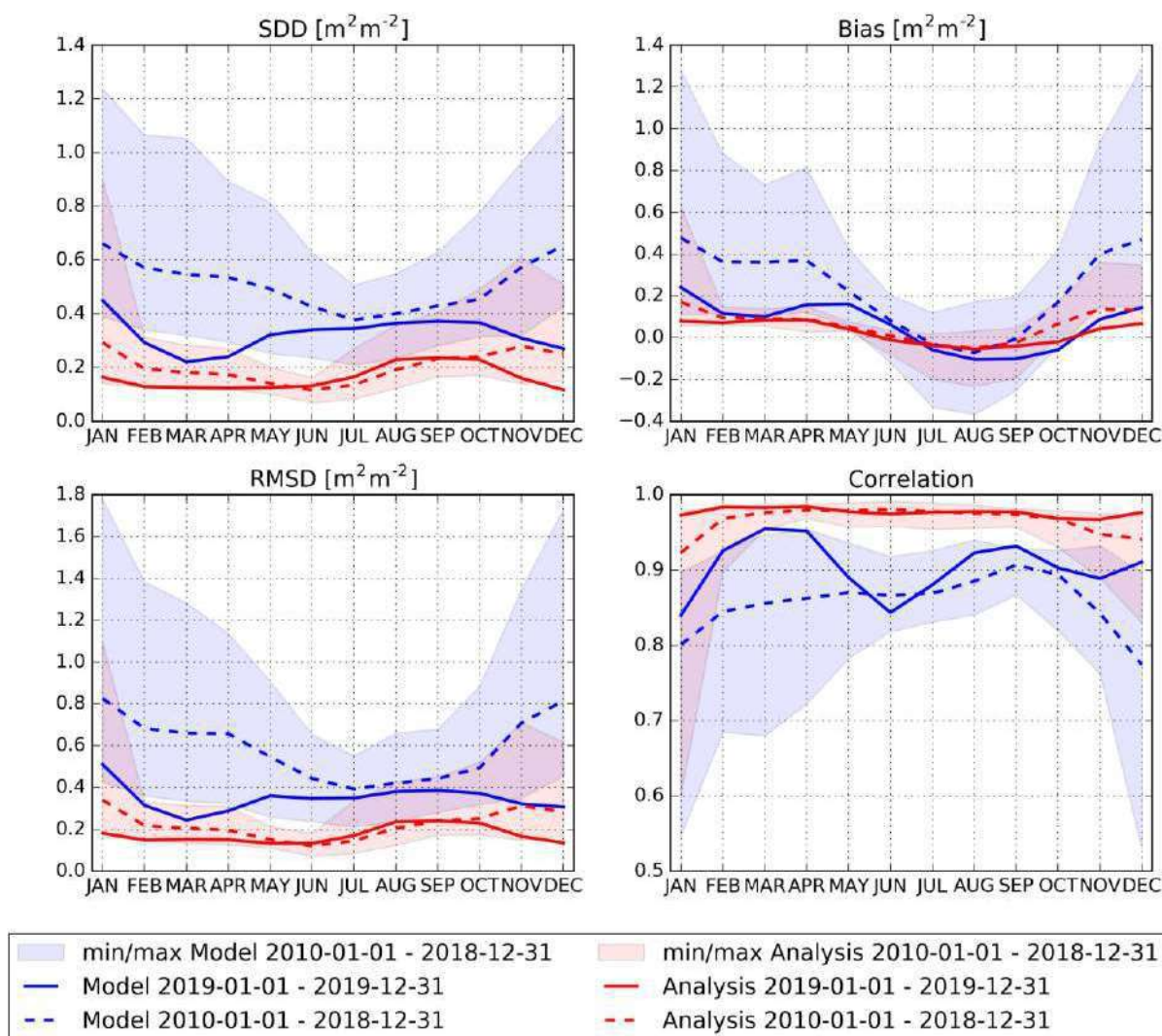


Figure 10: Monthly LAI scores of the model (blue) and analysis (red) when compared to the observations over Southern Africa at 0.25° spatial resolution: from 2010 to 2018 (dashed lines), with N ranging from 27,274 in December to 28,323 in January-March, August-November; and for 2019 (solid lines), with N ranging from 3,101 in July to 3,122 in January. The monthly N values are indicated in the legend Table. Analysis-Model differences show the impact of assimilating LAI and SWI-001 on the simulated LAI. Shaded areas are between minimum and maximum score values recorded from 2010 to 2018.



	JAN	FEB	MAR	APR	MAY	JUN	JUL	AUG	SEP	OCT	NOV	DEC	min	max
2010-01-01 - 2018-12-31	46888	46886	46872	46880	46871	46841	46627	46748	46829	46882	46892	45149	45149	46892
2019-01-01 - 2019-12-31	5203	5202	5202	5193	5187	5074	5103	5113	5167	5200	5202	5198	5074	5203

Figure 11: Monthly LAI scores of the model (blue) and analysis (red) when compared to the observations over the Murray-Darling basin at 0.25° spatial resolution: from 2010 to 2018 (dashed lines), with N ranging from 45,149 in December to 46,892 in October; and for 2019 (solid lines), with N ranging from 5,074 in June to 5,203 in January. The monthly N values are indicated in the legend Table. Analysis-Model differences show the impact of assimilating LAI and SWI-001 on the simulated LAI. Shaded areas are between minimum and maximum score values recorded from 2010 to 2018.

Table 3: Model and analysis LAI scores from 2010 to 2018 and for 2019 over Southern Africa (top), from 2010 to 2018 and for 2019 over the Murray-Darling basin (bottom). Analysis-Model differences show the impact of assimilating LAI and SWI-001 on the simulated LAI. Mean bias, RMSD and SDD are in m^2m^{-2} .

	Version	Bias	Correlation	RMSD	SDD	Nb_pts
2010-01-01 - 2018-12-31	Model	0.042	0.826	0.270	0.267	338793
2010-01-01 - 2018-12-31	Analysis	0.005	0.971	0.087	0.086	338793
2019-01-01 - 2019-12-31	Model	0.000	0.821	0.199	0.199	37378
2019-01-01 - 2019-12-31	Analysis	-0.004	0.973	0.071	0.071	37378

	Version	Bias	Correlation	RMSD	SDD	Nb_pts
2010-01-01 - 2018-12-31	Model	0.234	0.788	0.667	0.625	560365
2010-01-01 - 2018-12-31	Analysis	0.061	0.946	0.262	0.255	560365
2019-01-01 - 2019-12-31	Model	0.063	0.881	0.354	0.348	62044
2019-01-01 - 2019-12-31	Analysis	0.026	0.969	0.177	0.175	62044

Conclusion for LAI:

Over Southern Africa, during the drought period from August to October 2019, both modelled and analyzed LAI tend to present better SDD and RMSD scores values than those observed during the 2010-2018 reference period of time (Figure 10).

Over the Murray-Darling basin, apart from the May-August period, LAI values lower than normal are observed (Figure 3). In relation to these small LAI values, both model and analysis scores in 2019 tend to present better than average values (Figure 11, Table 3).

For both Southern Africa and the Murray-Darling basin, the model bias presents a marked seasonality (Figure 10, Figure 11). This is caused by a delayed (and advanced, respectively) peak LAI date in the model simulations (Figure 8, Figure 9). This could be attributed to biases in the ERA5 radiation forcing of the model (Urraca et al., 2018). The LAI bias seasonality is almost completely suppressed by the assimilation and the analyzed LAI hardly presents any bias (Figure 10, Figure 11).

Figure 4 and Figure 5 show that the assimilation of SSM and LAI observations tends to reinforce the drought signal over Southern Africa from May to December 2019, with smaller LAI values in the analysis in the area of Kimberley from May to August, and in the area of Cape Town from April to December. Figure 6 and Figure 7 show that the assimilation of SSM and LAI observations markedly reduces LAI values over the southeastern part of the Murray-Darling basin, from January to June, and in December.

5 RESULTS FOR FAPAR V1

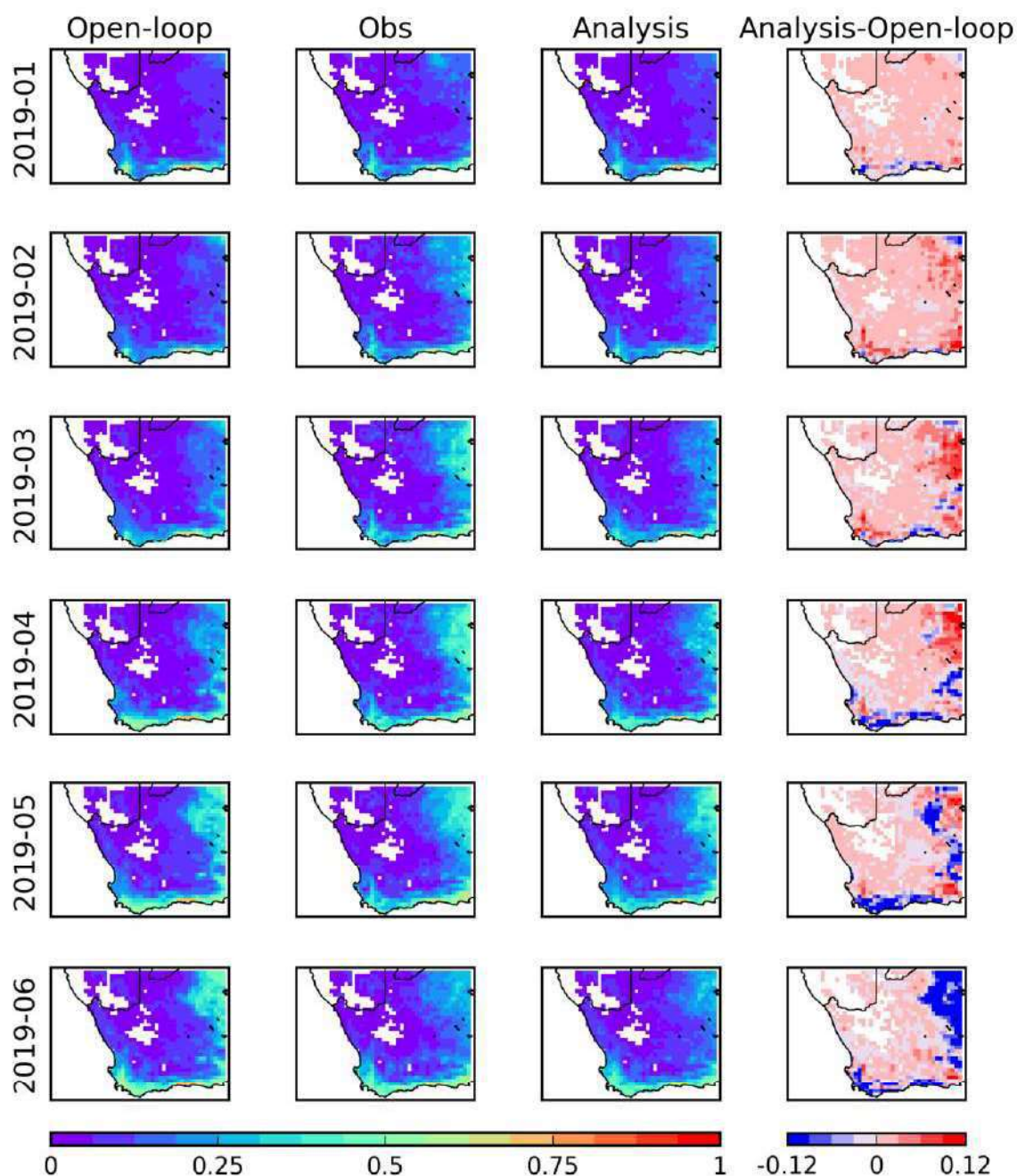


Figure 12: Monthly average values of FAPAR over Southern Africa at 0.25° spatial resolution from January (top) to June 2019 (bottom). From left to right: model, satellite product, analysis, analysis-model difference. The latter shows the impact of assimilating LAI and SWI-001 on the simulated FAPAR. The color scale range of FAPAR values is 0 to 1.0. Areas with vegetation cover fraction less than 0.1 are left blank.

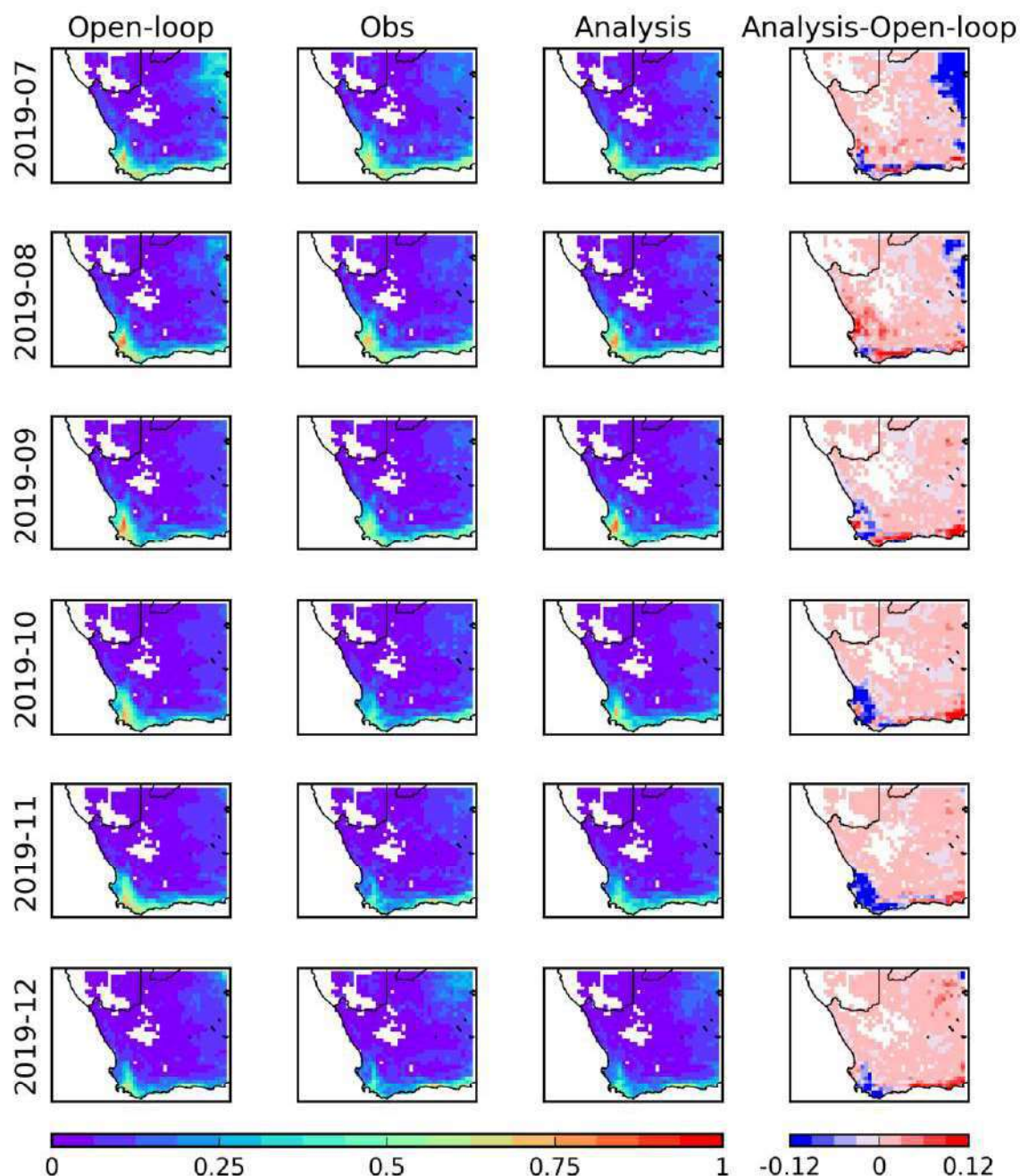


Figure 13: Monthly average values of FAPAR over Southern Africa at 0.25° spatial resolution July (top) to December 2019 (bottom). From left to right: model, satellite product, analysis, analysis-model difference. The latter shows the impact of assimilating LAI and SWI-001 on the simulated FAPAR. The color scale range of FAPAR values is 0 to 1.0. Areas with vegetation cover fraction less than 0.1 are left blank.

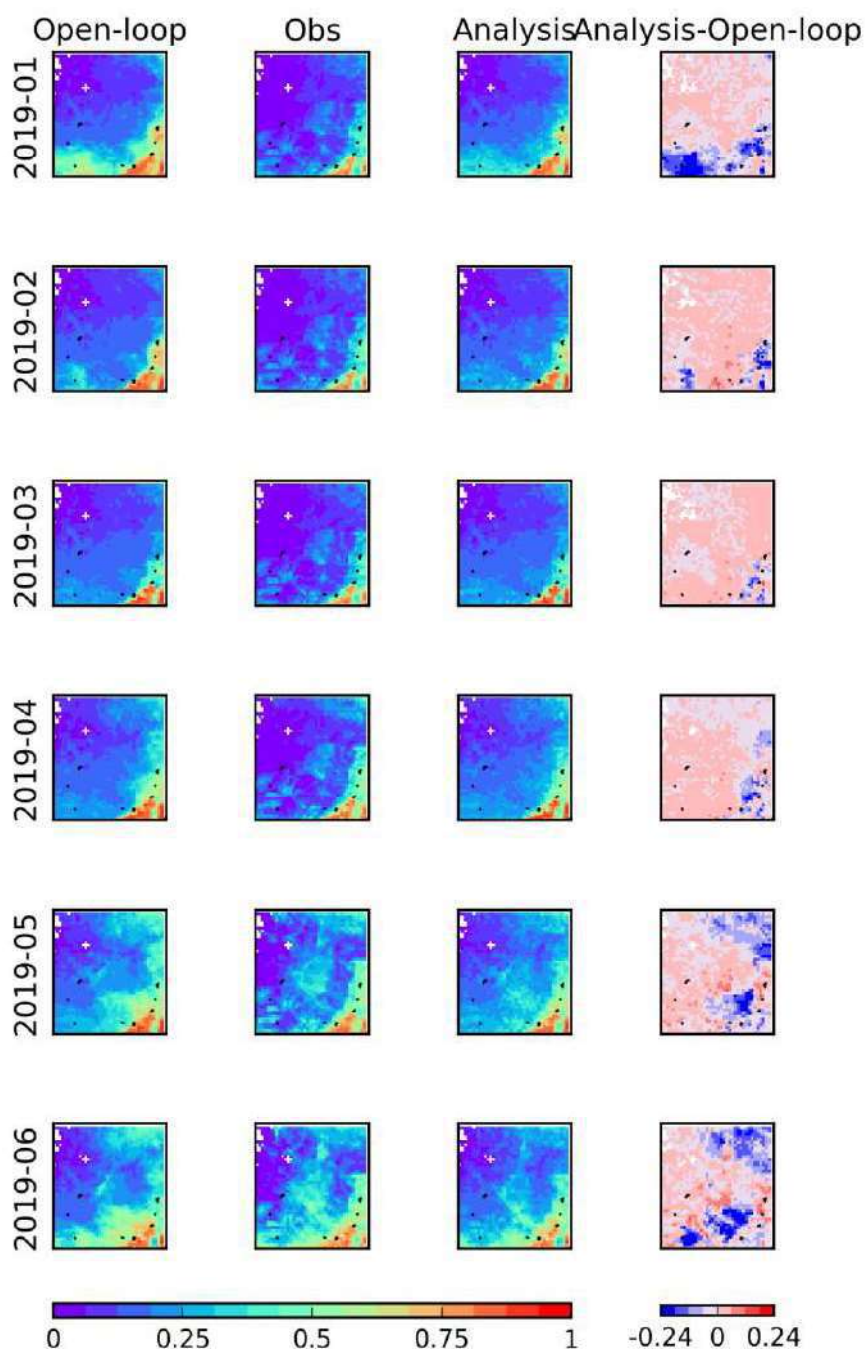


Figure 14: Monthly average values of FAPAR over the Murray-Darling basin at 0.25° resolution January (top) to June 2019 (bottom). From left to right: model, satellite product, analysis, analysis-model difference. The latter shows the impact of assimilating LAI and SWI-001 on the simulated FAPAR. The color scale range of FAPAR values is 0 to 1.0. Areas with vegetation cover fraction less than 0.1 are left blank.

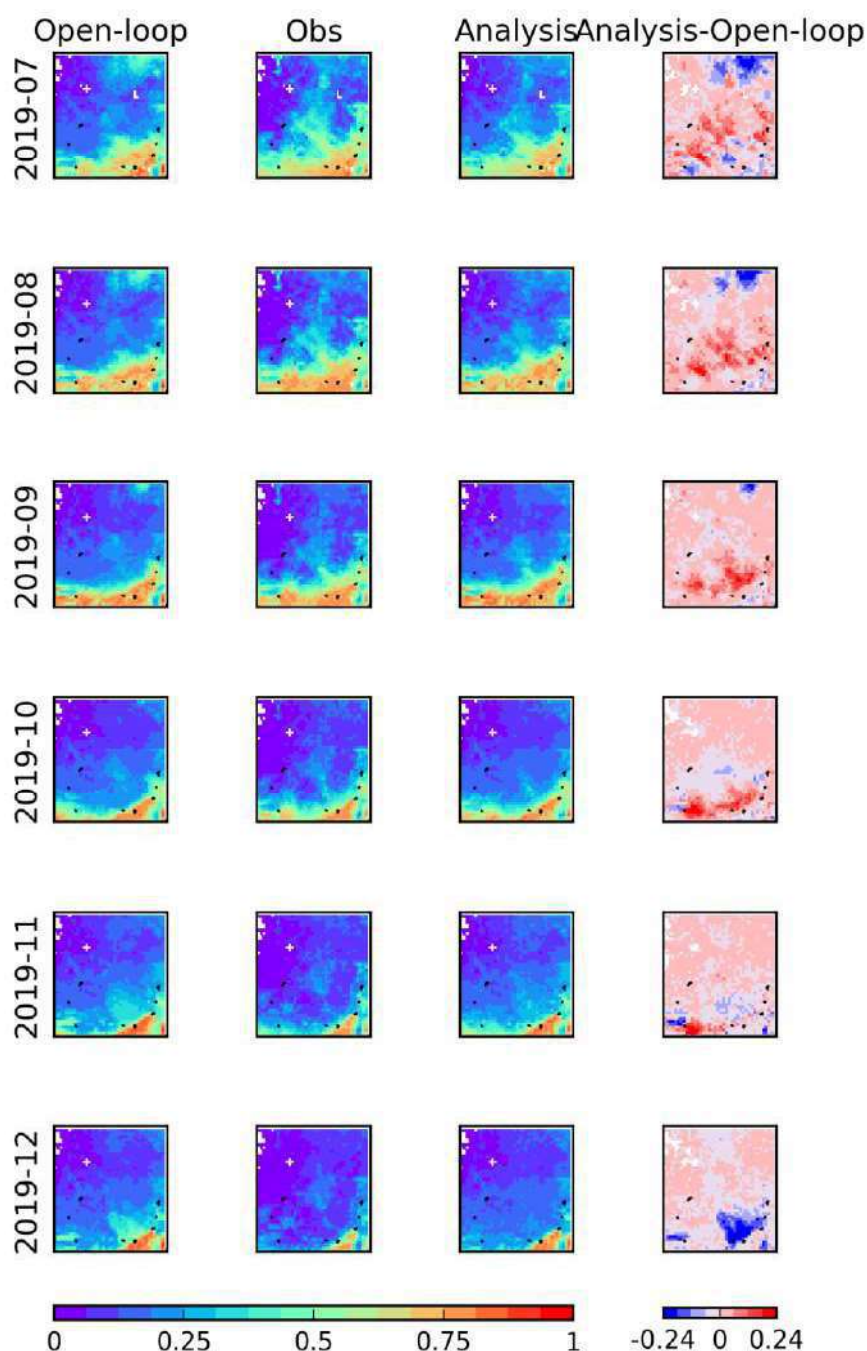


Figure 15: Monthly average values of FAPAR over the Murray-Darling basin at 0.25° resolution July (top) to December 2019 (bottom). From left to right: model, satellite product, analysis, analysis-model difference. The latter shows the impact of assimilating LAI and SWI-001 on the simulated FAPAR. The color scale range of FAPAR values is 0 to 1.0. Areas with vegetation cover fraction less than 0.1 are left blank.

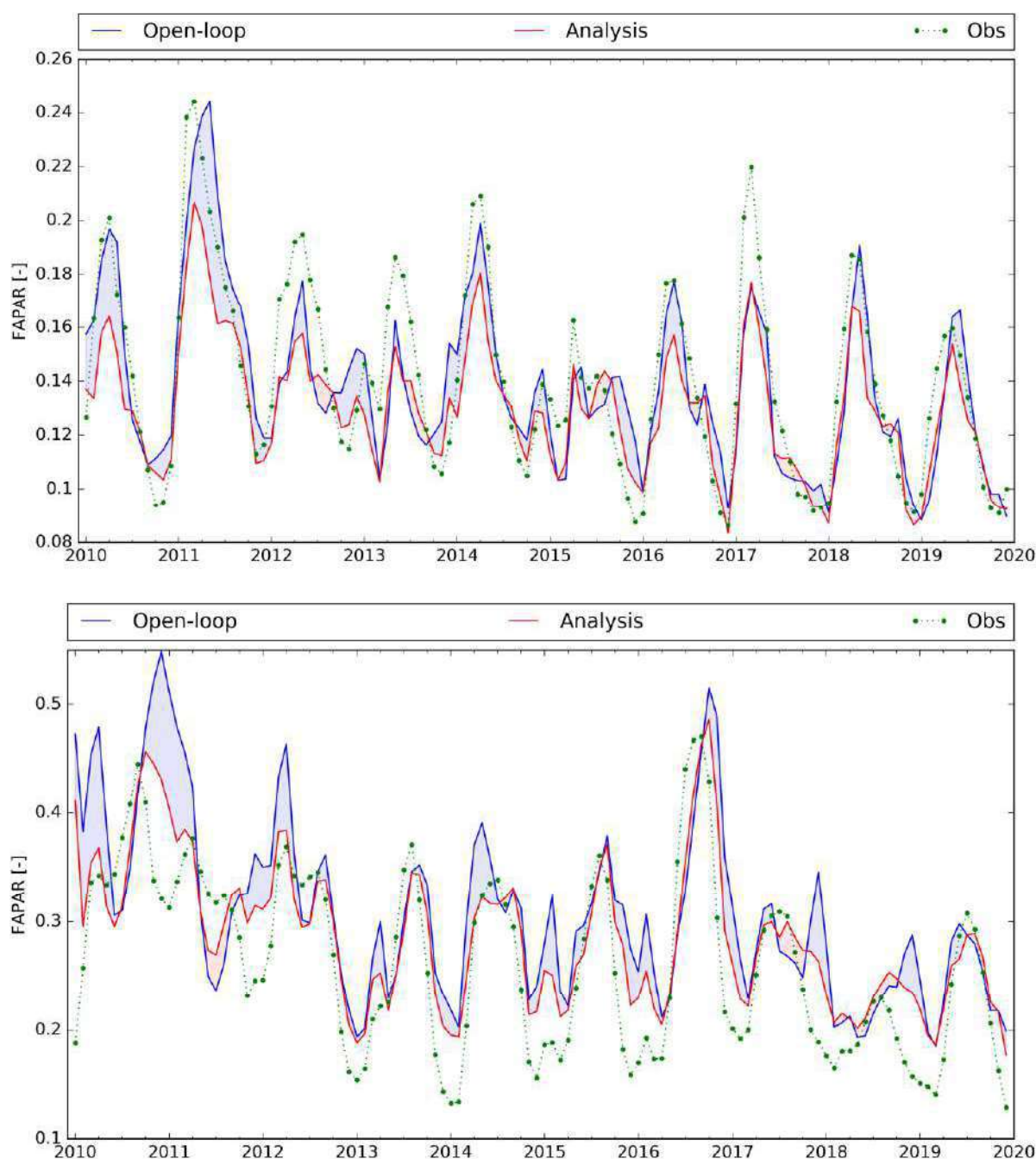


Figure 16: Monthly average values of FAPAR over Southern Africa (top) from 2010 to 2018, the Murray-Darling basin (bottom) from 2010 to 2018: model (blue line), satellite product (green circles), analysis (red line). Analysis-Model differences show the impact of assimilating LAI and SWI-001 on the simulated FAPAR.

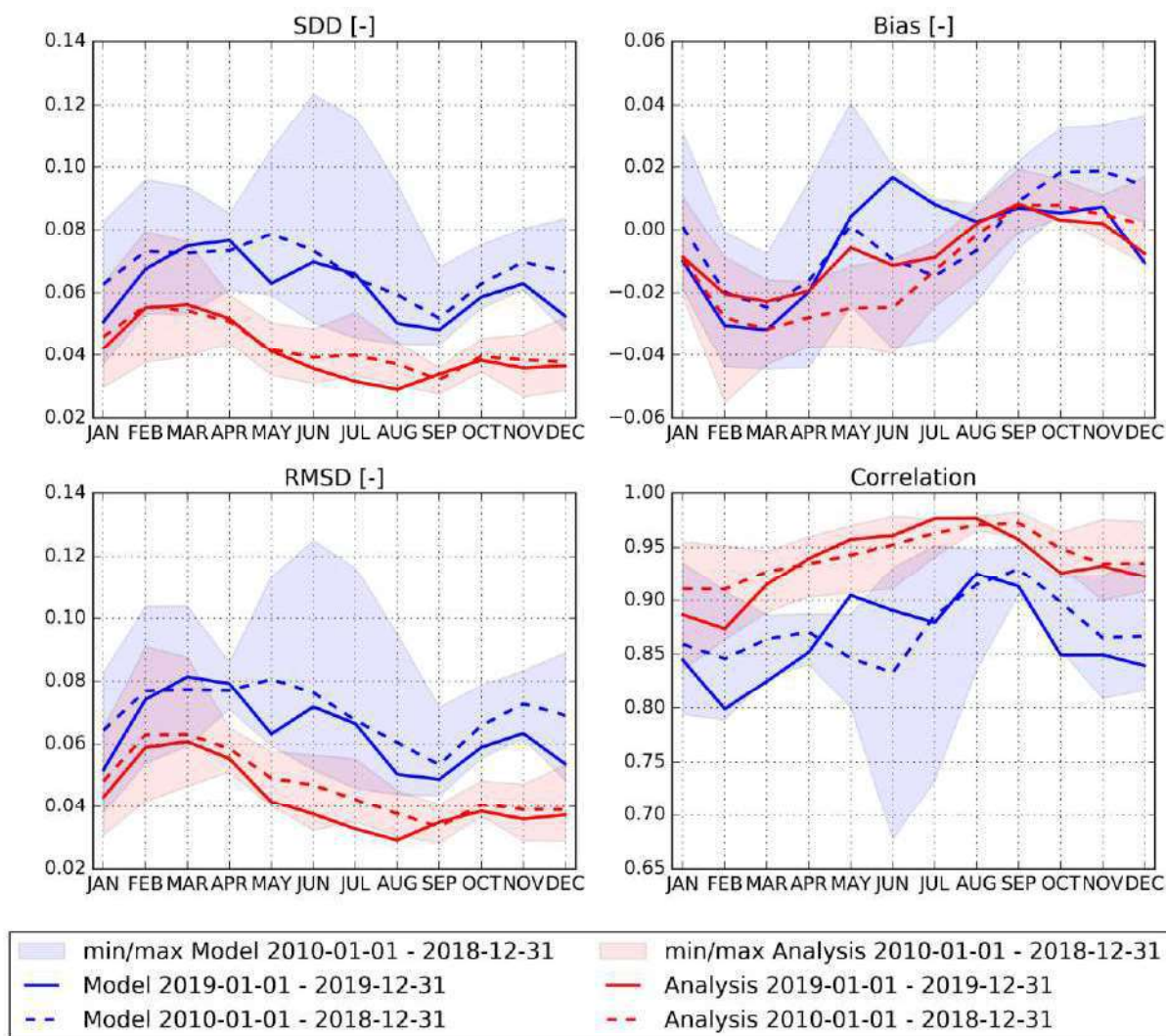


Figure 17: Monthly FAPAR scores of the model (blue) and analysis (red) when compared to the observations over Southern Africa at a 0.25° spatial resolution: from 2010 to 2018 (dashed lines), with N ranging from 28,315 in June to 28,323 in January-April, August-December; and for 2019 (solid lines), with N ranging from 3,145 in June to 3,150 in January, February, September-December. The monthly N values are indicated in the legend Table. Analysis-Model differences show the impact of assimilating LAI and SWI-001 on the simulated FAPAR. Shaded areas are between minimum and maximum score values recorded from 2010 to 2018.

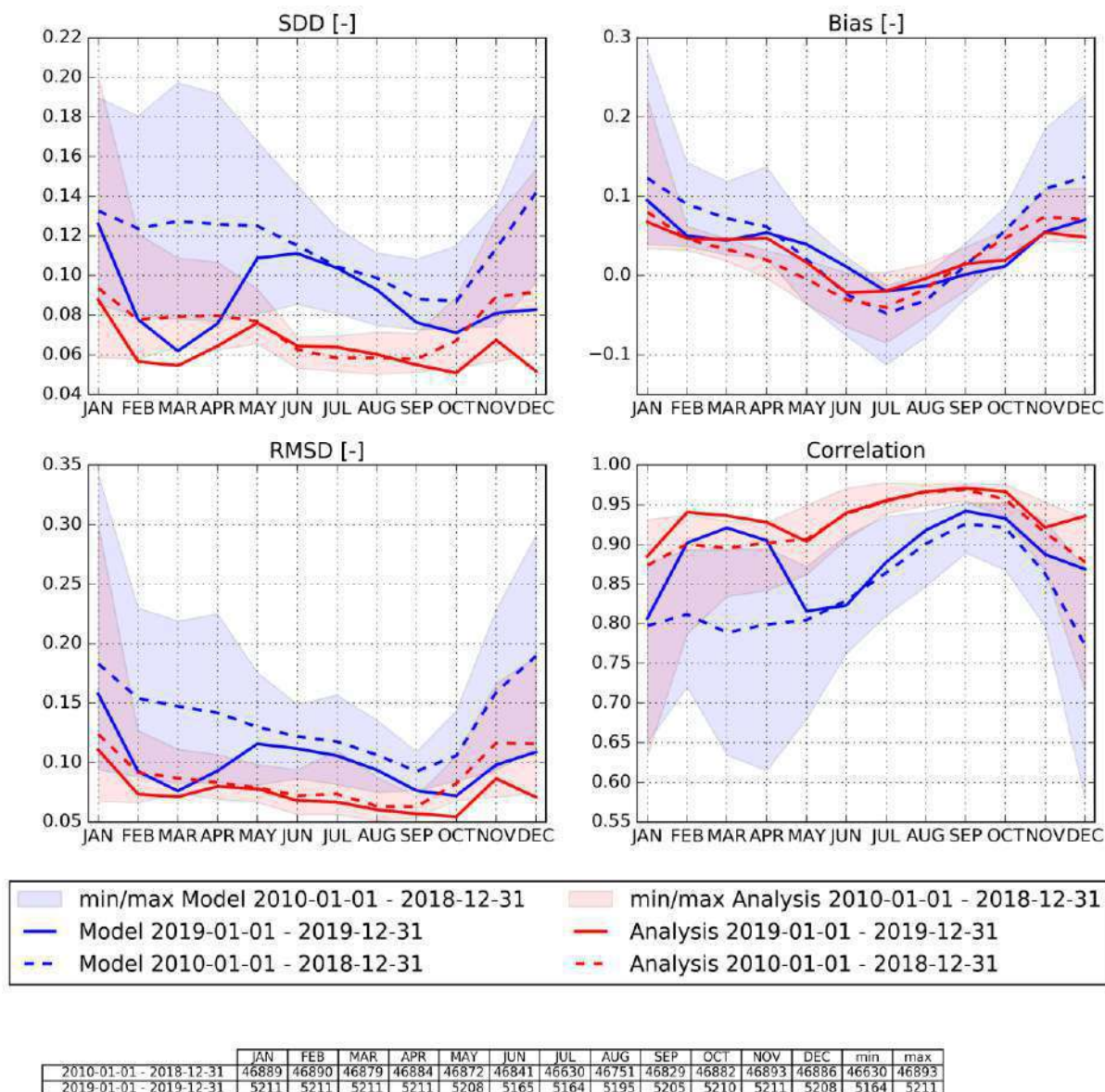


Figure 18: Monthly FAPAR scores of the model (blue) and analysis (red) when compared to the observations over the Murray-Darling basin at 0.25° spatial resolution: from 2010 to 2018 (dashed lines), with N ranging from 46,630 in July to 46,893 in November; and for 2019 (solid lines), with N ranging from 5,164 in July to 5,211 in November. The monthly N values are indicated in the legend Table. Analysis-Model differences show the impact of assimilating LAI and SWI-001 on the simulated FAPAR. Shaded areas are between minimum and maximum score values recorded from 2010 to 2018.

Table 4: Model and analysis FAPAR scores from 2010 to 2018 and for 2019 over Southern Africa (top), from 2010 to 2018 and for 2019 over the Murray-Darling basin (bottom). Analysis-Model differences show the impact of assimilating LAI and SWI-001 on the simulated FAPAR.

	Version	Bias	Correlation	RMSD	SDD	Nb_pts
2010-01-01 - 2018-12-31	Model	-0.002	0.861	0.072	0.072	339856
2010-01-01 - 2018-12-31	Analysis	-0.012	0.936	0.048	0.047	339856
2019-01-01 - 2019-12-31	Model	-0.004	0.860	0.064	0.064	37783
2019-01-01 - 2019-12-31	Analysis	-0.007	0.937	0.043	0.043	37783

	Version	Bias	Correlation	RMSD	SDD	Nb_pts
2010-01-01 - 2018-12-31	Model	0.047	0.806	0.146	0.138	562126
2010-01-01 - 2018-12-31	Analysis	0.025	0.904	0.093	0.090	562126
2019-01-01 - 2019-12-31	Model	0.033	0.873	0.103	0.097	62410
2019-01-01 - 2019-12-31	Analysis	0.026	0.933	0.074	0.070	62410

Conclusion for FAPAR:

Overall conclusions for FAPAR are similar to those for LAI, but over Southern Africa the assimilation of SSM and LAI introduces a FAPAR bias at the end of the vegetation growing period and during the senescence. This result may denote an inconsistency between the rescaled SWI-001 product and LAI caused by a dramatic change in climatic conditions at the end of the 2010-2019 time period.

Over Southern Africa, during the drought period from August to October 2019, both modelled and analyzed FAPAR tend to present better SDD and RMSD scores values than those observed during the 2010-2018 reference period of time (Figure 17).

Over the Murray-Darling basin, peak FAPAR values lower than normal are observed (Figure 16). In relation to these small FAPAR values, both model and analysis scores in 2019 tend to present better than average values (Figure 18, Table 4), apart from the May-August period.

For both Southern Africa and the Murray-Darling basin, the model bias presents a marked seasonality (Figure 17, Figure 18). This is caused by a delayed (and advanced, respectively) peak FAPAR date in the model simulations (Figure 16). This could be attributed to biases in the ERA5 radiation forcing of the model (Urraca et al., 2018). While the FAPAR bias seasonality is markedly reduced by the assimilation in the case of the Murray-Darling basin (Figure 18, Table 4), the mean bias tends to increase over Southern Africa (Table 4).

Figure 12 and Figure 13 show that the assimilation of SSM and LAI observations tends to reinforce the drought signal over Southern Africa from May to December 2019, with smaller FAPAR values in the analysis in the area of Kimberley from May to August, and in the area of Cape Town from April to December. Figure 14 and Figure 15 show that the assimilation of SSM and LAI observations markedly reduces FAPAR values over the southeastern part of the Murray-Darling basin, from January to June, and in December.

6 RESULTS FOR SURFACE ALBEDO

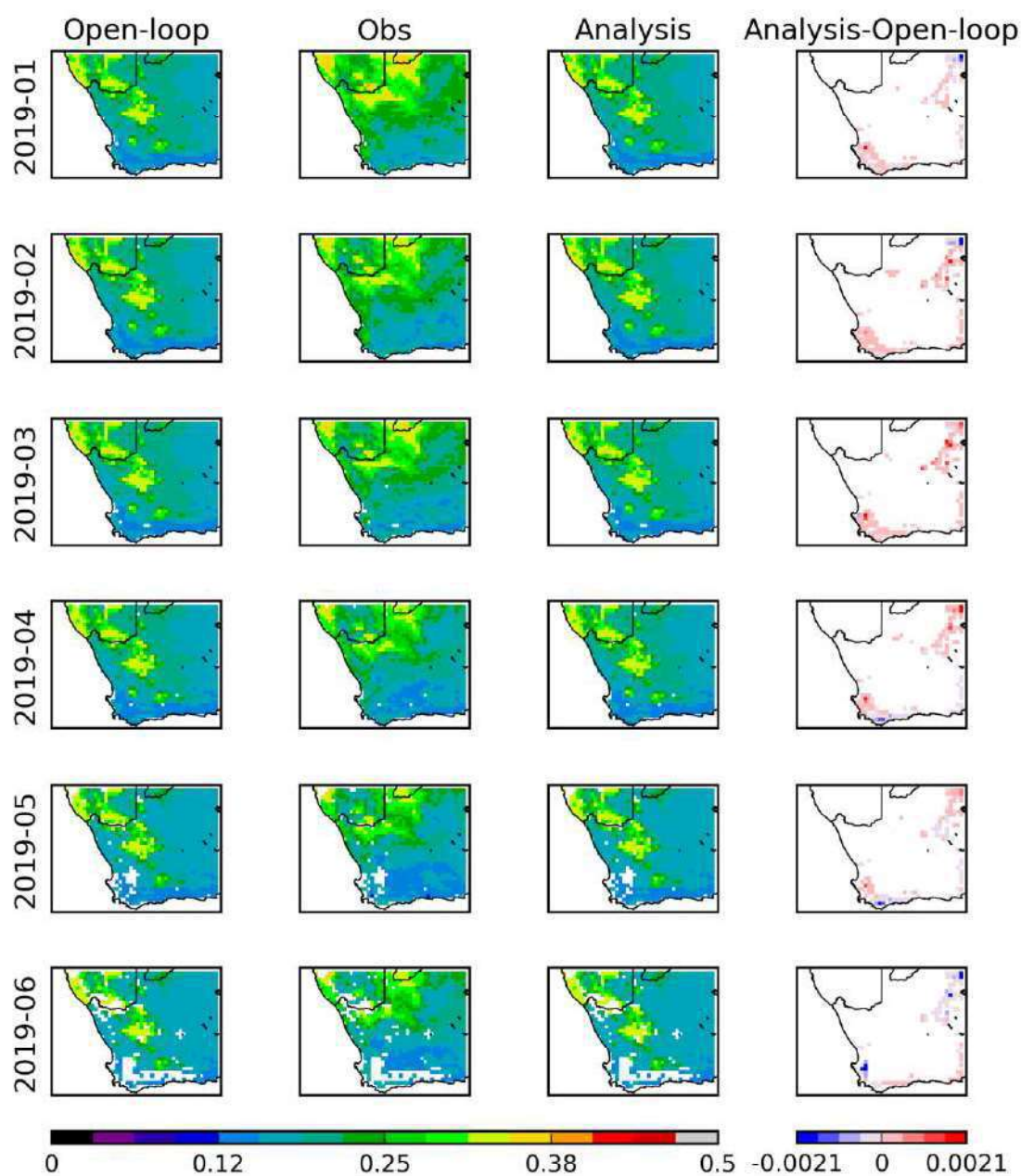


Figure 19: Monthly average values of Surface Albedo over Southern Africa at 0.25° spatial resolution from January (top) to June 2019 (bottom). From left to right: model, satellite product, analysis, analysis-model difference. The latter shows the impact of assimilating LAI and SWI-001 on the simulated SA. The color scale range of SA values is 0 to 0.5. Areas with missing data are left blank.

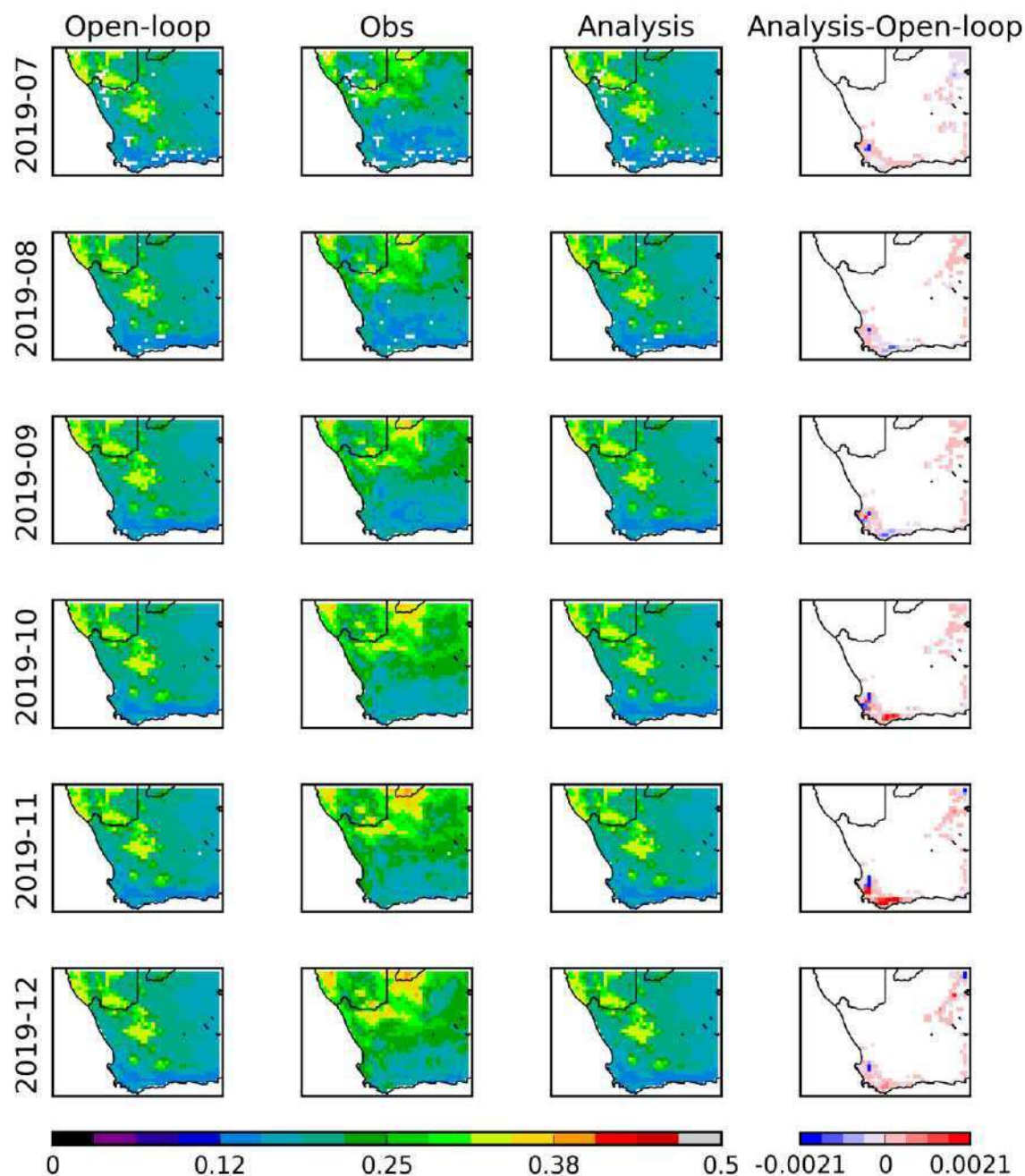


Figure 20: Monthly average values of Surface Albedo over Southern Africa at 0.25° spatial resolution from July (top) to December 2019 (bottom). From left to right: model, satellite product, analysis, analysis-model difference. The latter shows the impact of assimilating LAI and SWI-001 on the simulated SA. The color scale range of SA values is 0 to 0.5. Areas with missing data are left blank.

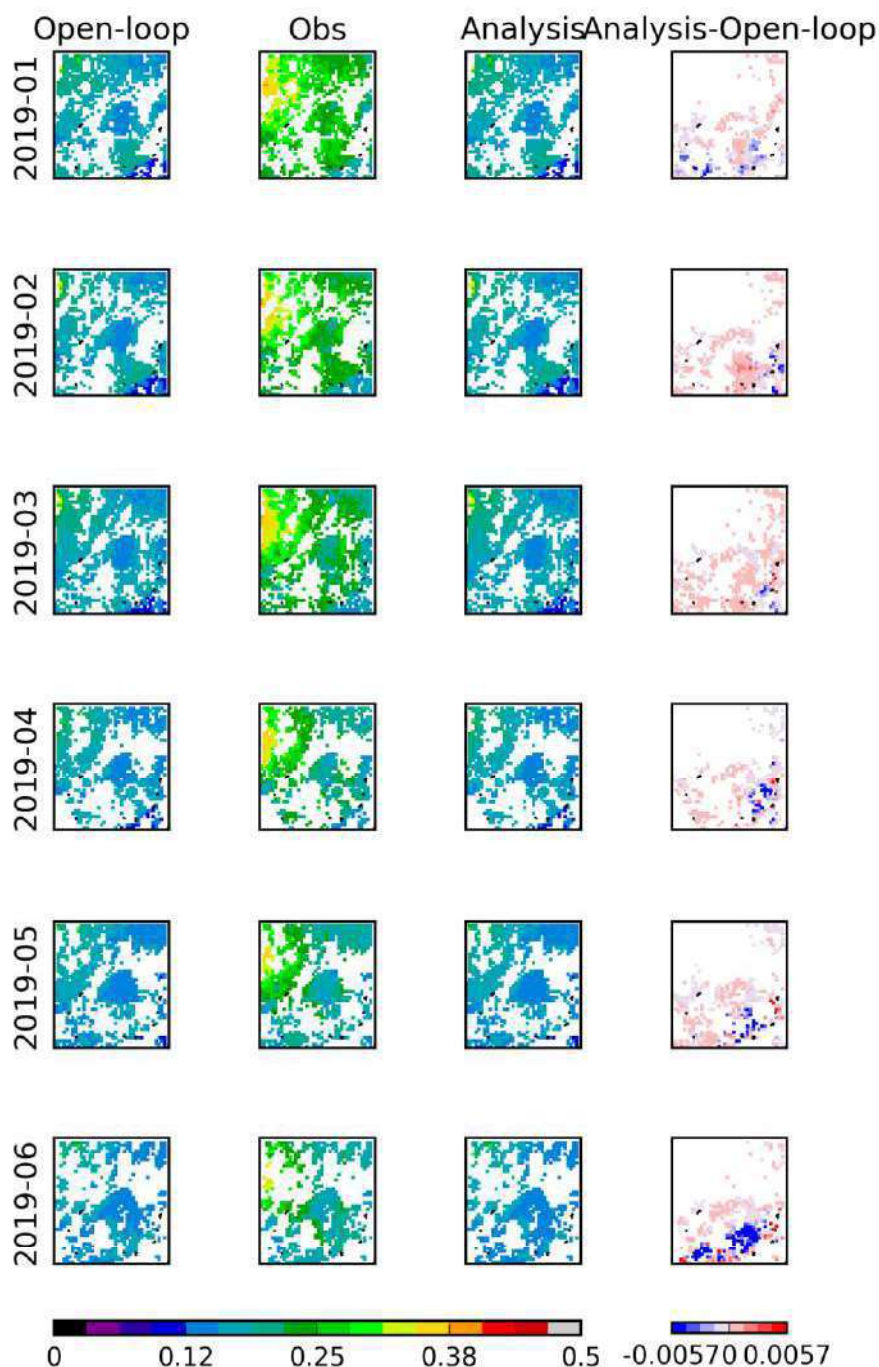


Figure 21: Monthly average values of Surface albedo over the Murray-Darling basin at 0.25° spatial resolution from January (top) to June 2019 (bottom). From left to right: model, satellite product, analysis, analysis-model difference. The latter shows the impact of assimilating LAI and SWI-001 on the simulated SA. The color scale range of SA values is 0 to 0.5. Areas with missing data are left blank.

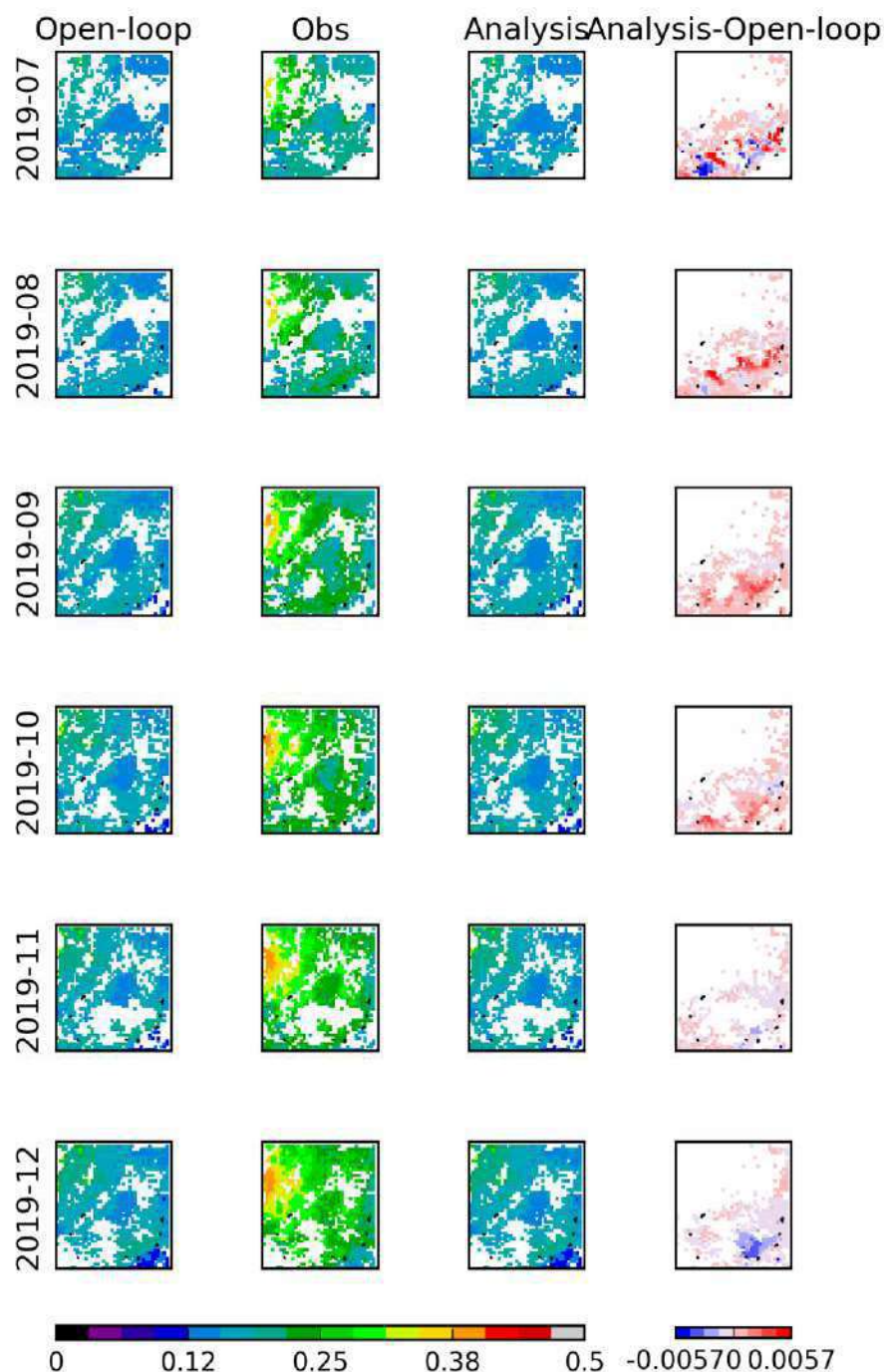


Figure 22: Monthly average values of Surface albedo over the Murray-Darling basin at 0.25° spatial resolution from July (top) to December 2019 (bottom). From left to right: model, satellite product, analysis, analysis-model difference. The latter shows the impact of assimilating LAI and SWI-001 on the simulated SA. The color scale range of SA values is 0 to 0.5. Areas with missing data are left blank.

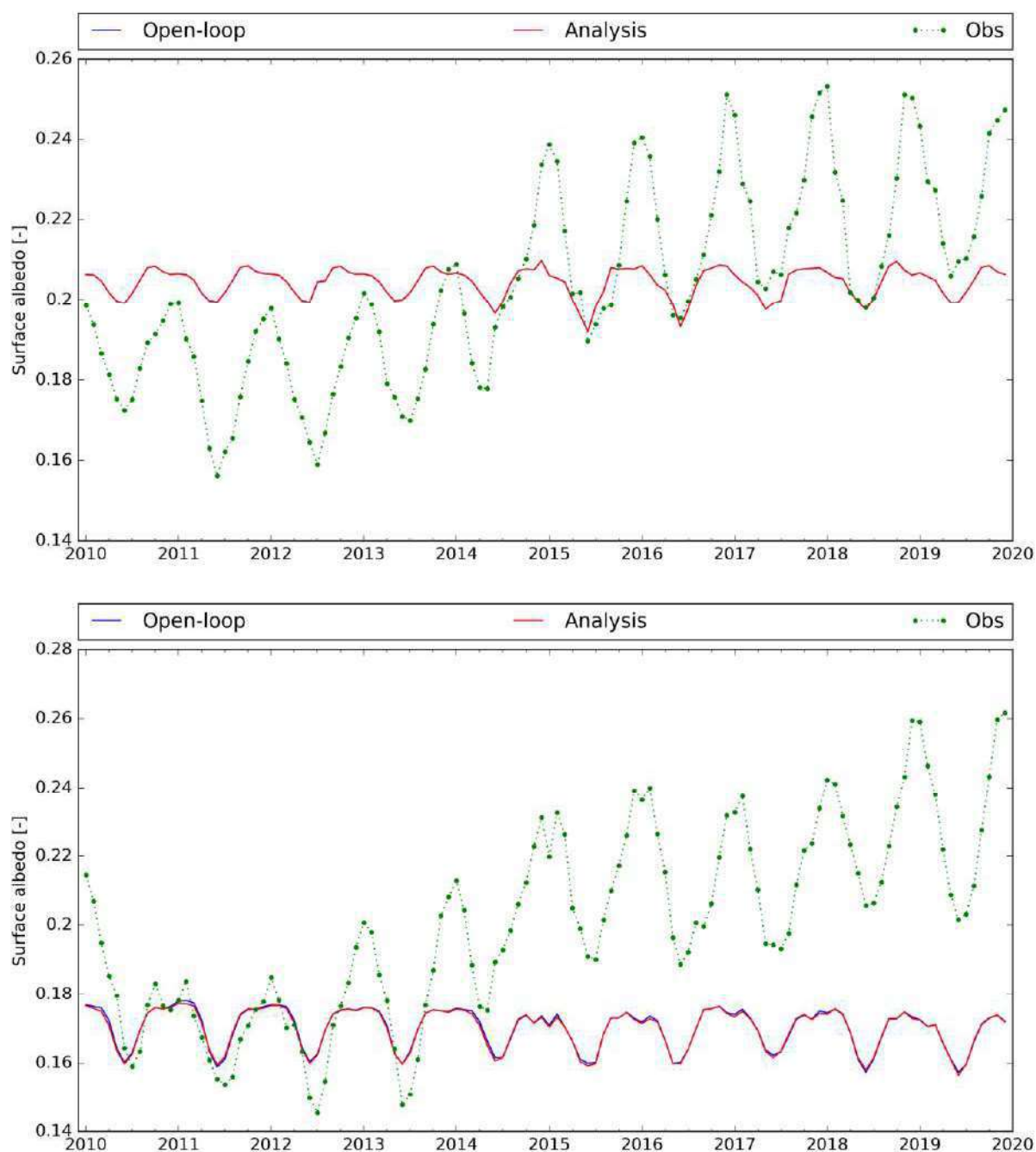


Figure 23: Monthly average values of SA over Southern Africa (top) from 2010 to 2019, the Murray-Darling basin (bottom) from 2010 to 2019: model (blue line), satellite product (green circles), analysis (red line). Analysis-Model differences show the impact of assimilating LAI and SWI-001 on the simulated SA. (Note that model and analysis curves are often superimposed).

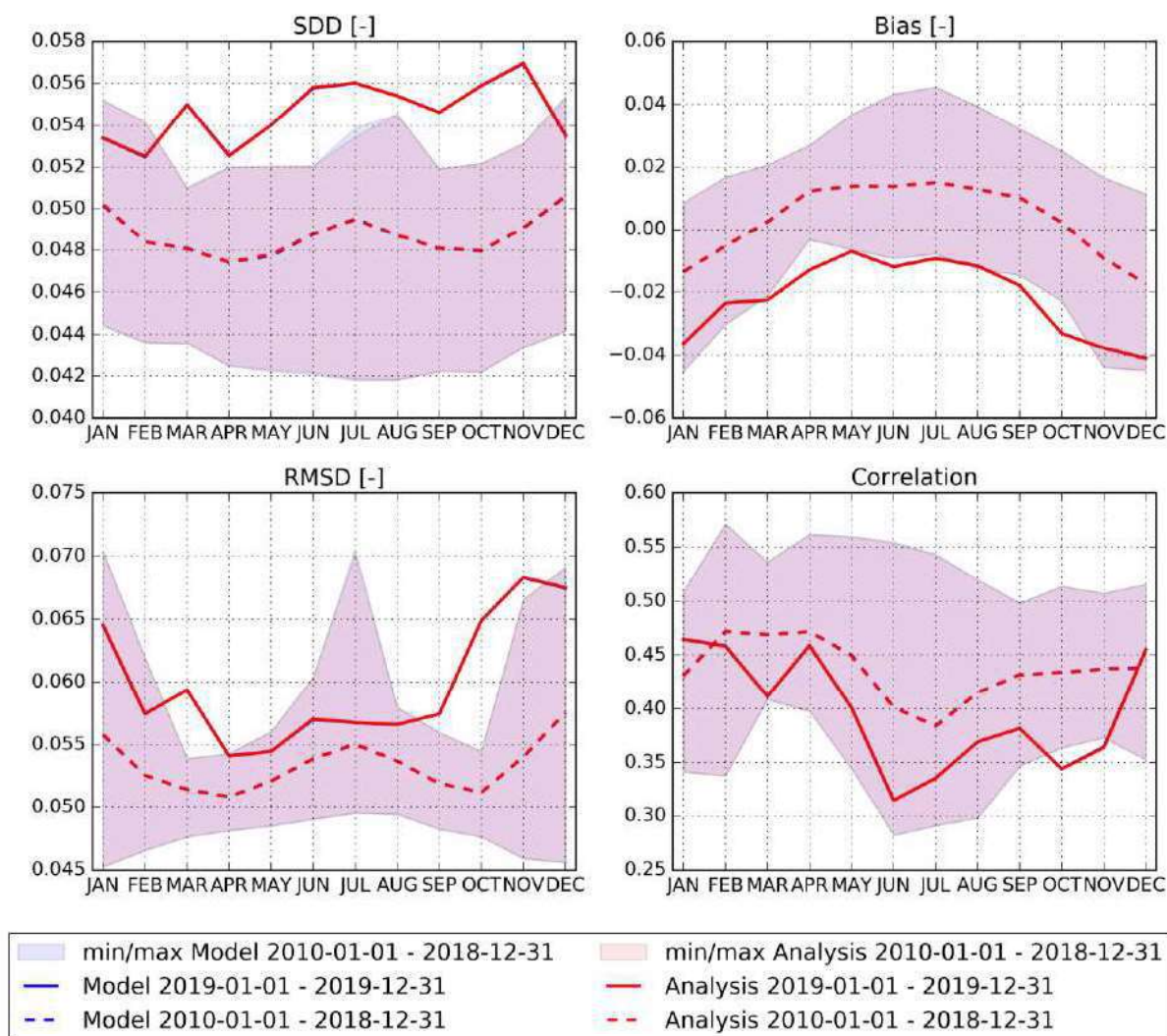


Figure 24: Monthly SA scores of the model (blue) and analysis (red) when compared to the observations over Southern Africa at a 0.25° spatial resolution: from 2010 to 2018 (dashed lines), with N ranging from 27,291 in January to 30,750 in September; and for January to December 2019 (solid lines), with N ranging from 2,686 in June to 3,490 in February. The monthly N values are indicated in the legend Table. Analysis-Model differences show the impact of assimilating LAI and SWI-001 on the simulated SA. (Note that model and analysis curves are nearly completely superimposed).

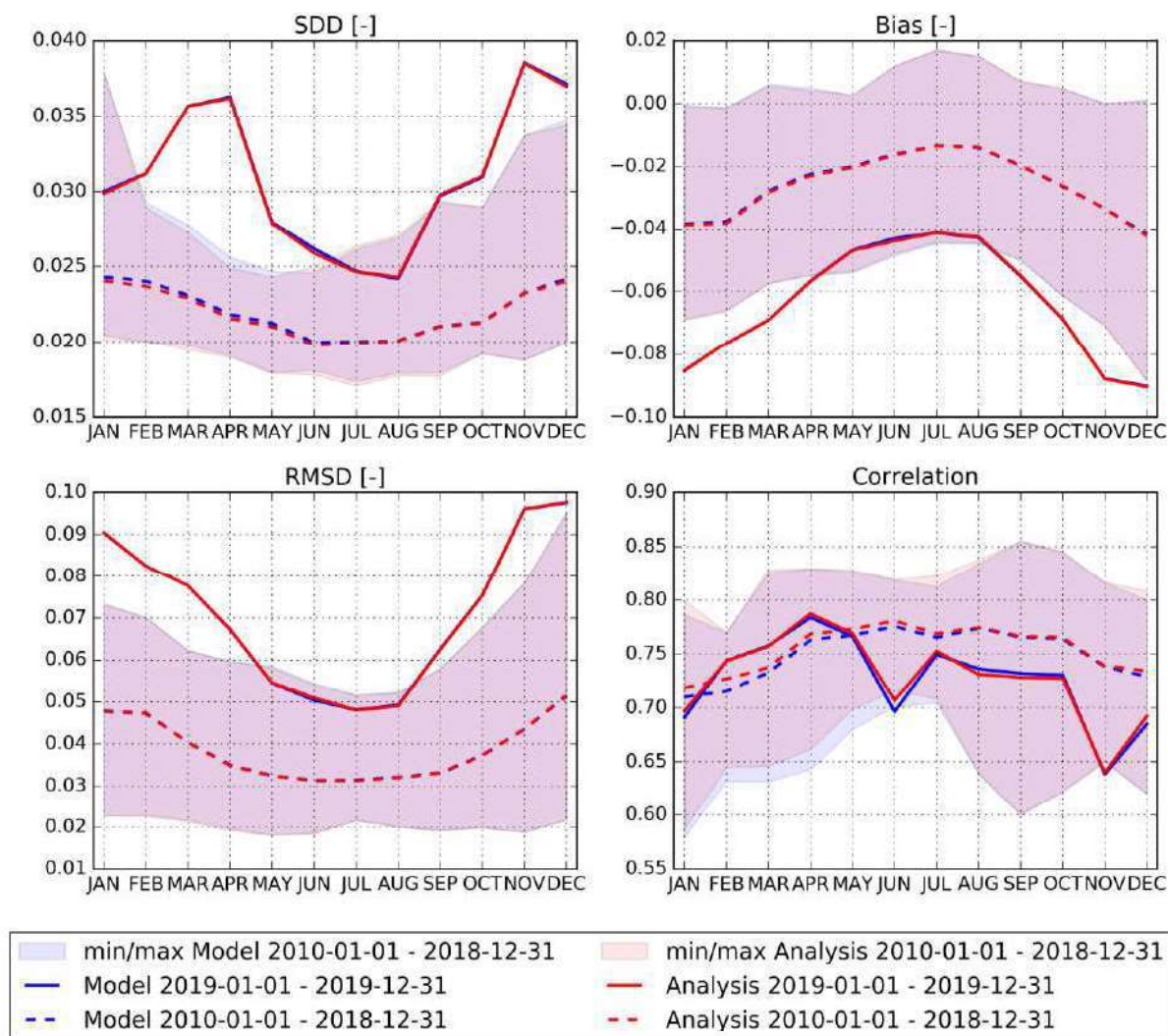


Figure 25: Monthly SA scores of the model (blue) and analysis (red) when compared to the observations over the Murray-Darling basin at 0.25° spatial resolution: from 2010 to 2018 (dashed lines), with N ranging from 36,703 in December to 42,707 in April; and for January to December 2019 (solid lines), with N ranging from 1,357 in June to 2,828 in December. The monthly N values are indicated in the legend Table. Analysis-Model differences show the impact of assimilating LAI and SWI-001 on the simulated SA. (Note that model and analysis curves are often superimposed).

Table 5: Model and analysis SA scores from 2010 to 2018 and for 2019 over Southern Africa (top), the Murray-Darling basin (bottom). Analysis-Model differences show the impact of assimilating LAI and SWI-001 on the simulated SA.

	Version	Bias	Correlation	RMSD	SDD	Nb_pts
2010-01-01 - 2018-12-31	Model	0.005	0.401	0.053	0.053	348417
2010-01-01 - 2018-12-31	Analysis	0.005	0.401	0.053	0.053	348417
2019-01-01 - 2019-12-31	Model	-0.023	0.400	0.060	0.056	39631
2019-01-01 - 2019-12-31	Analysis	-0.023	0.400	0.060	0.056	39631

	Version	Bias	Correlation	RMSD	SDD	Nb_pts
2010-01-01 - 2018-12-31	Model	-0.022	0.592	0.040	0.033	484451
2010-01-01 - 2018-12-31	Analysis	-0.022	0.596	0.040	0.033	484451
2019-01-01 - 2019-12-31	Model	-0.065	0.721	0.075	0.036	24685
2019-01-01 - 2019-12-31	Analysis	-0.065	0.721	0.075	0.036	24685

Conclusion for Surface Albedo:

Contrary to LAI and FAPAR, the SA scores in 2019 (Table 5) do not present better values than during the 2010-2018 reference period of time. Particularly large SDD values are observed over Southern Africa from March to November 2019 (Figure 24). The same result is found over the Murray-Darling basin from March to May and from October to December 2019 (Figure 25). Table 5 indicates that in 2019 SDD and RMSD scores are worse over both Southern Africa and the Murray-Darling basin. Correlation is better over the Murray-Darling basin. The bias is also much more pronounced in 2019, especially over the Murray-Darling basin (Table 5, Figure 25). This can be at least partly attributed to the transition between SPOT-VGT and PROBA-V in 2014. A discontinuity in mean observed SA values is clearly visible in May 2014, when data from SPOT-VGT were replaced by data from PROBA-V (Figure 23). The SA values tend to present higher values after this date (see Section 9.2 for a detailed comparison).

Over the Murray-Darling basin, the marked decrease in LAI values from 2016, to 2019 (Figure 9) corresponds to a marked increase in SA (Figure 23). This is consistent with the observed impact of the assimilation in 2019 from January to June and in December: the assimilation tends to reduce SA values (Figure 21, Figure 22) in areas where LAI is increased (Figure 6, Figure 7) and SSM is decreased (Figure 28, Figure 29). This relationship is less obvious at the end of the growing period (from July to September) and during the senescence (October and November).

Over the Murray-Darling basin, the number of SA observations (Table 5) is smaller than for LAI (Table 3) and FAPAR (Table 4). In 2019, N for SA is 60% smaller than N for FAPAR. For example, only 1357 SA observations are available over this area in June, against 5165 for FAPAR.

7 RESULTS FOR SWI-001

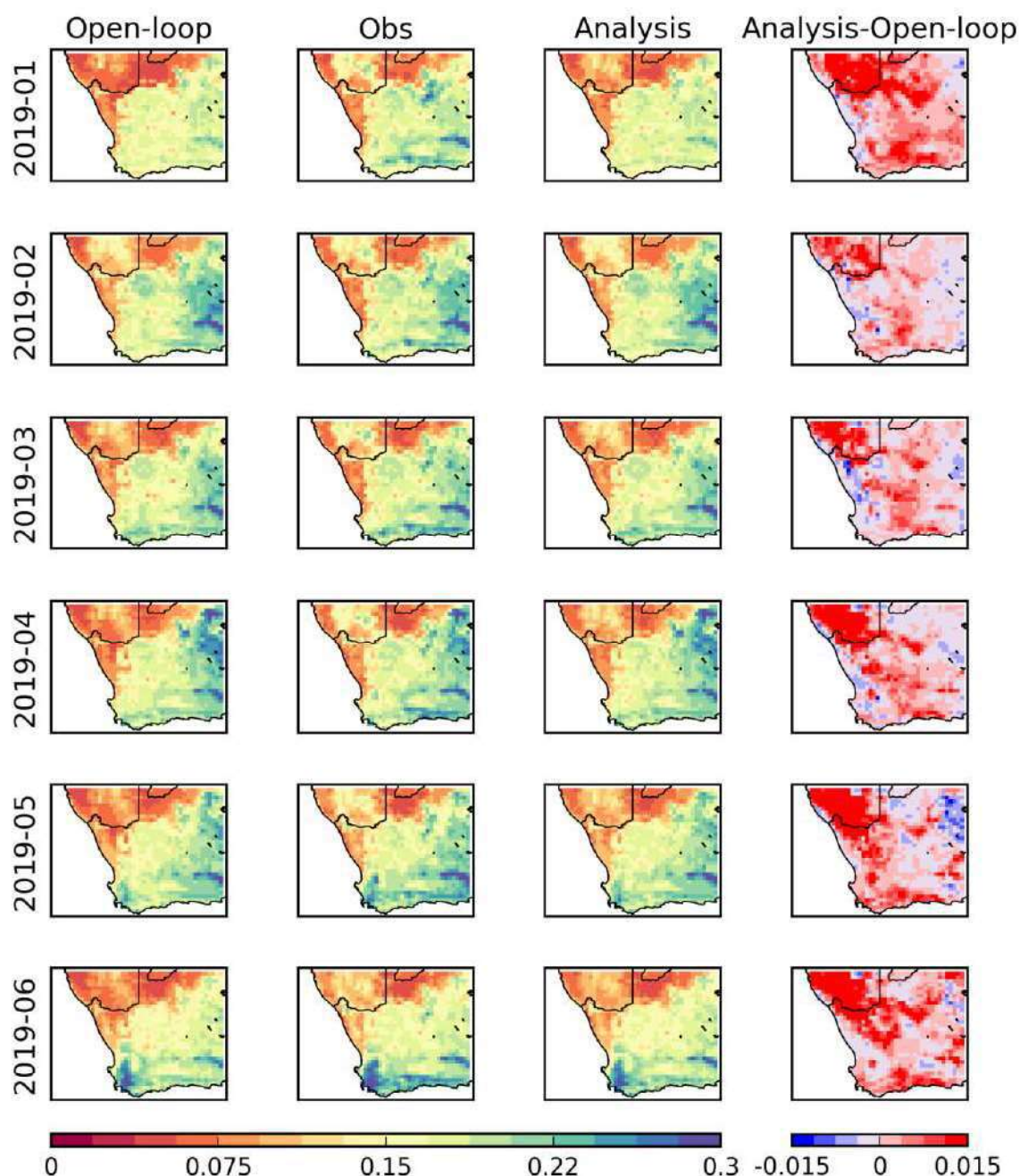


Figure 26: Monthly average values of SSM over Southern Africa at 0.25° spatial resolution from January (top) to June 2019 (bottom). From left to right: model, rescaled satellite product after CDF matching, analysis, analysis-model difference. The latter shows the impact of assimilating LAI and SWI-001 on the simulated SSM. The color scale range of SSM values is 0 to 0.3 m³m⁻³.

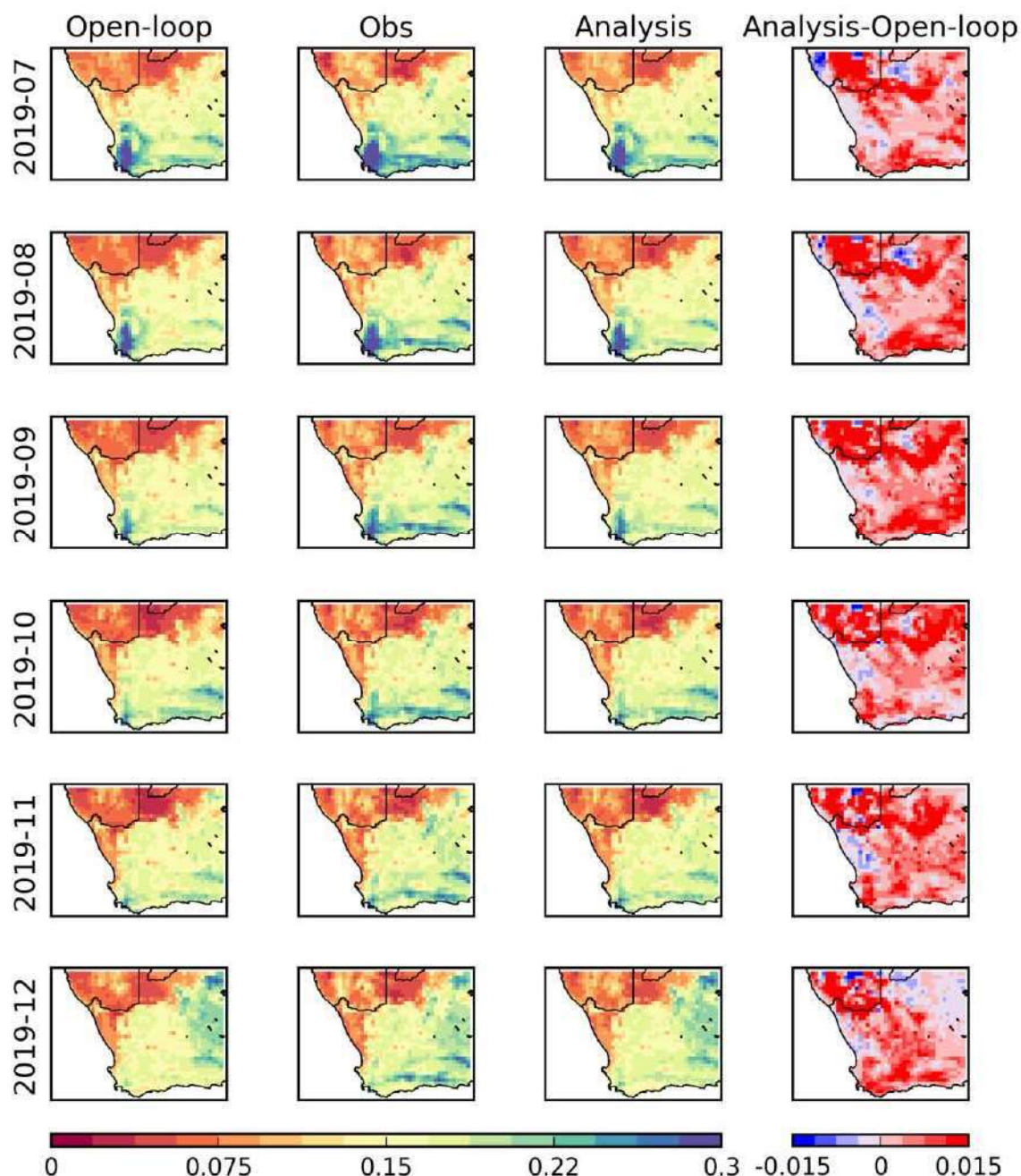


Figure 27: Monthly average values of SSM over Southern Africa at 0.25° spatial resolution from July (top) to December 2019 (bottom). From left to right: model, rescaled satellite product after CDF matching, analysis, analysis-model difference. The latter shows the impact of assimilating LAI and SWI-001 on the simulated SSM. The color scale range of SSM values is 0 to 0.3 m³m⁻³.

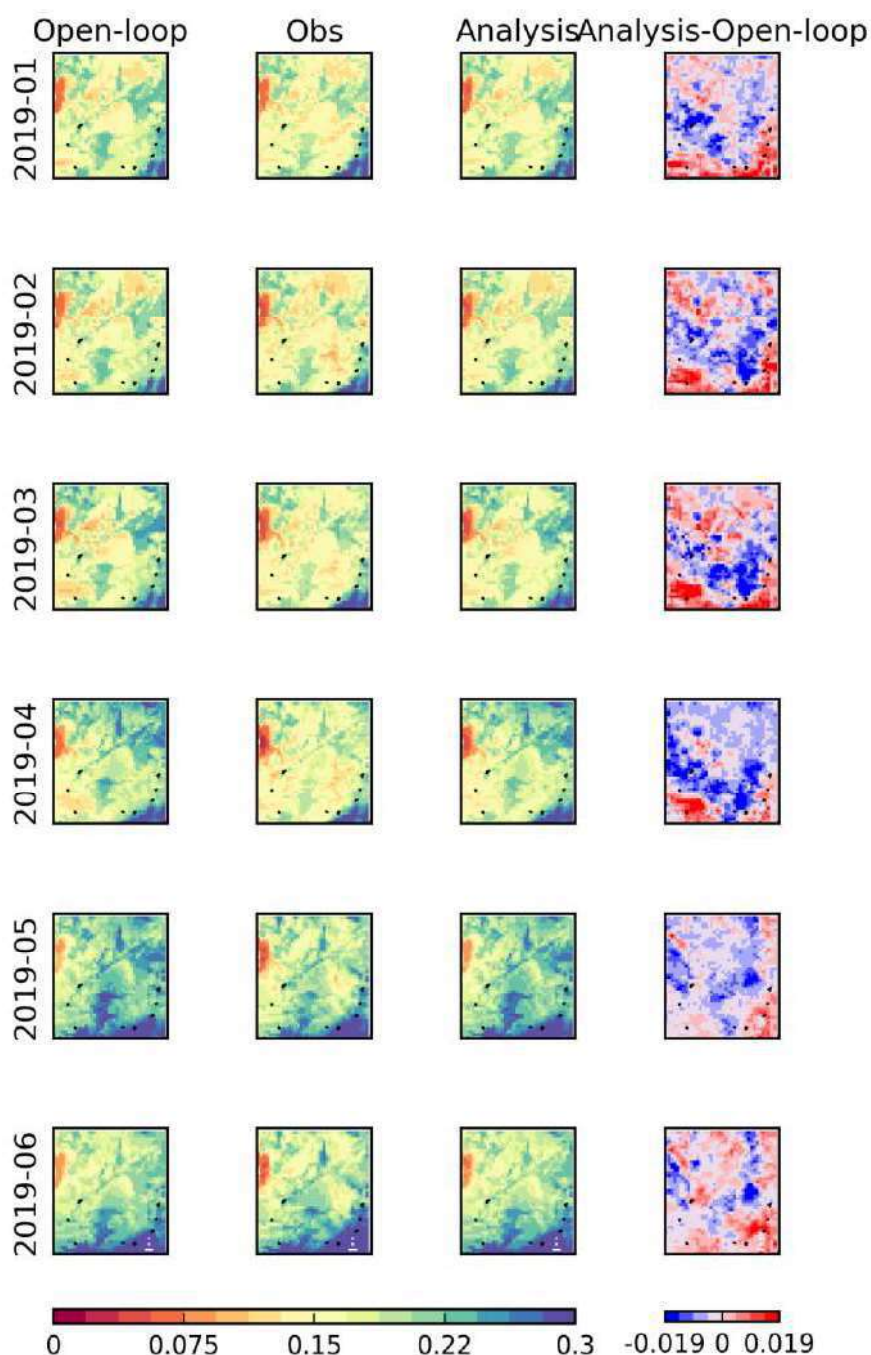


Figure 28: Monthly average values of SSM over the Murray-Darling basin at 0.25° spatial resolution from January (top) to June 2019 (bottom). From left to right: model, rescaled satellite product after CDF matching, analysis, analysis-model difference. The latter shows the impact of assimilating LAI and SWI-001 on the simulated SSM. The color scale range of SSM values is 0 to 0.3 m³m⁻³. Areas with missing data are left blank.

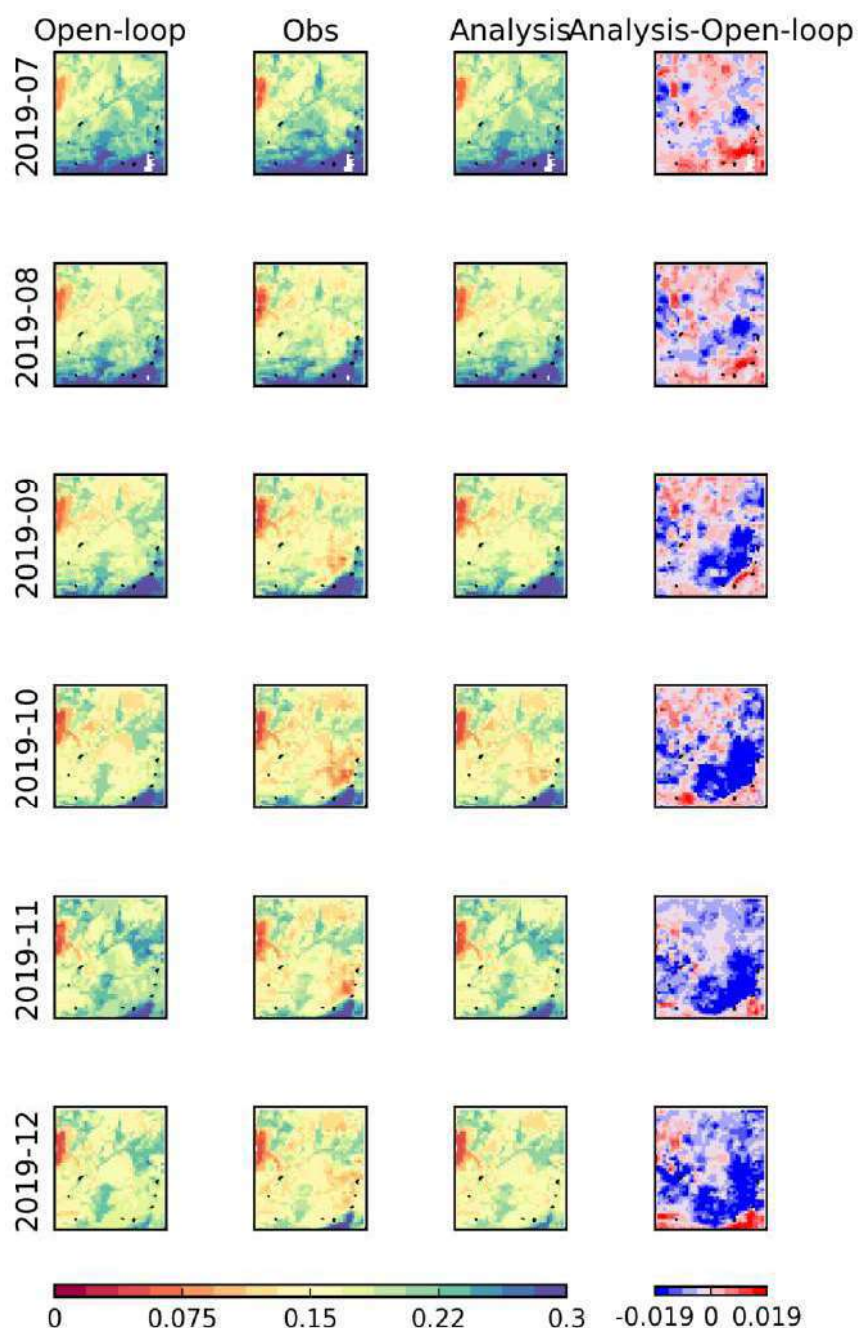


Figure 29: Monthly average values of SSM over the Murray-Darling basin at 0.25° spatial resolution from July (top) to December 2019 (bottom). From left to right: model, rescaled satellite product after CDF matching, analysis, analysis-model difference. The latter shows the impact of assimilating LAI and SWI-001 on the simulated SSM. The color scale range of SSM values is 0 to 0.3 m³m⁻³. Areas with missing data are left blank.

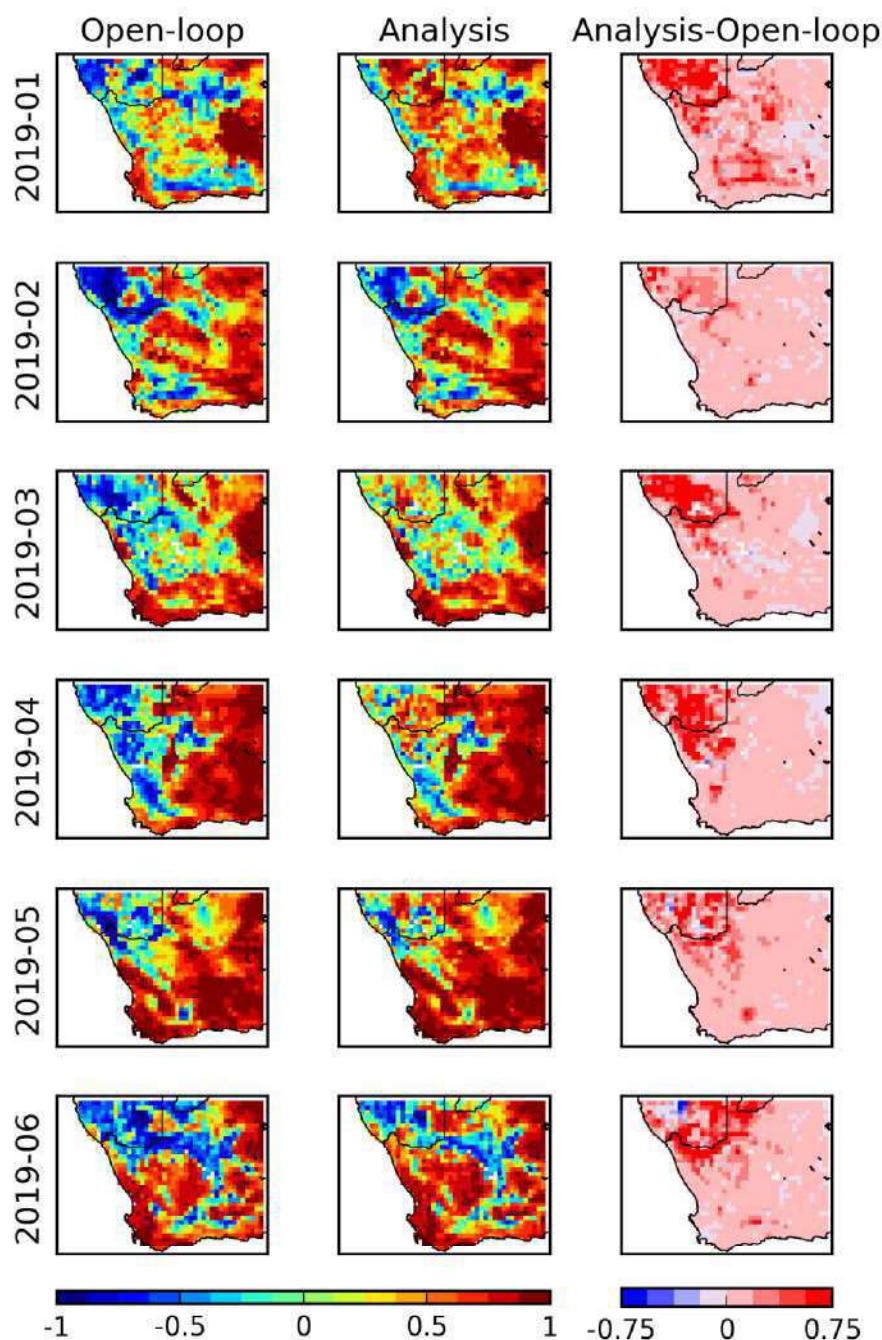


Figure 30: Monthly correlation maps between the rescaled SWI-001 product time series after CDF matching and the modeled SSM (left), and the analyzed SSM (middle) over Southern Africa at 0.25° spatial resolution from January (top) to June 2019 (bottom). Analysis-Model differences show the impact of assimilating LAI and SWI-001 on the simulated SSM. The color scale range of R values is -1.0 to 1.0.

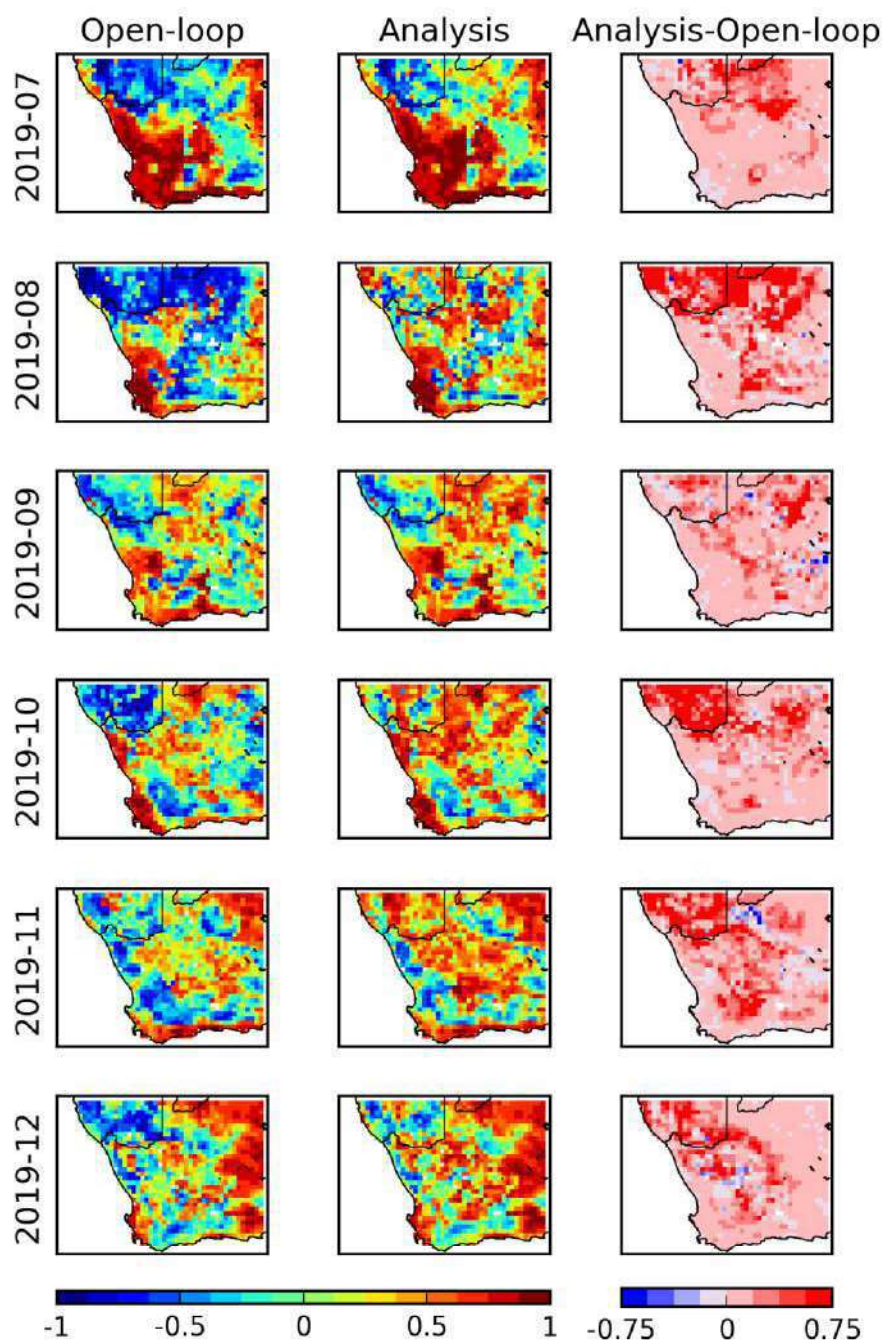


Figure 31: Monthly correlation maps between the rescaled SWI-001 product time series after CDF matching and the modeled SSM (left), and the analyzed SSM (middle) over Southern Africa at 0.25° spatial resolution from July (top) to December 2019 (bottom). Analysis-Model differences show the impact of assimilating LAI and SWI-001 on the simulated SSM. The color scale range of R values is -1.0 to 1.0.

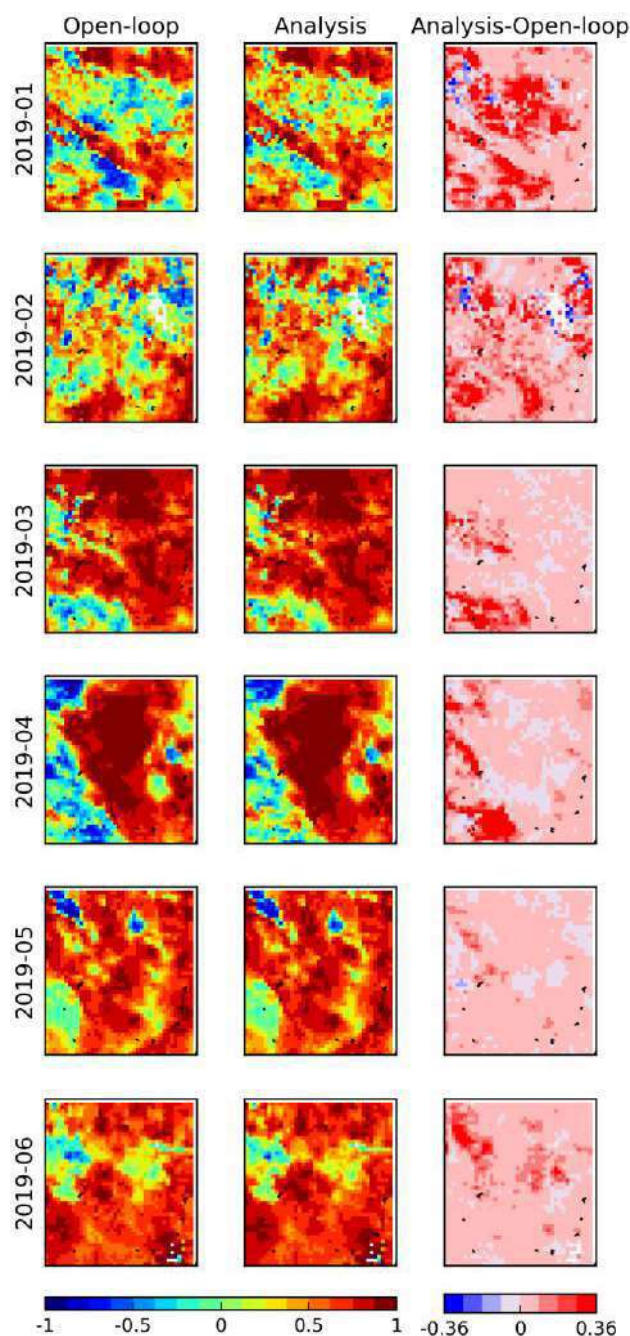


Figure 32: Monthly correlation maps between the rescaled SWI-001 product time series after CDF matching and the modeled SSM (left), and the analyzed SSM (middle) over the Murray-Darling basin at 0.25° spatial resolution from January (top) to June 2019 (bottom). Analysis-Model differences show the impact of assimilating LAI and SWI-001 on the simulated SSM. The color scale range of R values is -1.0 to 1.0. Areas with missing data are left blank.

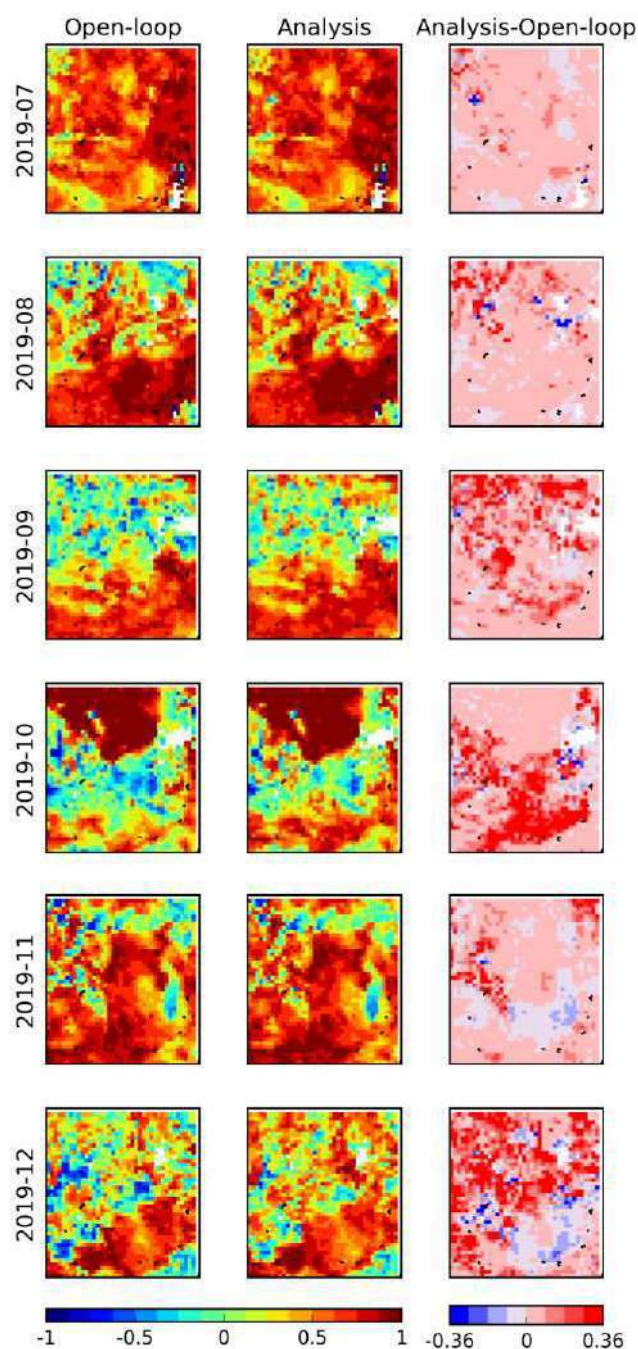


Figure 33: Monthly correlation maps between the rescaled SWI-001 product time series after CDF matching and the modeled SSM (left), and the analyzed SSM (middle) over the Murray-Darling basin at 0.25° spatial resolution from July (top) to December 2019 (bottom). Analysis-Model differences show the impact of assimilating LAI and SWI-001 on the simulated SSM. The color scale range of R values is -1.0 to 1.0. Areas with missing data are left blank.

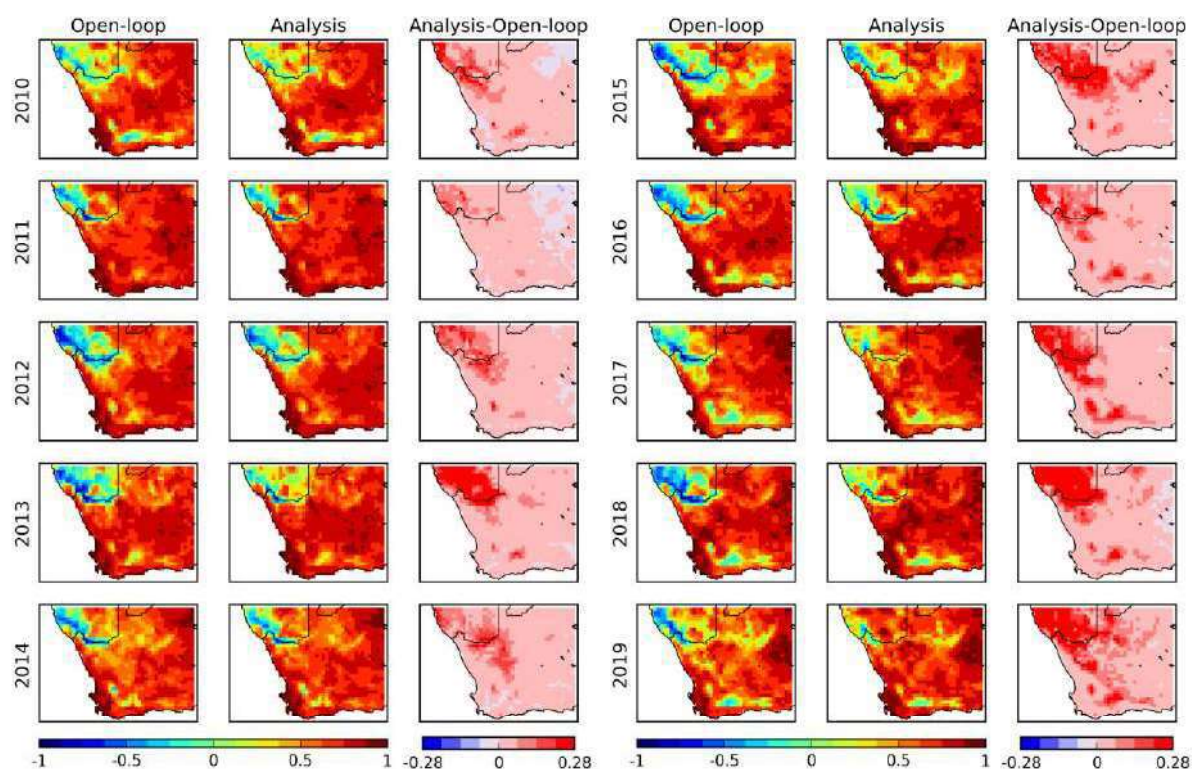


Figure 34: Yearly correlation maps between the rescaled SWI-001 product time series after CDF matching and the modeled SSM (left), and the analyzed SSM (middle) over Southern Africa at 0.25° resolution from 2010 to 2019. Analysis-Model differences show the impact of assimilating LAI and SWI-001 on the simulated SSM. The color scale range of R values is -1.0 to 1.0.

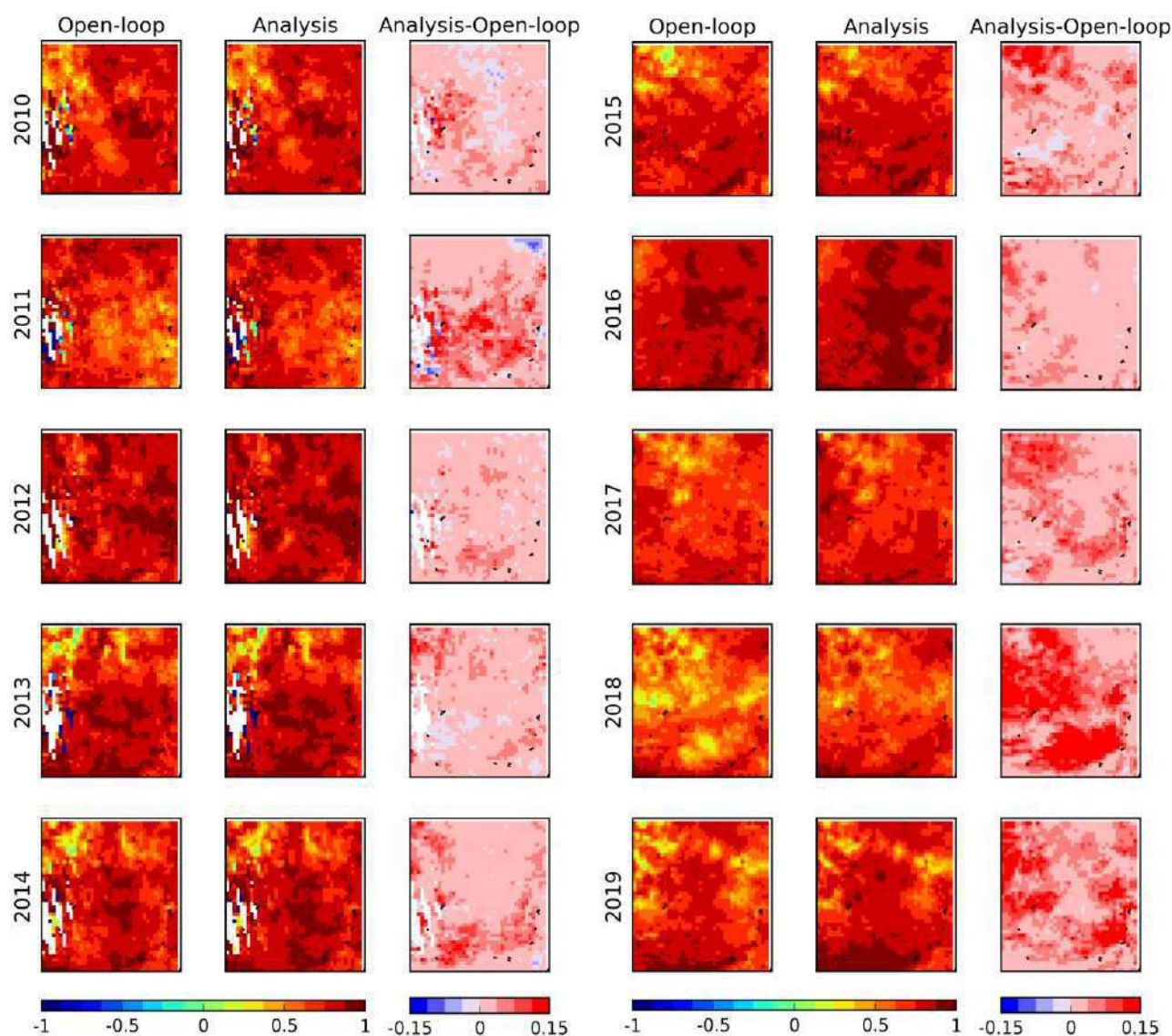


Figure 35: Yearly correlation maps between the rescaled SWI-001 product time series after CDF matching and the modeled SSM (left), and the analyzed SSM (middle) over the Murray-Darling basin at 0.25° resolution from 2010 to 2019. Analysis-Model differences show the impact of assimilating LAI and SWI-001 on the simulated SSM. The color scale range of R values is -1.0 to 1.0. Areas with missing data are left blank.

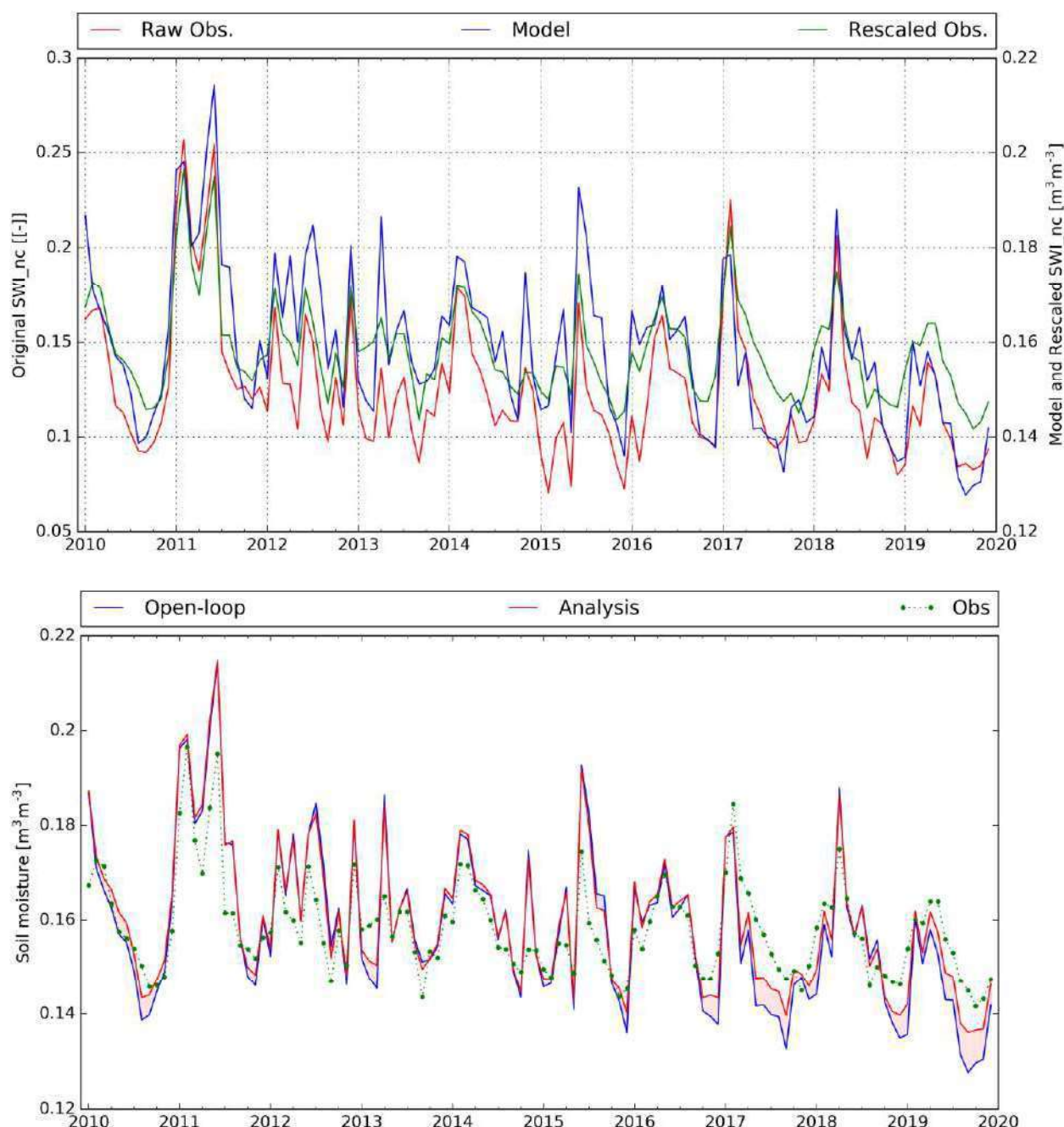


Figure 36: Monthly average values of SSM over Southern Africa from 2010 to 2019. Top panel: original SWI-001 (red), model SSM used for CDF-matching (blue), rescaled SWI-001 product (green). Bottom panel: model (blue, same as on the top graph), rescaled SWI-001 product (green), analysis (red). Analysis-Model differences show the impact of assimilating LAI and SWI-001 on the simulated SSM.

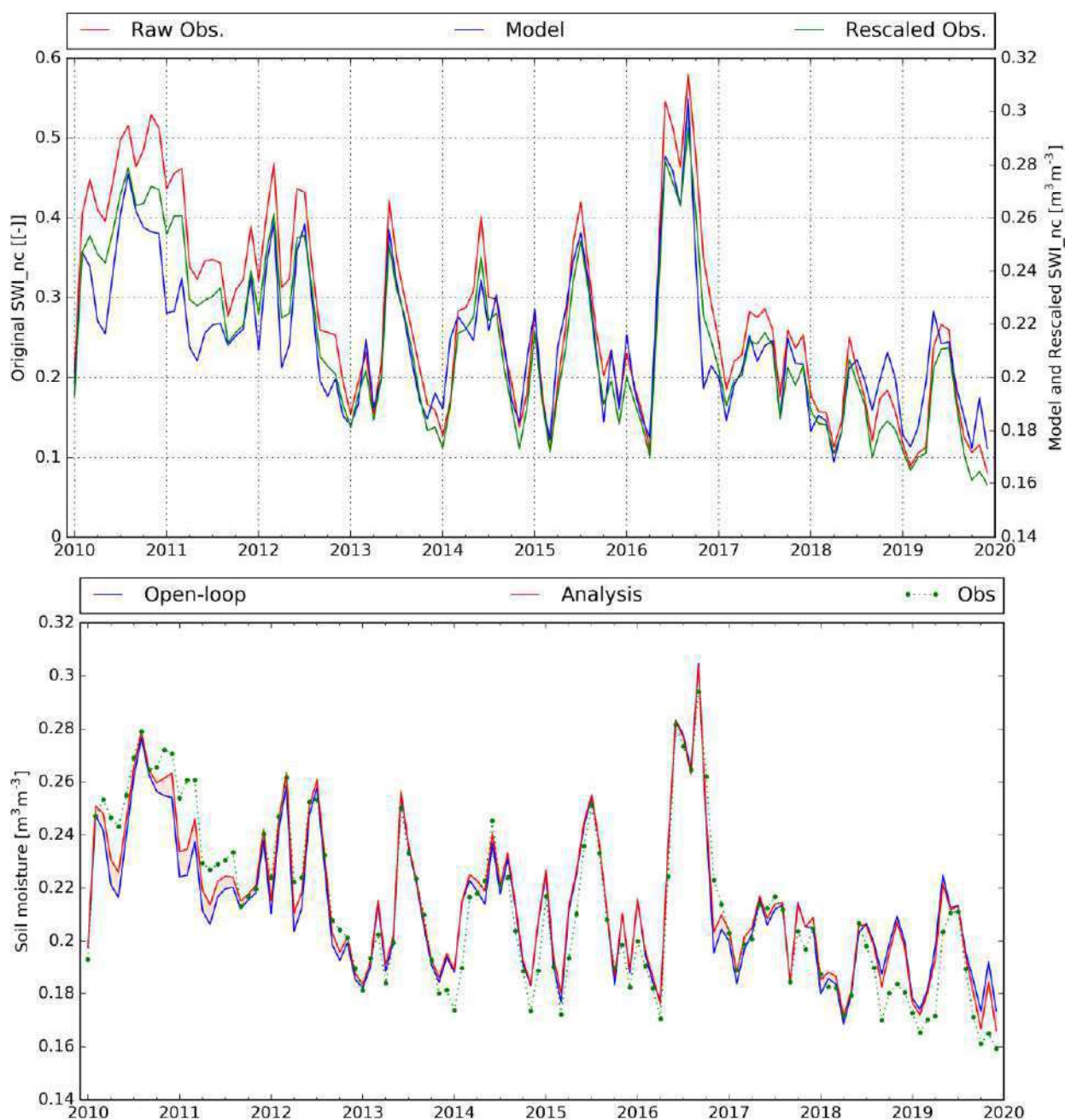


Figure 37: Monthly average values of SSM over the Murray-Darling basin from 2010 to 2019. Top panel: original SWI-001 (red), model SSM used for CDF-matching (blue), rescaled SWI-001 product (green). Bottom panel: model (blue, same as on the top graph), rescaled SWI-001 observations (green), analysis (red). Analysis-Model differences show the impact of assimilating LAI and SWI-001 on the simulated SSM.

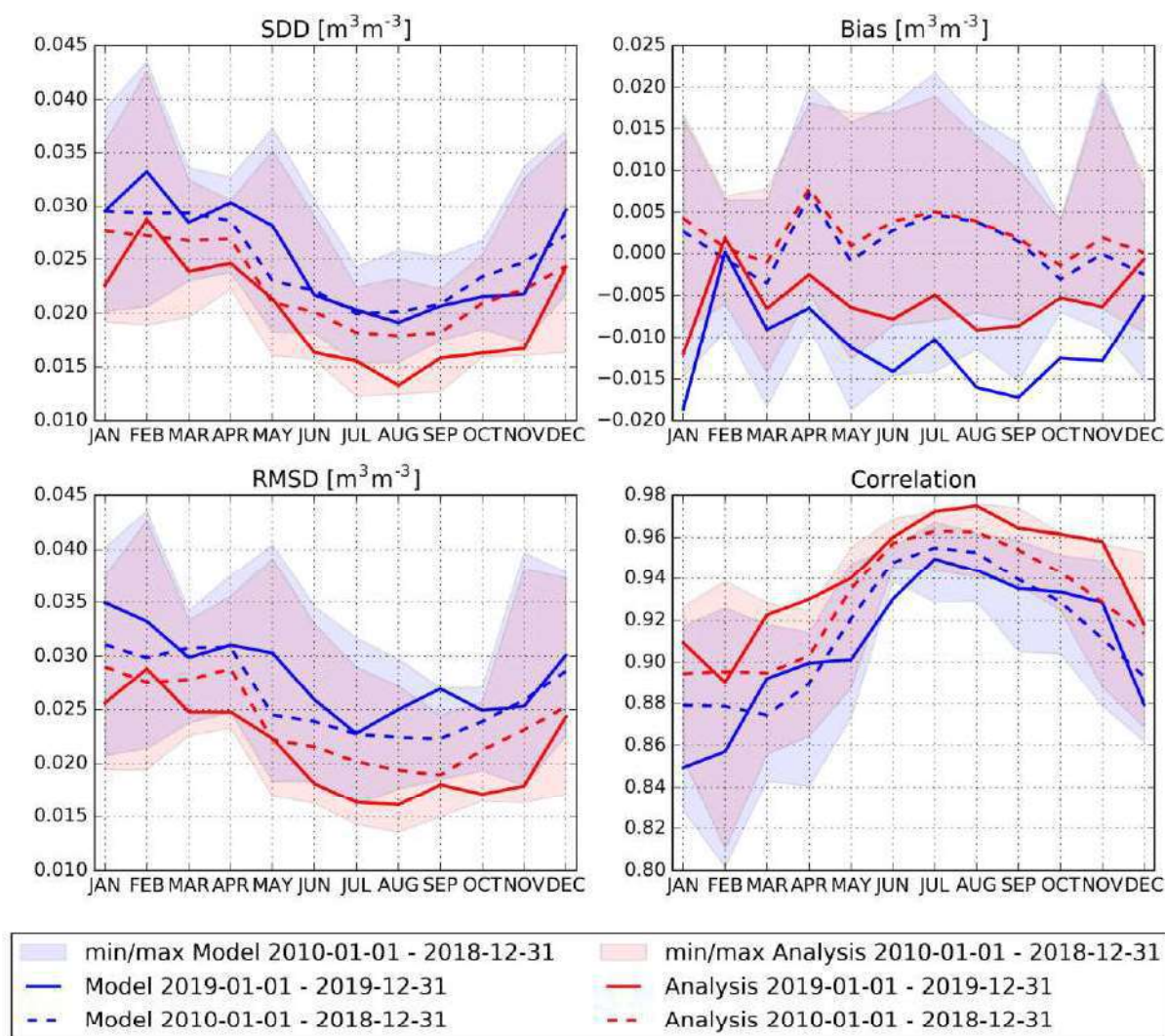


Figure 38: Monthly SSM scores of the model (blue) and analysis (red) when compared to the rescaled SWI-001 over Southern Africa at 0.25° spatial resolution: for all data from 2010 to 2018 (dashed lines), with N ranging from 39,163 in January to 2,448,876 in August, and for data in 2019 (solid lines), with N ranging from 1,530 in February to 41,868 in July. The monthly N values are indicated in the legend Table. Analysis-Model differences show the impact of assimilating LAI and SWI-001 on the simulated SSM. Shaded areas are between minimum and maximum score values recorded from 2010 to 2018.

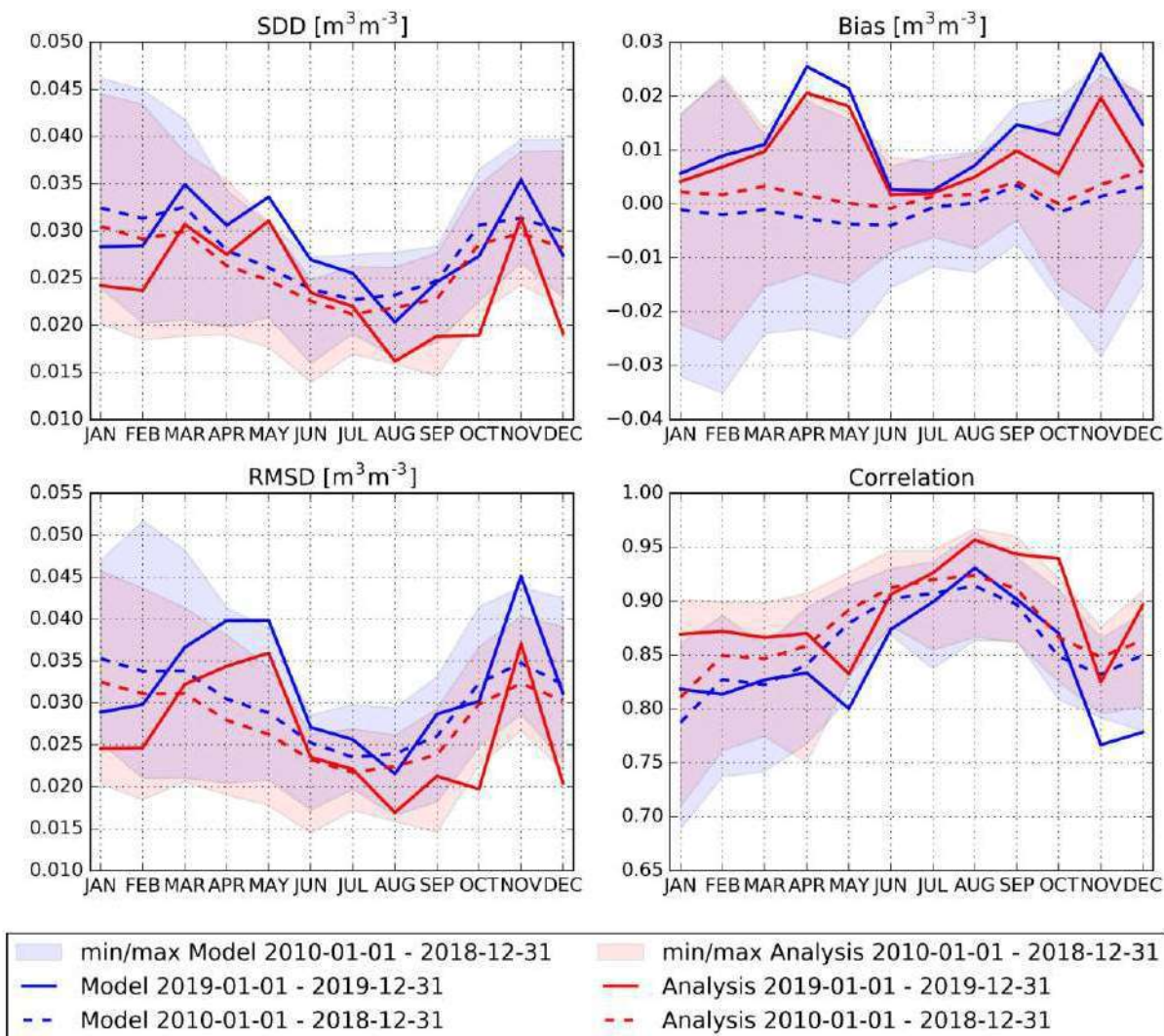


Figure 39: Monthly SSM scores of the model (blue) and analysis (red) when compared to the rescaled SWI-001 over the Murray-Darling basin at 0.25° spatial resolution: for all data from 2010 to 2018 (dashed lines), with N ranging from 118,513 in February to 169,957 in November, and for data in 2019 (solid lines), with N ranging from 39,454 in February to 44,720 in October. The monthly N values are indicated in the legend Table. Analysis-Model differences show the impact of assimilating LAI and SWI-001 on the simulated SSM. Shaded areas are between minimum and maximum score values recorded from 2010 to 2018.

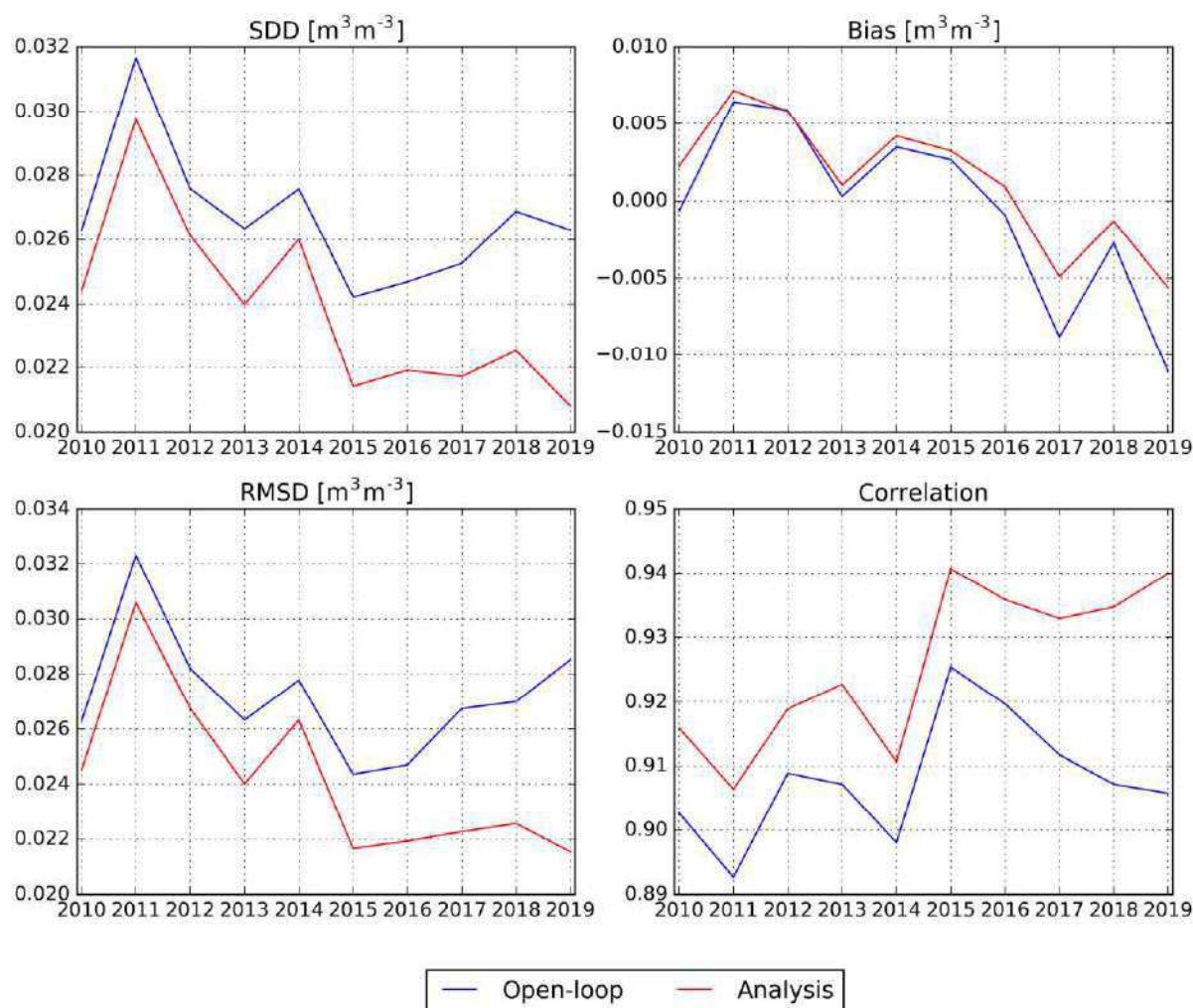
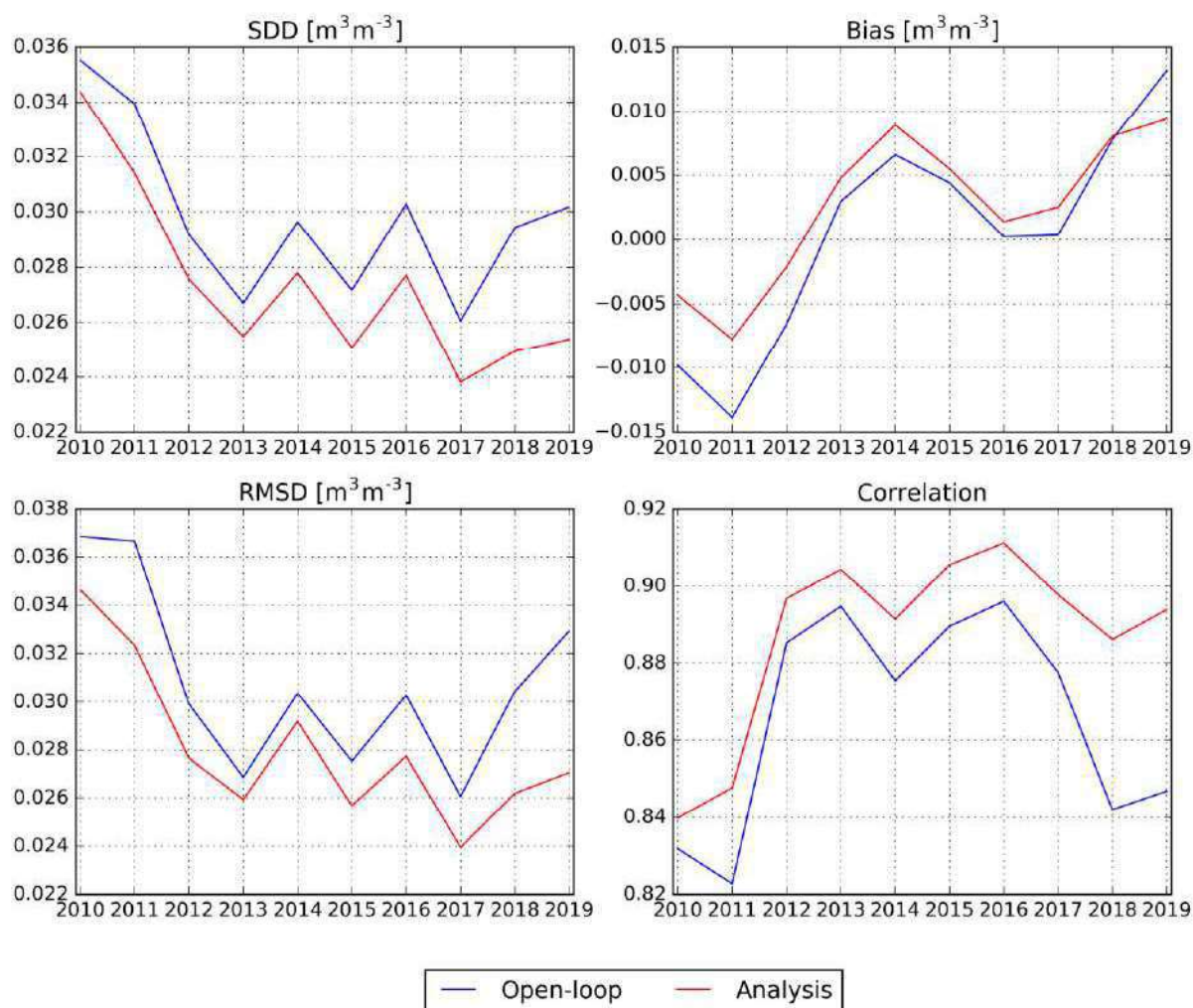


Figure 40: Annual scores of the model (blue) and analysis (red) when compared to the rescaled SWI-001 over Southern Africa at 0.25° spatial resolution, with N ranging from 140,118 in 2011 to 260,019 in 2019. The yearly N values are indicated in the legend Table. Analysis-Model differences show the impact of assimilating LAI and SWI-001 on the simulated SSM.



2010	85972
2011	85439
2012	83612
2013	84304
2014	82588
2015	285998
2016	495292
2017	495331
2018	511044
2019	499594
min	82588
max	511044

Figure 41: Annual scores of the model (blue) and analysis (red) when compared to the rescaled SWI-001 over the Murray-Darling basin at 0.25° spatial resolution, with N ranging from 82,588 in 2014 to 511,044 in 2018. The yearly N values are indicated in the legend Table. Analysis-Model differences show the impact of assimilating LAI and SWI-001 on the simulated SSM.

Table 6: Annual score values of the model and analysis w.r.t. the rescaled SWI-001 over Southern Africa (top) from 2010 to 2019, the Murray-Darling basin (bottom) from 2010 to 2019. Model-analysis differences show the impact of assimilating LAI and SWI-001 on the simulated SSM.

Period	Version	Bias	Correlation	RMSD	SDD	Nb_pts
2010	Model	-0.001	0.903	0.026	0.026	149615
2010	Analysis	0.002	0.916	0.025	0.024	149615
2011	Model	0.006	0.893	0.032	0.032	140118
2011	Analysis	0.007	0.906	0.031	0.030	140118
2012	Model	0.006	0.909	0.028	0.028	142132
2012	Analysis	0.006	0.919	0.027	0.026	142132
2013	Model	0.000	0.907	0.026	0.026	146128
2013	Analysis	0.001	0.923	0.024	0.024	146128
2014	Model	0.003	0.898	0.028	0.028	145681
2014	Analysis	0.004	0.911	0.026	0.026	145681
2015	Model	0.003	0.925	0.024	0.024	203097
2015	Analysis	0.003	0.941	0.022	0.021	203097
2016	Model	-0.001	0.920	0.025	0.025	244532
2016	Analysis	0.001	0.936	0.022	0.022	244532
2017	Model	-0.009	0.912	0.027	0.025	247048
2017	Analysis	-0.005	0.933	0.022	0.022	247048
2018	Model	-0.003	0.907	0.027	0.027	241250
2018	Analysis	-0.001	0.935	0.023	0.023	241250
2019	Model	-0.011	0.906	0.029	0.026	260019
2019	Analysis	-0.006	0.940	0.022	0.021	260019

Period	Version	Bias	Correlation	RMSD	SDD	Nb_pts
2010	Model	-0.010	0.832	0.037	0.036	85972
2010	Analysis	-0.004	0.840	0.035	0.034	85972
2011	Model	-0.014	0.823	0.037	0.034	85439
2011	Analysis	-0.008	0.848	0.032	0.031	85439
2012	Model	-0.007	0.885	0.030	0.029	83612
2012	Analysis	-0.002	0.897	0.028	0.028	83612
2013	Model	0.003	0.895	0.027	0.027	84304
2013	Analysis	0.005	0.904	0.026	0.025	84304
2014	Model	0.007	0.876	0.030	0.030	82588
2014	Analysis	0.009	0.891	0.029	0.028	82588
2015	Model	0.004	0.890	0.028	0.027	285998
2015	Analysis	0.005	0.906	0.026	0.025	285998
2016	Model	0.000	0.896	0.030	0.030	495292
2016	Analysis	0.001	0.911	0.028	0.028	495292
2017	Model	0.000	0.878	0.026	0.026	495331
2017	Analysis	0.003	0.898	0.024	0.024	495331
2018	Model	0.008	0.842	0.030	0.029	511044
2018	Analysis	0.008	0.886	0.026	0.025	511044
2019	Model	0.013	0.847	0.033	0.030	499594
2019	Analysis	0.009	0.894	0.027	0.025	499594

Conclusion for SWI-001:

Contrary to LAI and FAPAR products:

- SSM SDD and RMSD scores in 2019 do not present significantly better values than for the 2010-2018 reference period of time over the Murray-Darling basin (Figure 39, Table 6),
- the analyzed SSM does not present a reinforcement of the drought signal with respect to the modelled SSM.

For example, over Southern Africa the analysis leads to larger SSM values from May to December in the area of Cape Town (Figure 26, Figure 27) where the analysis leads to smaller LAI values (Figure 4, Figure 5). The same conclusion can be drawn for the south-east of the Murray-Darling basin from January to June 2019 only (see Figure 6 for LAI and Figure 28 for SSM).

The impact of the seasonal SSM CDF-matching performed prior the assimilation is particularly striking for Southern Africa (Figure 36): while the lowest SSM rescaled observations, model and analysis simulations are observed in 2019 during the dry season, the smallest values of the raw SWI-001 time series are observed in 2015, across seasons. Without the complex seasonal CDF-matching, the SSM information would be misleading over Southern Africa. On the other hand, raw and rescaled observations are much more proportional over the Murray-Darling basin (Figure 37), and a simple constant CDF-matching would probably give similar results as the seasonal CDF-matching over this region.

8 RESULTS FOR LST

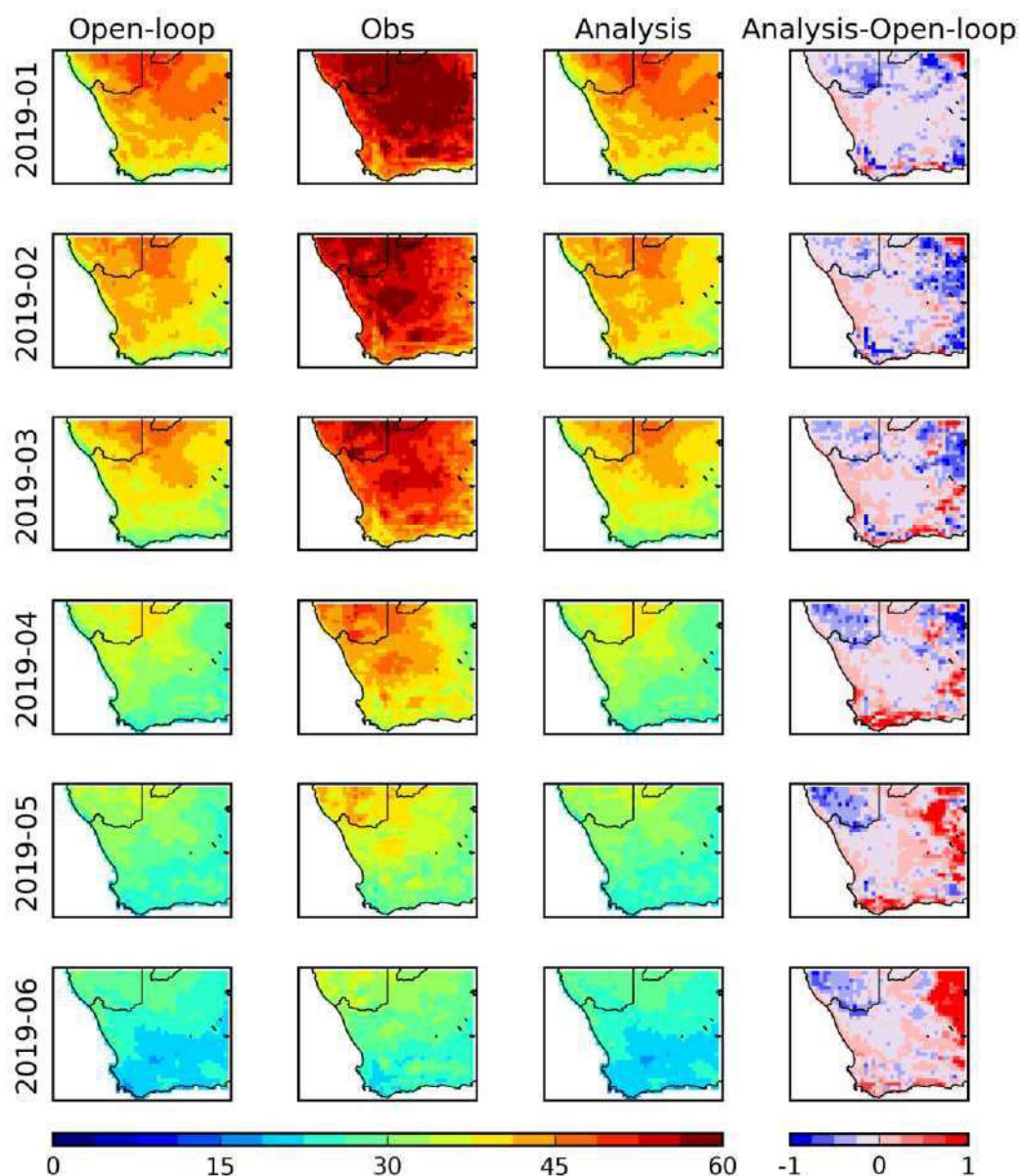


Figure 42: Monthly average values of LST at 1200 UTC over Southern Africa at 0.25° spatial resolution from January to June 2019. From left to right: model, satellite product, analysis, analysis-model difference. The latter shows the impact of assimilating LAI and SWI-001 on the simulated LST. The color scale range of LST values is 0 to 60 °C.

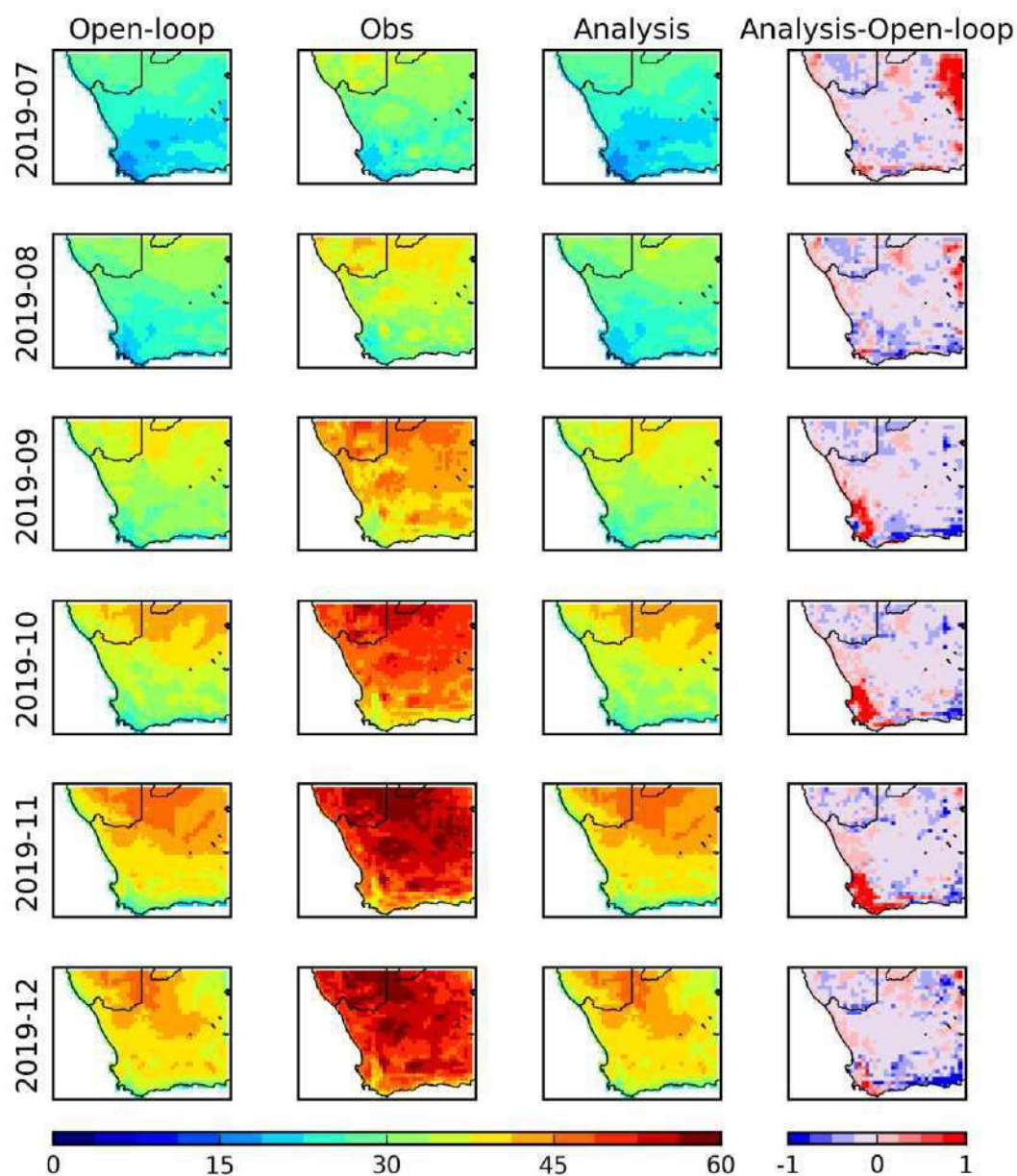


Figure 43: Monthly average values of LST at 1200 UTC over Southern Africa at 0.25° spatial resolution from July to December 2019. From left to right: model, satellite product, analysis, analysis-model difference. The latter shows the impact of assimilating LAI and SWI-001 on the simulated LST. The color scale range of LST values is 0 to 60 °C.

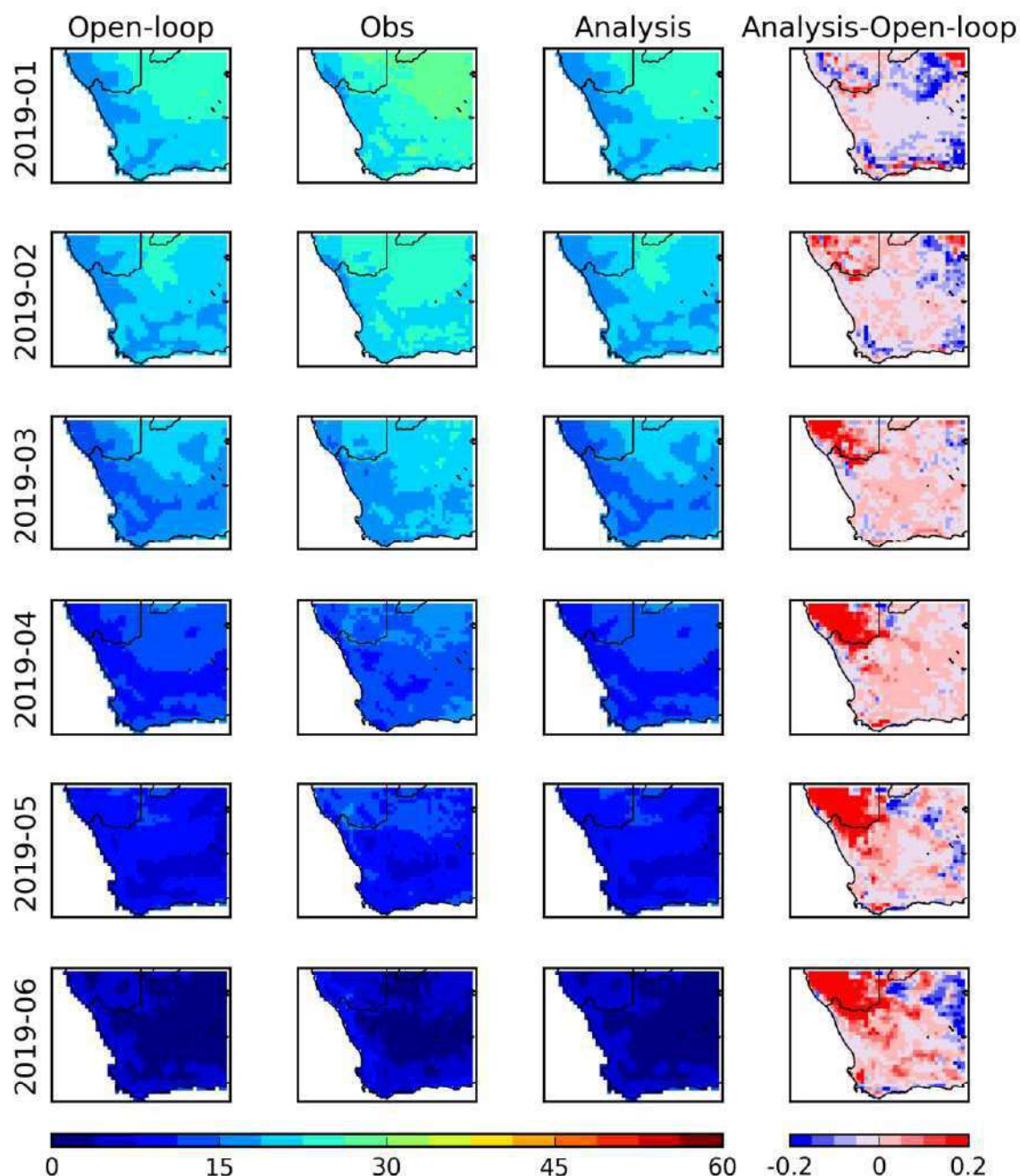


Figure 44: Monthly average values of LST at 0600 UTC over Southern Africa at 0.25° spatial resolution from January to June 2019. From left to right: model, satellite product, analysis, analysis-model difference. The latter shows the impact of assimilating LAI and SWI-001 on the simulated LST. The color scale range of LST values is 0 to 60 °C.

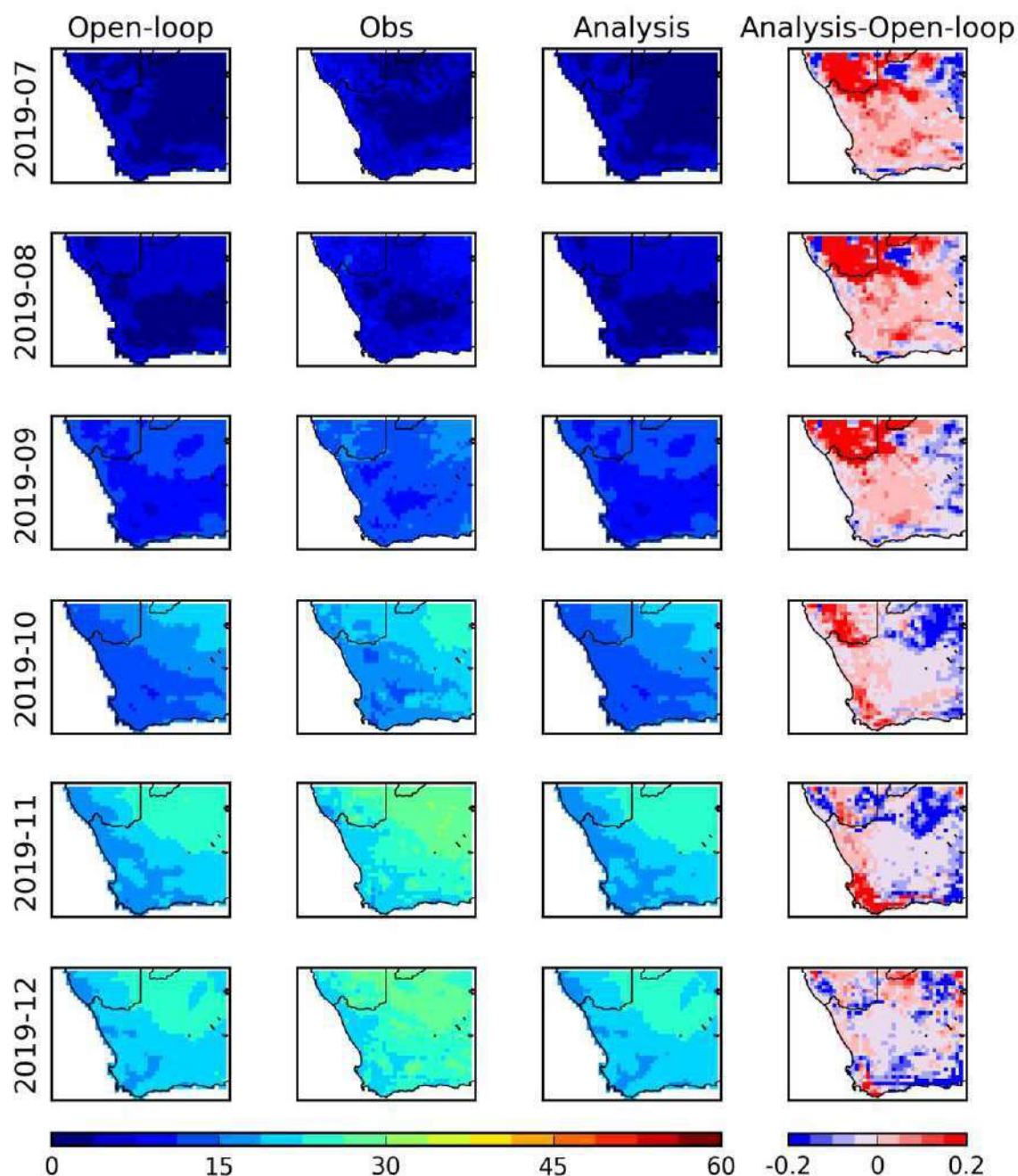


Figure 45: Monthly average values of LST at 0600 UTC over Southern Africa at 0.25° spatial resolution from July to December 2019. From left to right: model, satellite product, analysis, analysis-model difference. The latter shows the impact of assimilating LAI and SWI-001 on the simulated LST. The color scale range of LST values is 0 to 60 °C.

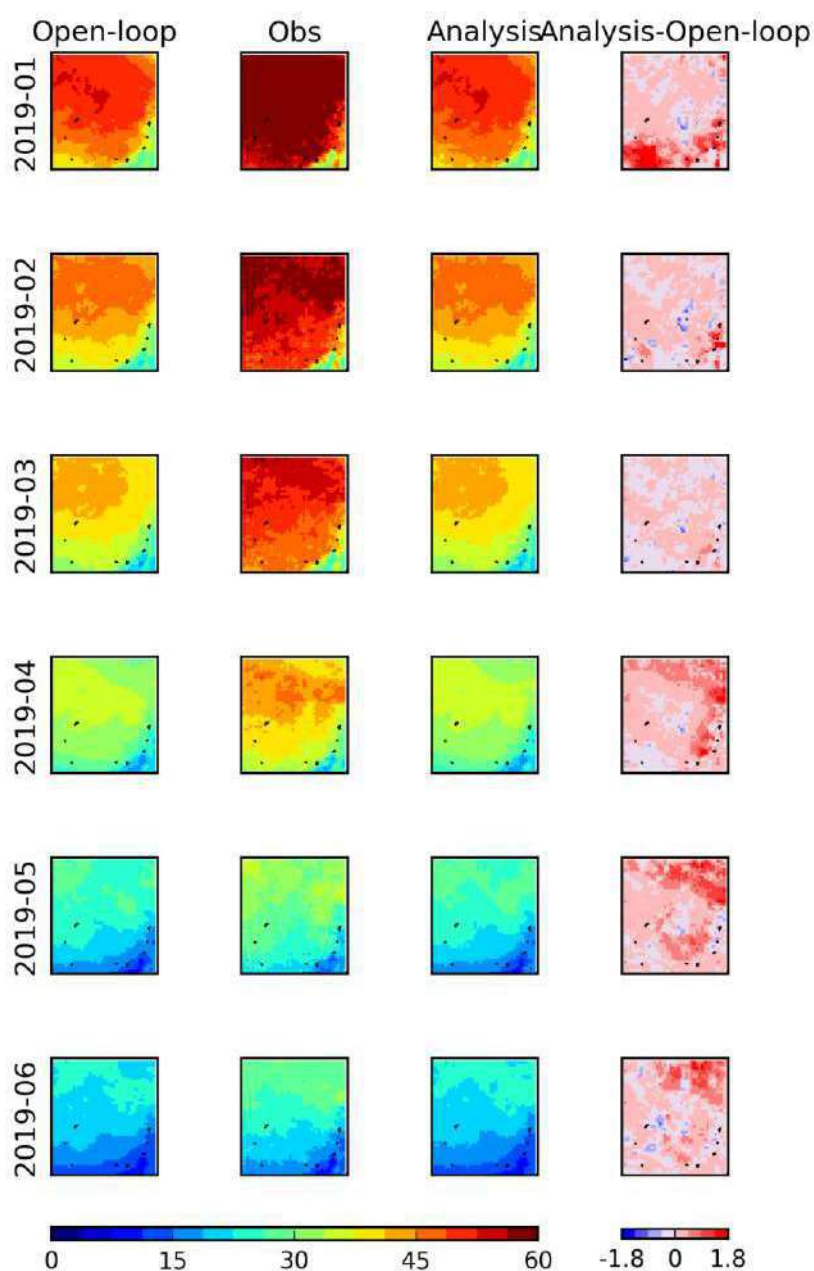


Figure 46: Monthly average values of LST at 0300 UTC (~noon) over the Murray-Darling basin at 0.25° spatial resolution from January to June 2019: model (left), satellite (middle) product, and analysis (right). Analysis-Model differences show the impact of assimilating LAI and SWI-001 on the simulated LST. The color scale range of LST values is 0 to 60 °C.

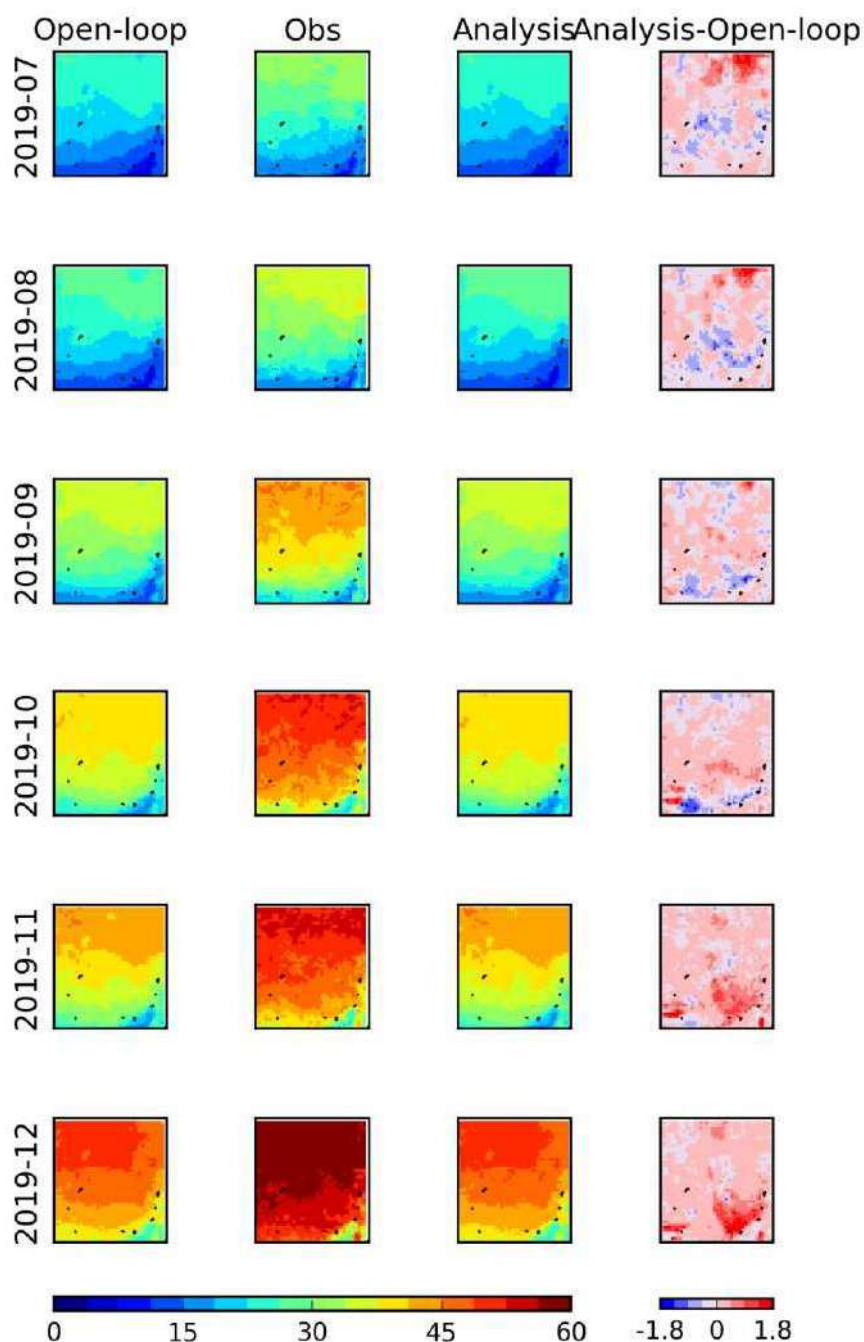


Figure 47: Monthly average values of LST at 0300 UTC (~noon) over the Murray-Darling basin at 0.25° spatial resolution from July to December 2019: model (left), satellite (middle) product, and analysis (right). Analysis-Model differences show the impact of assimilating LAI and SWI-001 on the simulated LST. The color scale range of LST values is 0 to 60 °C.

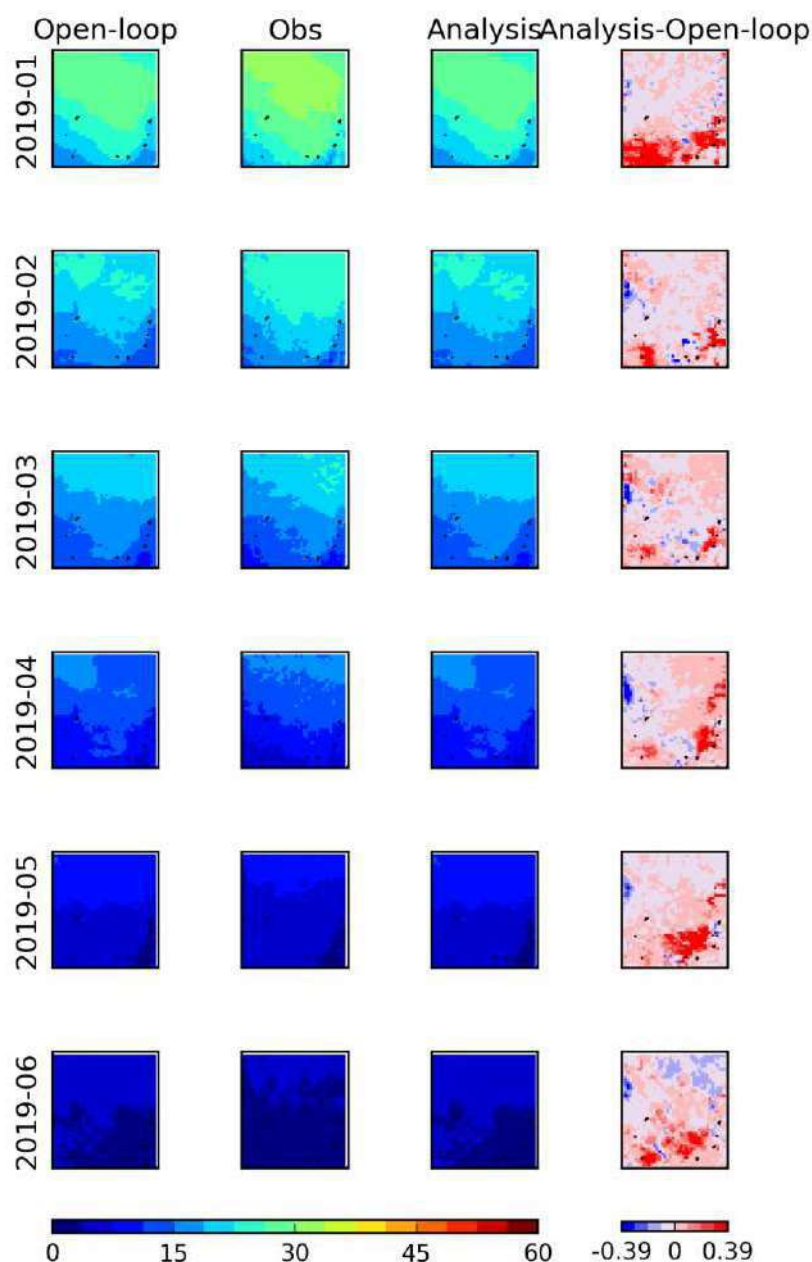


Figure 48: Monthly average values of LST at 2100 UTC (~dawn) over the Murray-Darling basin at 0.25° spatial resolution from January to June 2019: model (left), satellite (middle) product, and analysis (right). Analysis-Model differences show the impact of assimilating LAI and SWI-001 on the simulated LST. The color scale range of LST values is 0 to 60 °C.

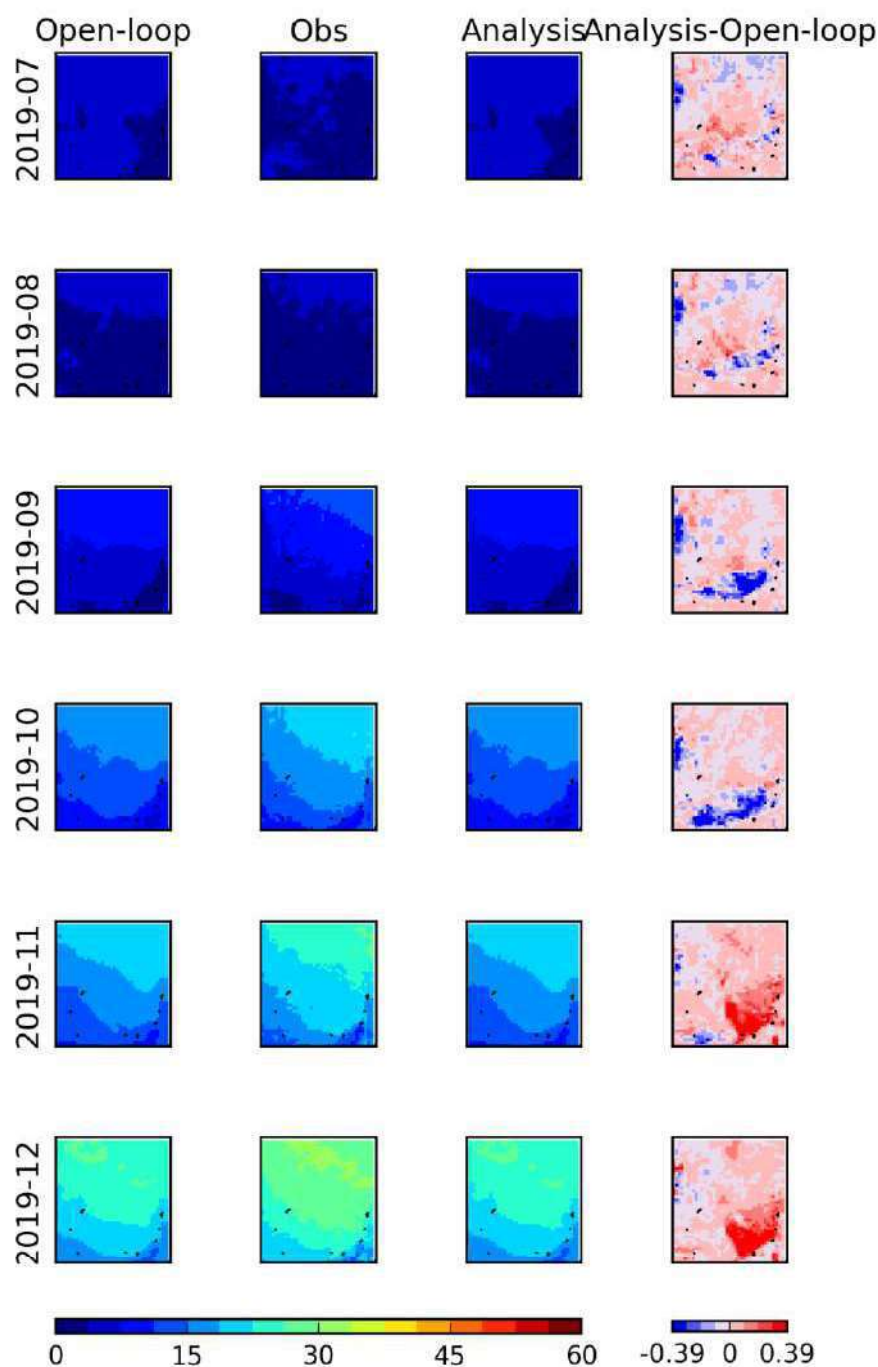


Figure 49: Monthly average values of LST at 2100 UTC (~dawn) over the Murray-Darling basin at 0.25° spatial resolution from July to December 2019: model (left), satellite (middle) product, and analysis (right). Analysis-Model differences show the impact of assimilating LAI and SWI-001 on the simulated LST. The color scale range of LST values is 0 to 60 °C.

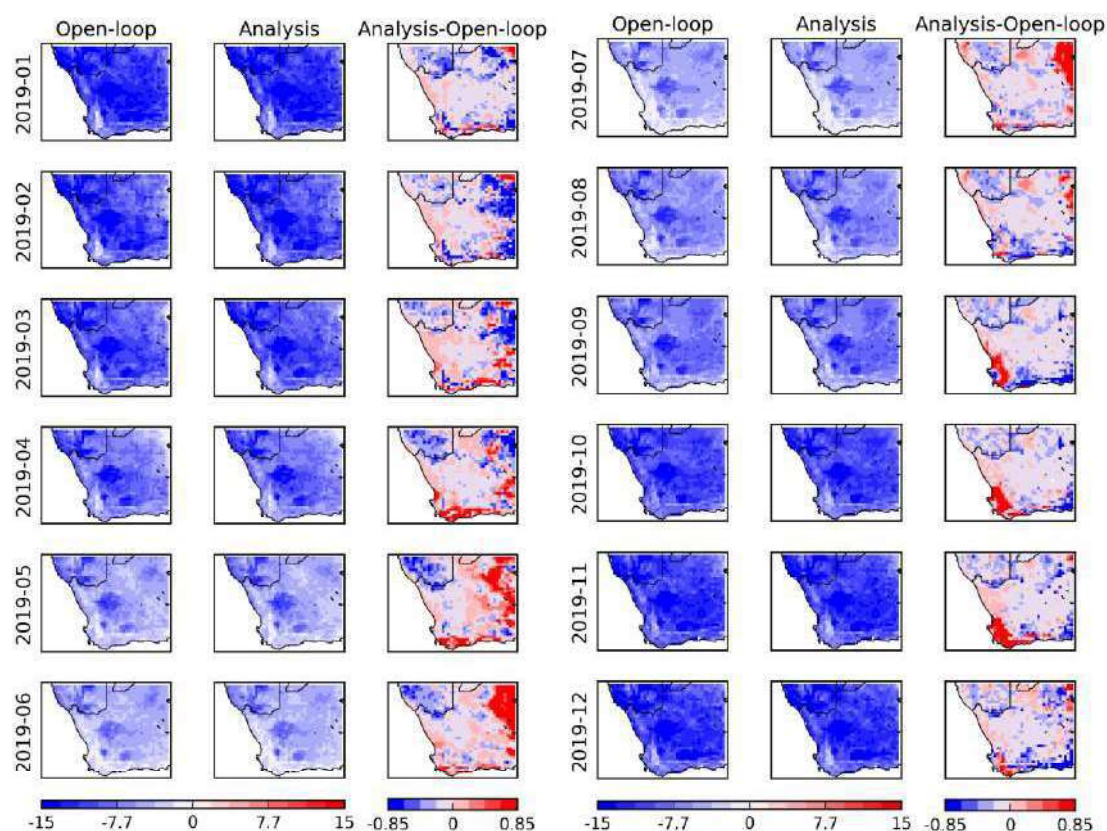


Figure 50: Monthly bias for LST at 1200 UTC over Southern Africa at 0.25° spatial resolution from January to December 2019. From left to right: model, analysis, analysis-model difference. The latter shows the impact of assimilating LAI and SWI-001 on the simulated LST. The color scale range of LST bias values is -15 to 15 °C.

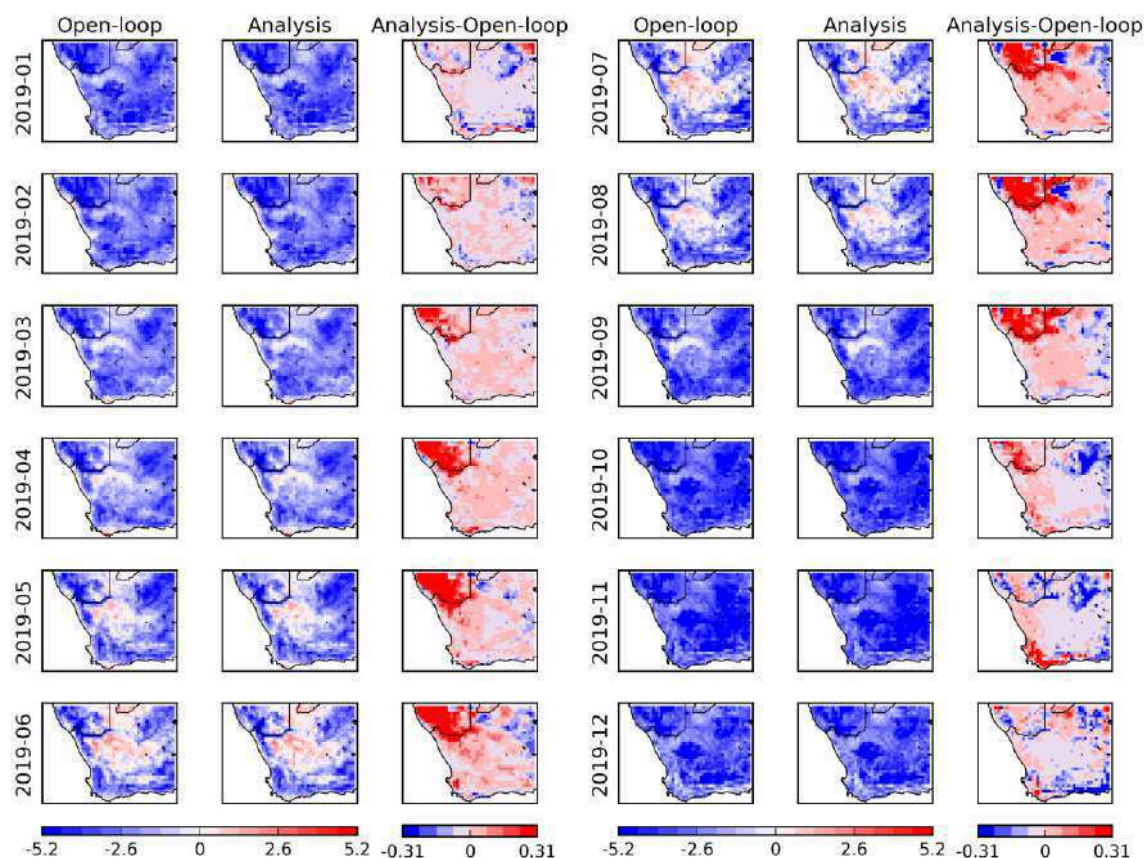


Figure 51: Monthly bias for LST at 0600 UTC over Southern Africa at 0.25° spatial resolution from January to December 2019. From left to right: model, analysis, analysis-model difference. The latter shows the impact of assimilating LAI and SWI-001 on the simulated LST. The color scale range of LST bias values is -5.2 to 5.2 °C.

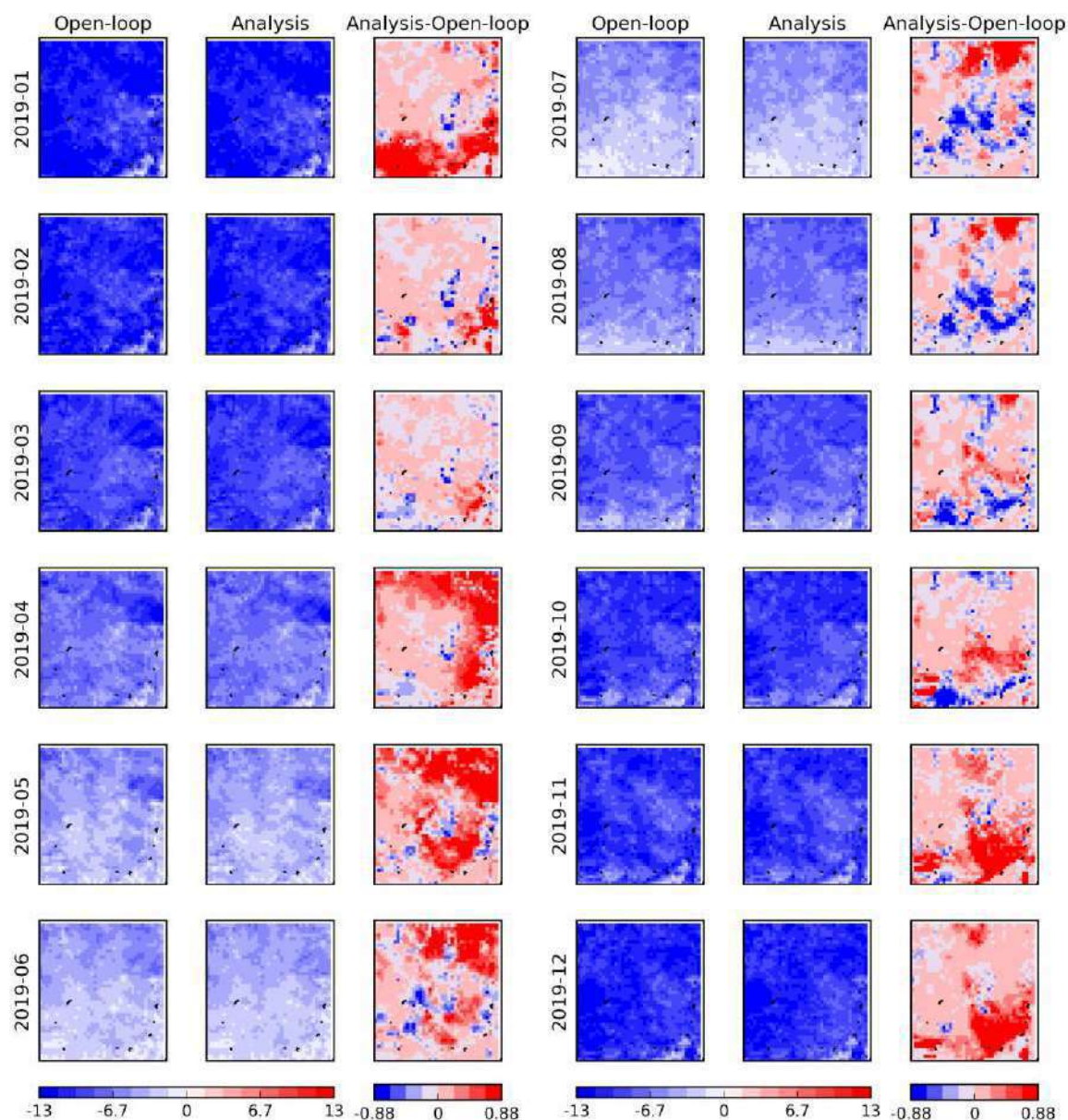


Figure 52: Monthly bias for LST at 0300 UTC (~noon) over the Murray-Darling basin at 0.25° spatial resolution from January to December 2019. From left to right: model, analysis, analysis-model difference. The latter shows the impact of assimilating LAI and SWI-001 on the simulated LST. The color scale range of LST bias values is -13 to 13 °C.

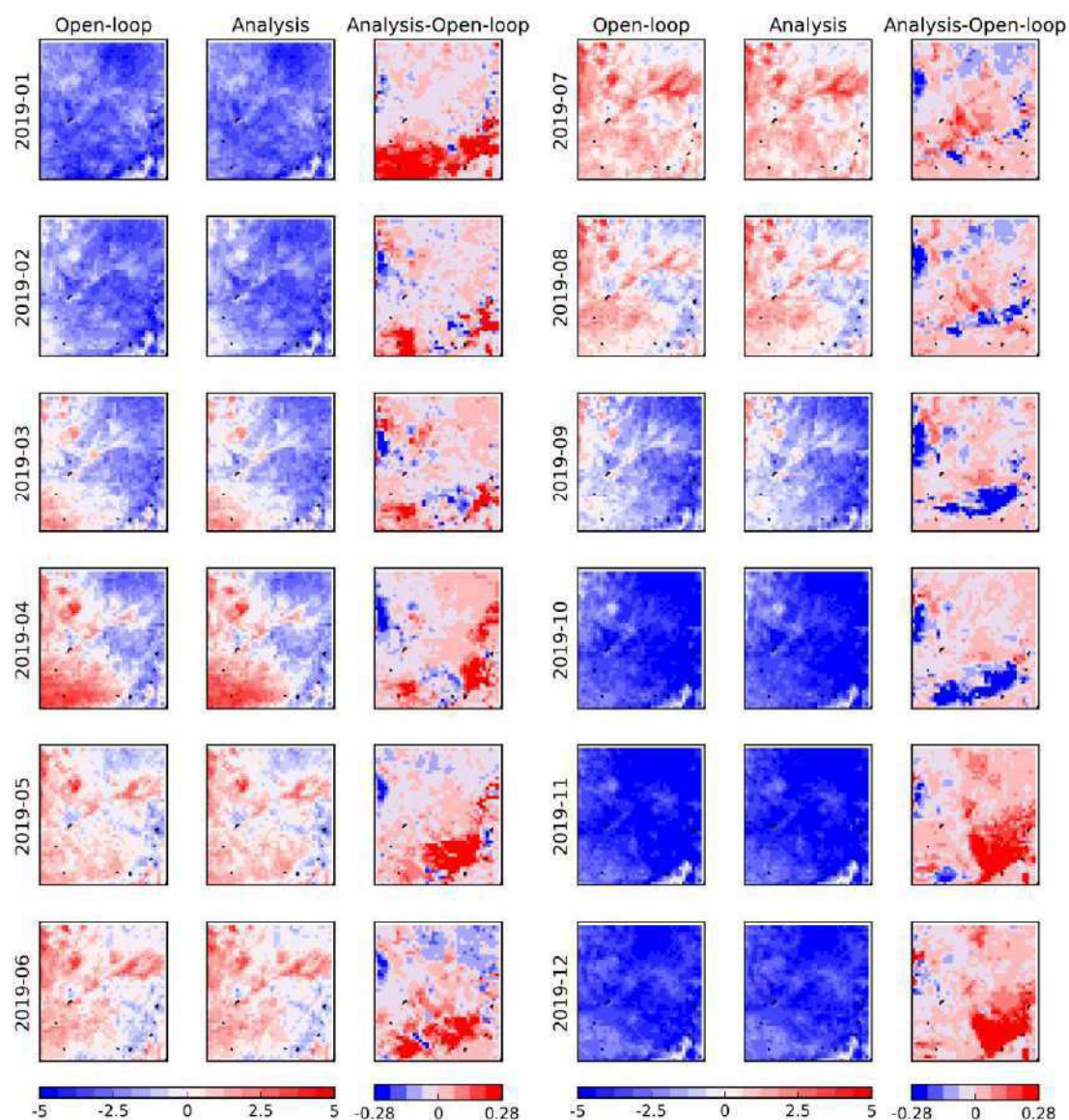


Figure 53: Monthly bias for LST at 2100 UTC (~dawn) over the Murray-Darling basin at 0.25° spatial resolution from January to December 2019. From left to right: model, analysis, analysis-model difference. The latter shows the impact of assimilating LAI and SWI-001 on the simulated LST. The color scale range of LST bias values is -5 to 5 °C.

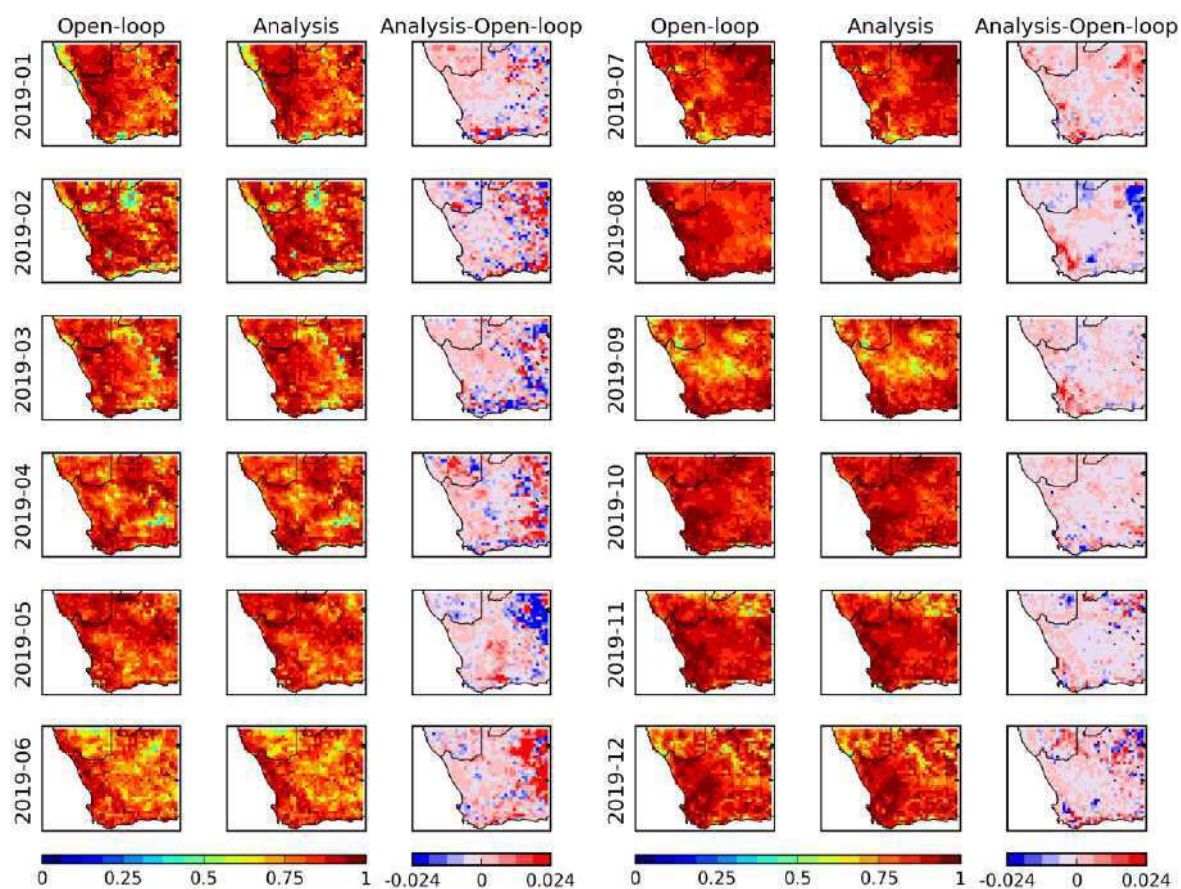


Figure 54: Monthly correlation for LST at 1200 UTC over Southern Africa at 0.25° spatial resolution from January to December 2019. From left to right: model, analysis, analysis-model difference. The latter shows the impact of assimilating LAI and SWI-001 on the simulated LST.

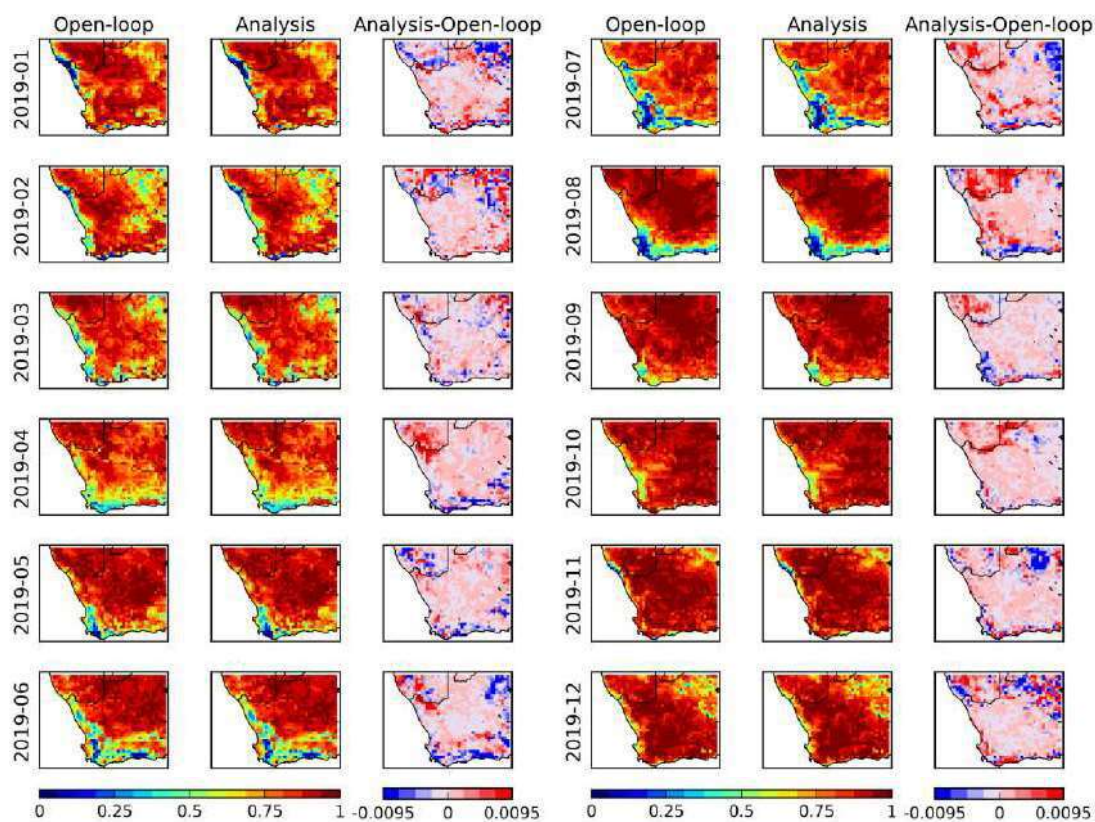


Figure 55: Monthly correlation for LST at 0600 UTC over Southern Africa at 0.25° spatial resolution from January to December 2019. From left to right: model, analysis, analysis-model difference. The latter shows the impact of assimilating LAI and SWI-001 on the simulated LST.

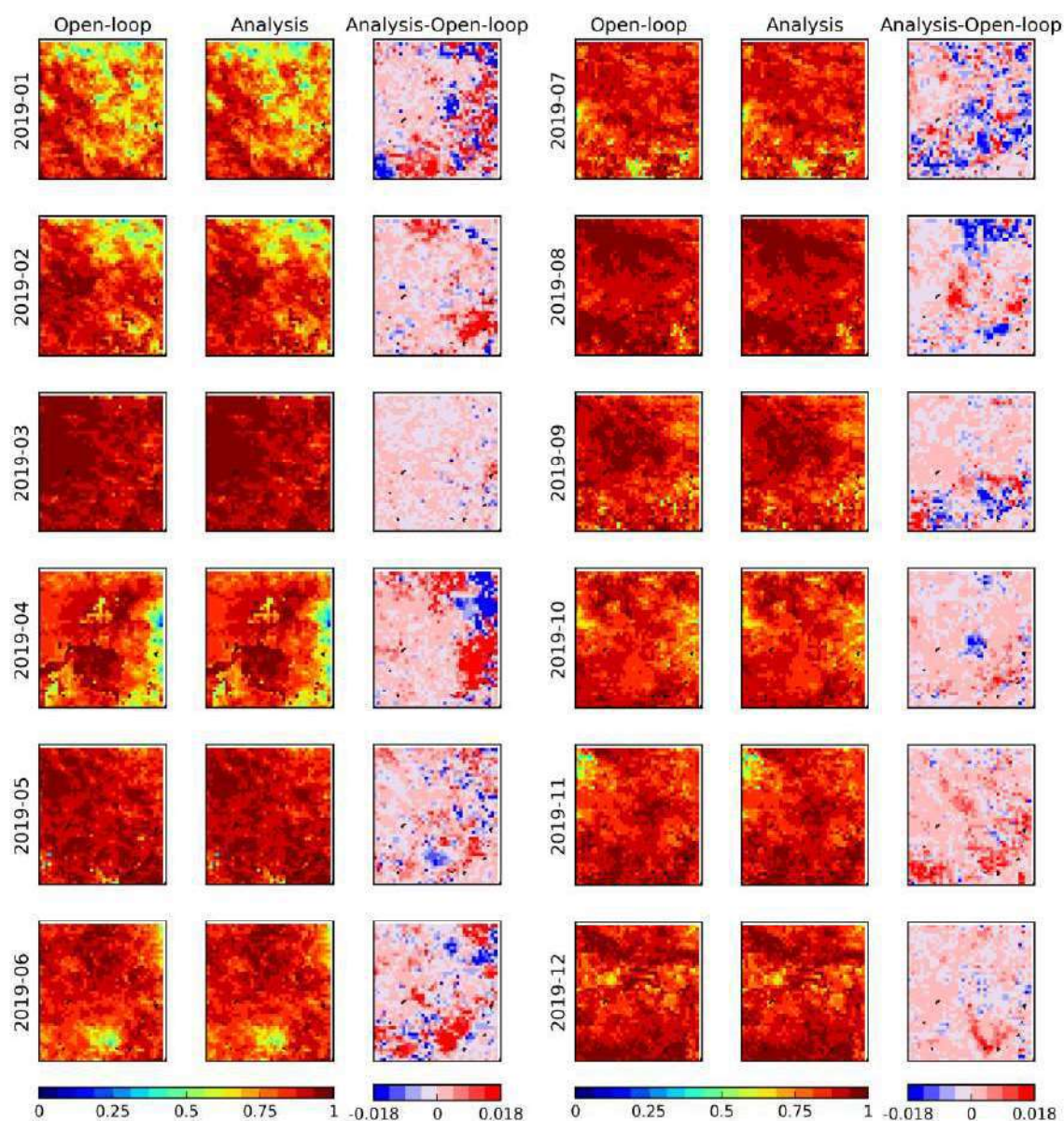


Figure 56: Monthly correlation for LST at 0300 UTC (~noon) over the Murray-Darling basin at 0.25° spatial resolution from January to December 2019. From left to right: model, analysis, analysis-model difference. The latter shows the impact of assimilating LAI and SWI-001 on the simulated LST.

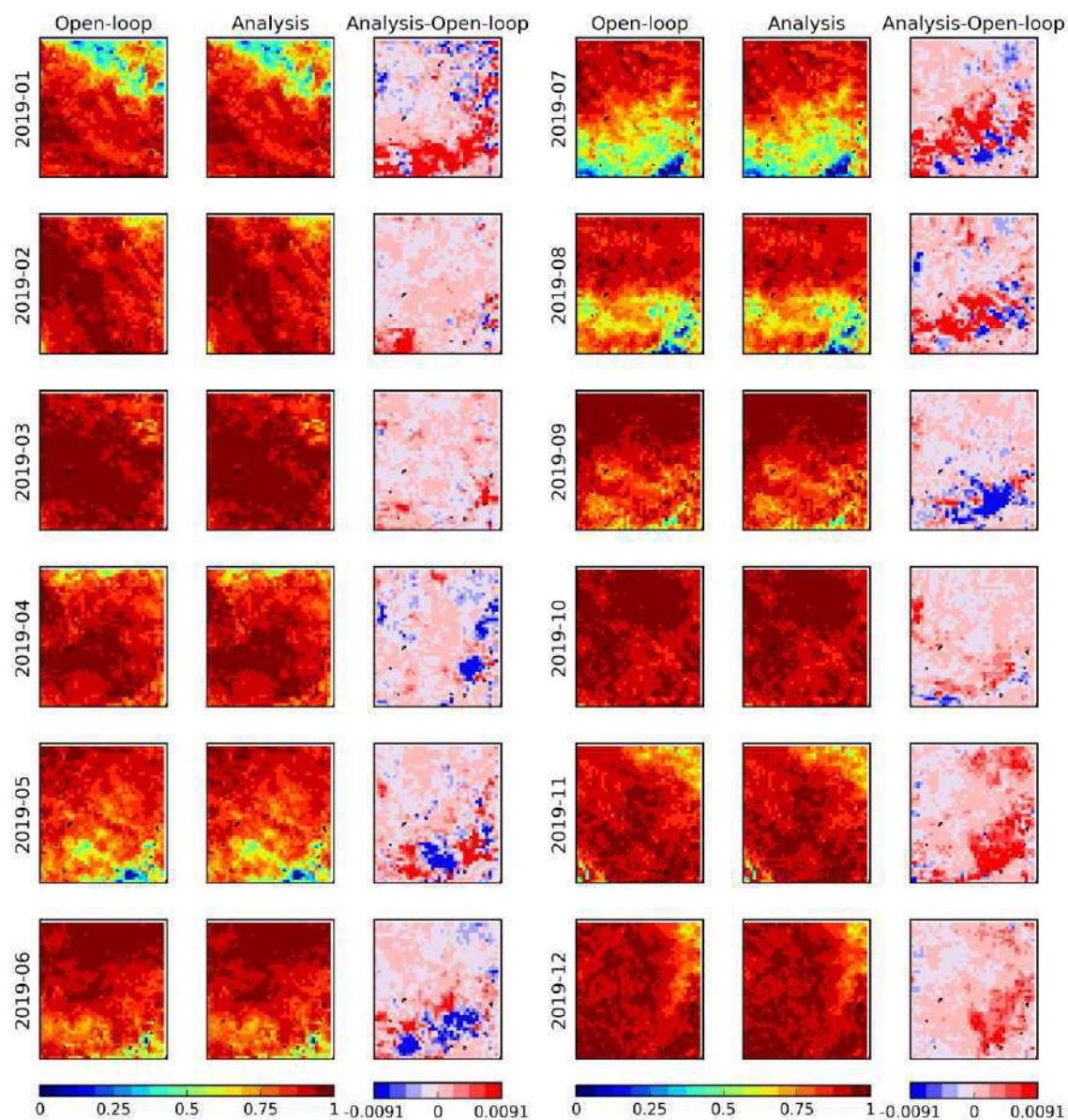


Figure 57: Monthly correlation for LST at 2100 UTC (~dawn) over the Murray-Darling basin at 0.25° spatial resolution from January to December 2019. From left to right: model, analysis, analysis-model difference. The latter shows the impact of assimilating LAI and SWI-001 on the simulated LST.

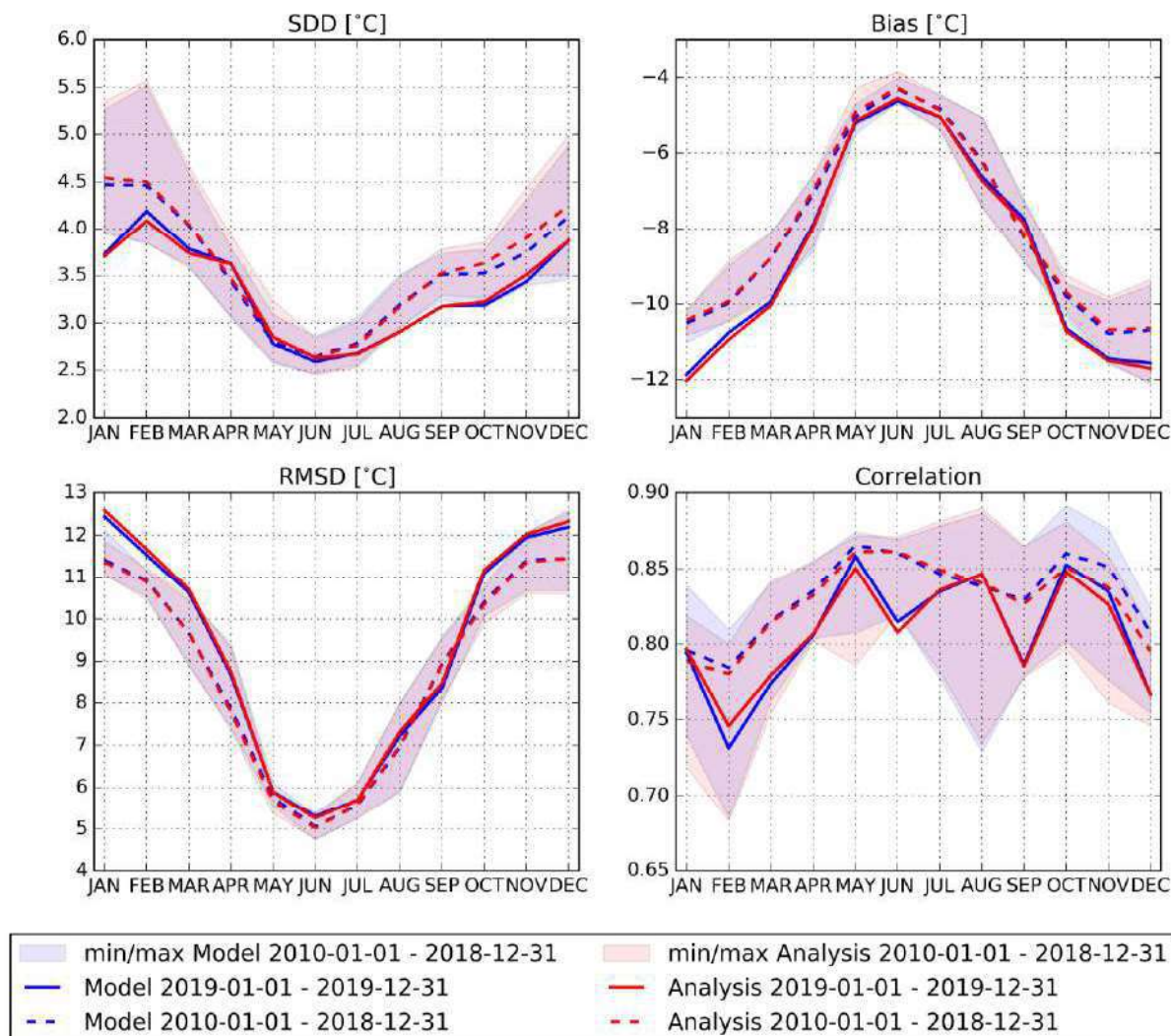


Figure 58: Monthly LST scores at 1200 UTC of the model (blue) and analysis (red) when compared to observations over Southern Africa at 0.25° spatial resolution: from 2010 to 2018 (dashed lines), with N ranging from 46,003 in December to 89,644 in March; and 2019 (solid lines), with N ranging from 3,518 in January to 15,793 in May. The monthly N values are indicated in the legend Table. Analysis-Model differences show the impact of assimilating LAI and SWI-001 on the simulated LST. Shaded areas are between minimum and maximum score values recorded from 2010 to 2018.

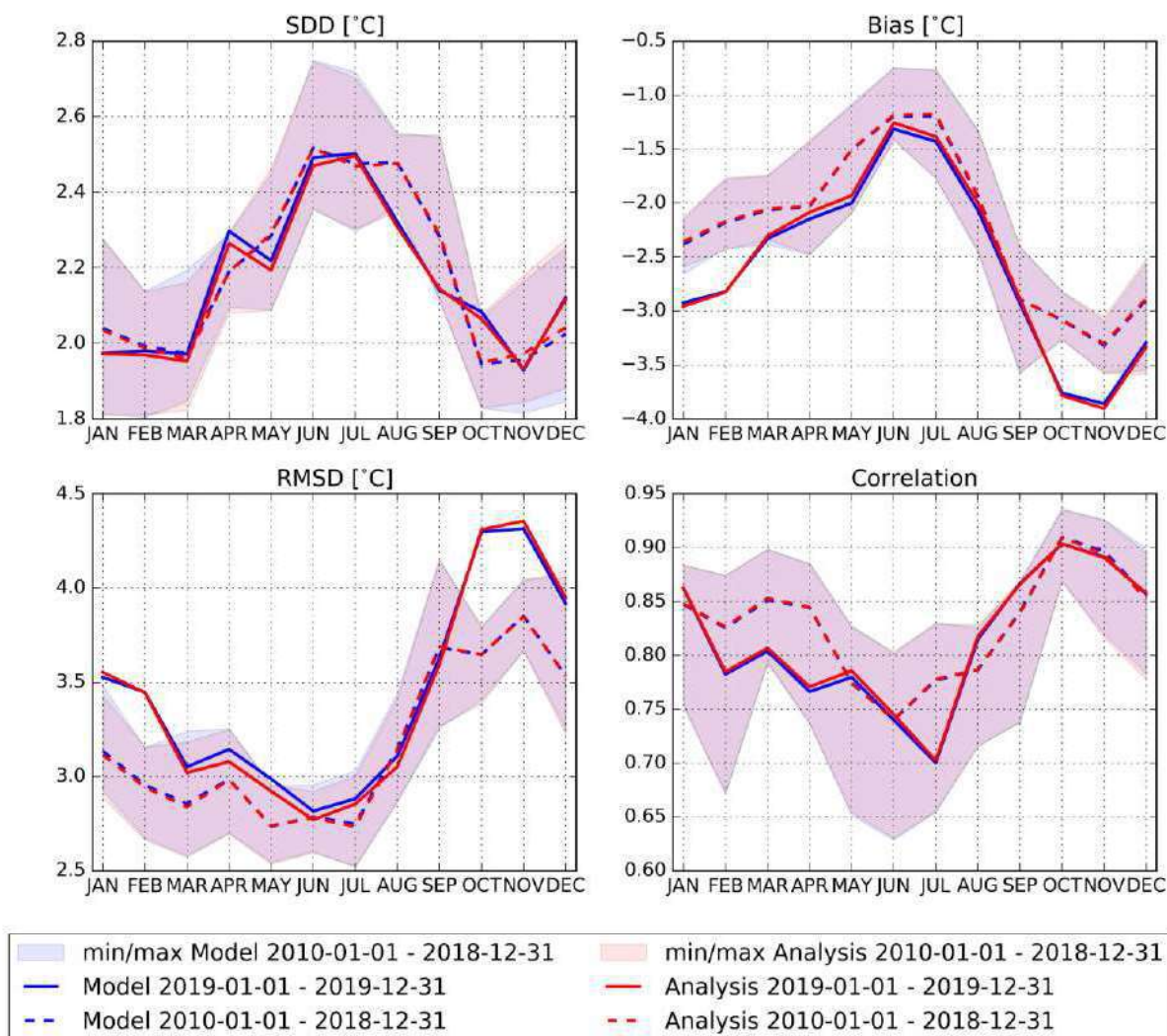


Figure 59: Monthly LST scores at 0600 UTC of the model (blue) and analysis (red) when compared to observations over Southern Africa at 0.25° spatial resolution: from 2010 to 2018 (dashed lines), with N ranging from 65,939 in November to 121,511 in March; and 2019 (solid lines), with N ranging from 4,617 in January to 23,143 in July. The monthly N values are indicated in the legend Table. Analysis-Model differences show the impact of assimilating LAI and SWI-001 on the simulated LST. Shaded areas are between minimum and maximum score values recorded from 2010 to 2018.

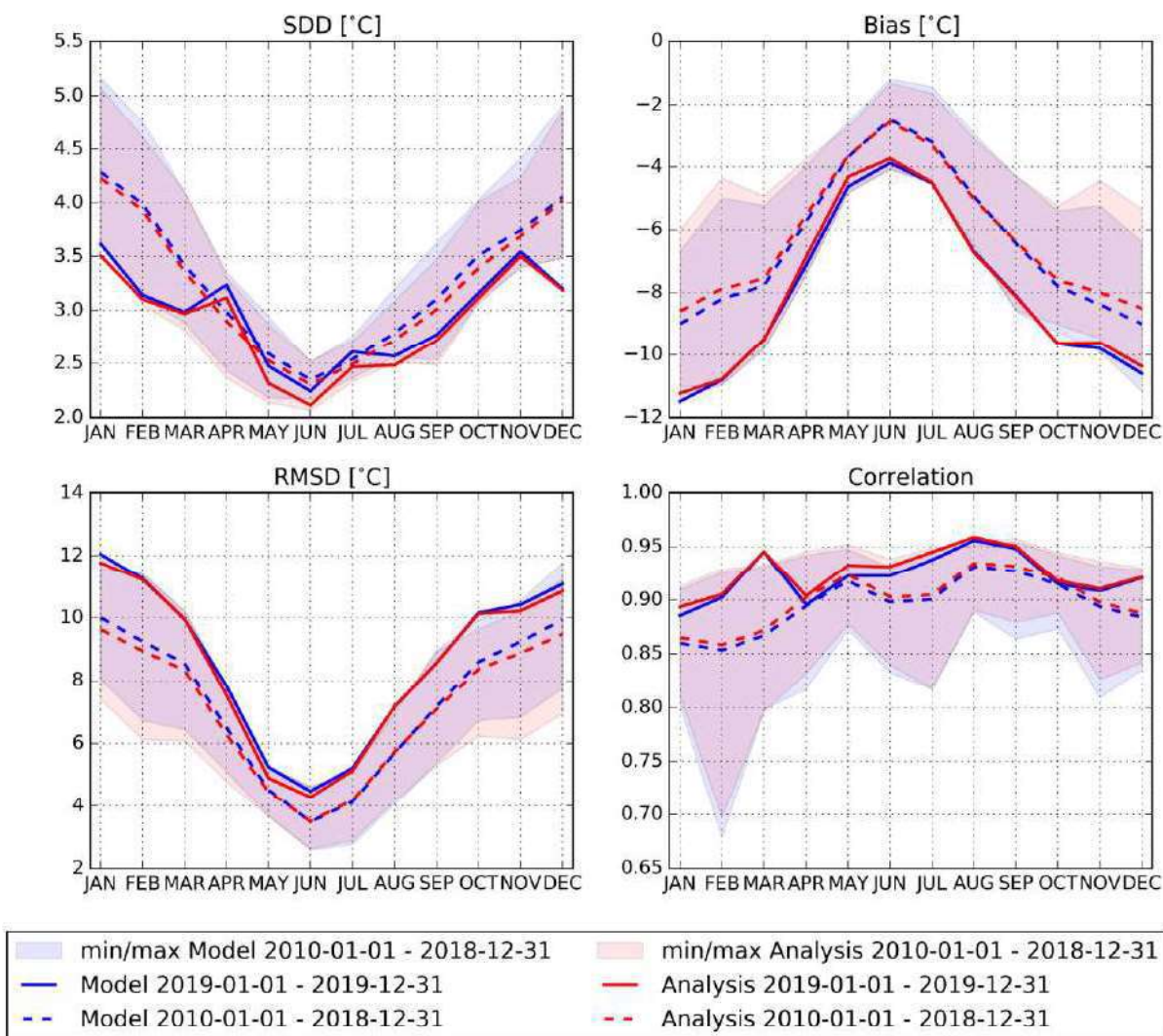


Figure 60: Monthly LST scores at 0300 UTC (~noon) of the model (blue) and analysis (red) when compared to observations over the Murray-Darling basin at 0.25° spatial resolution: from 2010 to 2018 (dashed lines), with N ranging from 244,461 in March to 312,367 in September; and 2019 (solid lines), with N ranging from 31,304 in December to 43,018 in August. The monthly N values are indicated in the legend Table. Analysis-Model differences show the impact of assimilating LAI and SWI-001 on the simulated LST. Shaded areas are between minimum and maximum score values recorded from 2010 to 2018.

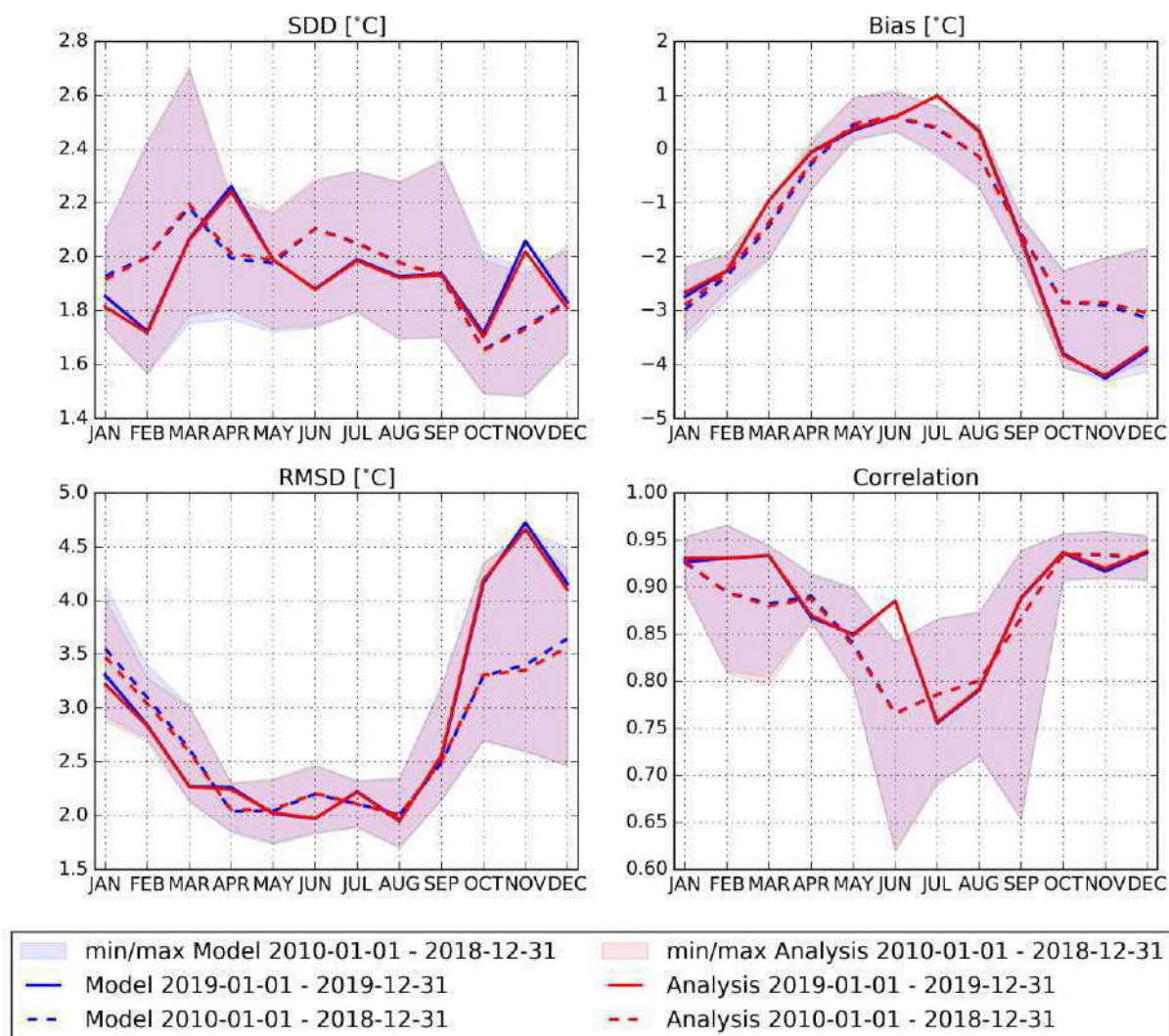


Figure 61: Monthly LST scores at 2100 UTC (~dawn) of the model (blue) and analysis (red) when compared to observations over the Murray-Darling basin at 0.25° spatial resolution: from 2010 to 2018 (dashed lines), with N ranging from 286,934 in February to 367,991 in August; and 2019 (solid lines), with N ranging from 34,959 in January to 48,635 in August. The monthly N values are indicated in the legend Table. Analysis-Model differences show the impact of assimilating LAI and SWI-001 on the simulated LST. Shaded areas are between minimum and maximum score values recorded from 2010 to 2018.

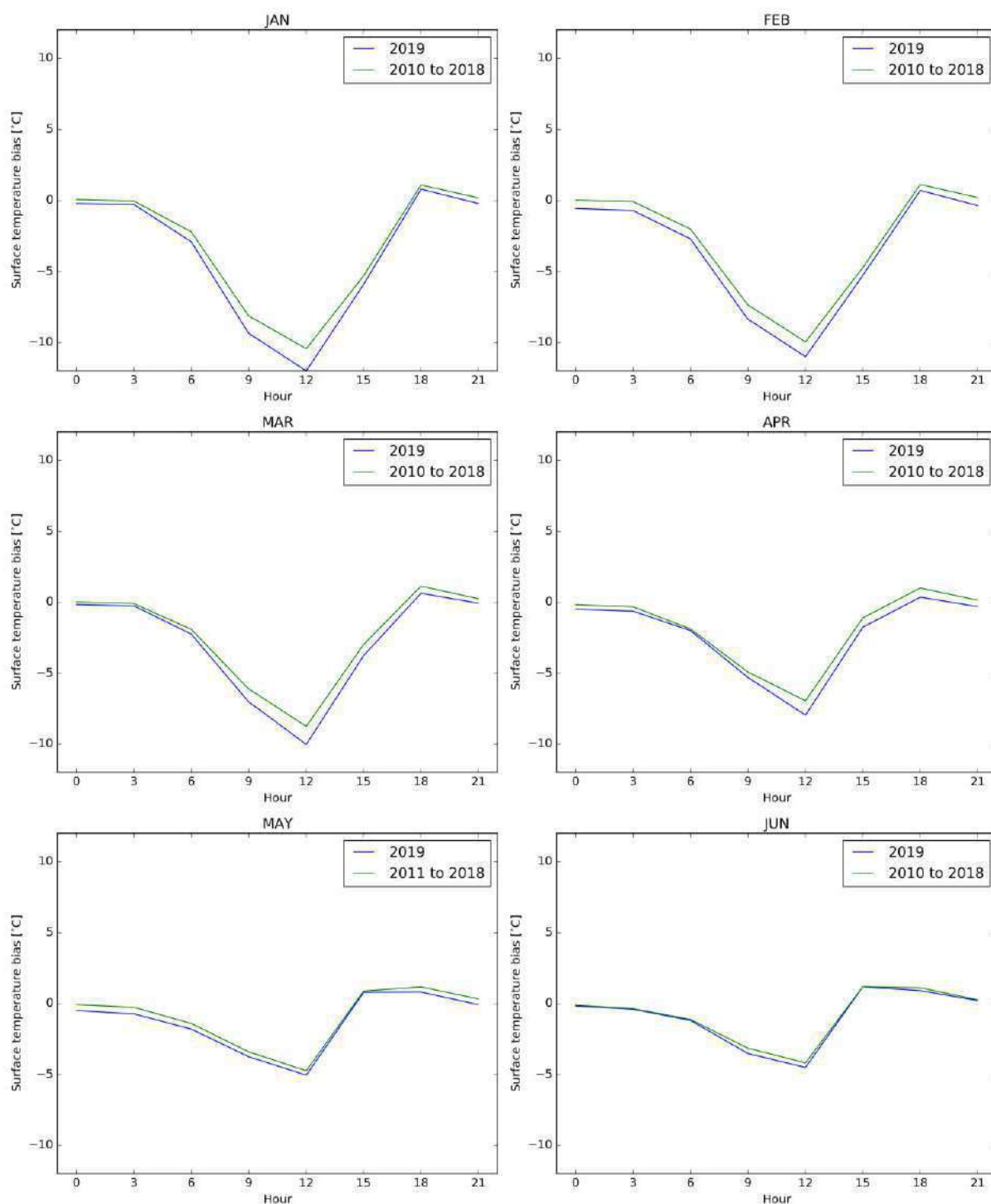


Figure 62: LST 3-hourly bias of the analysis over Southern Africa at 0.25° spatial resolution from January to June from 2010 to 2018 (green line) and for 2019 (blue line).

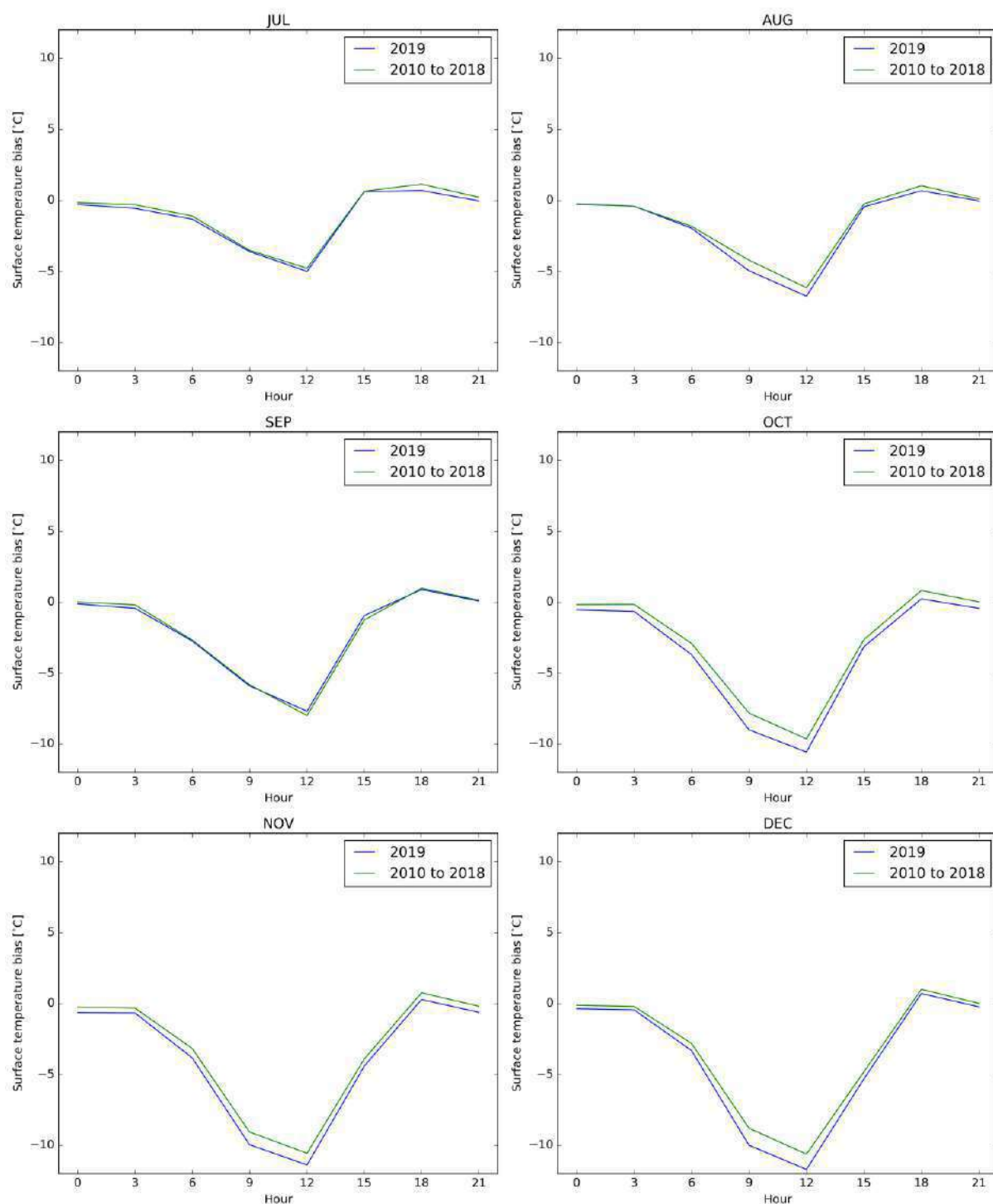


Figure 63: LST 3-hourly bias of the analysis over Southern Africa at 0.25° spatial resolution from July to December from 2010 to 2018 (green line) and for 2019 (blue line).

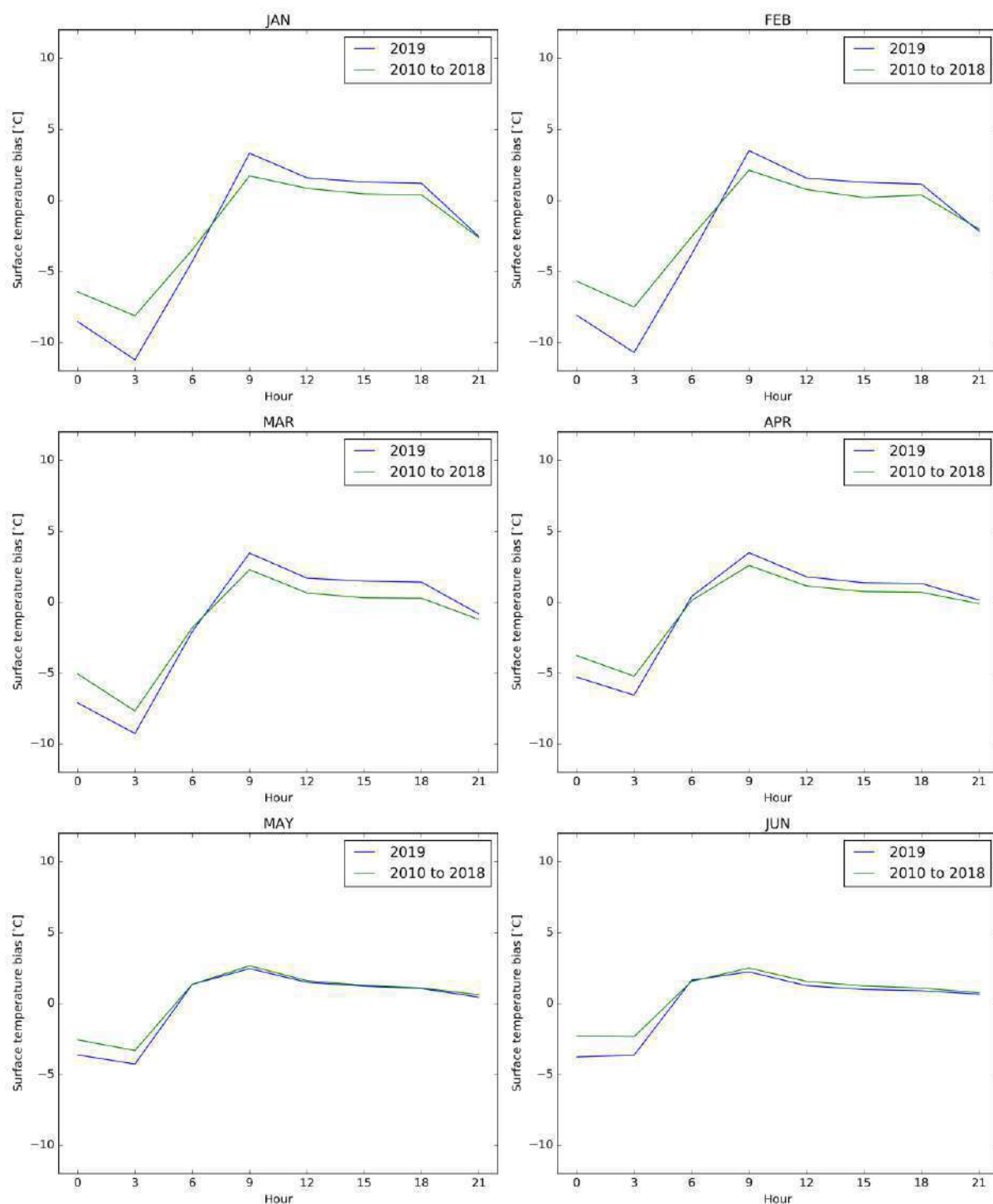


Figure 64: LST 3-hourly bias of the analysis over the Murray-Darling basin at 0.25° spatial resolution from January to June from 2010 to 2018 (green line) and for 2019 (blue line). [Note that 0300 UTC is close to noon at these longitudes.]

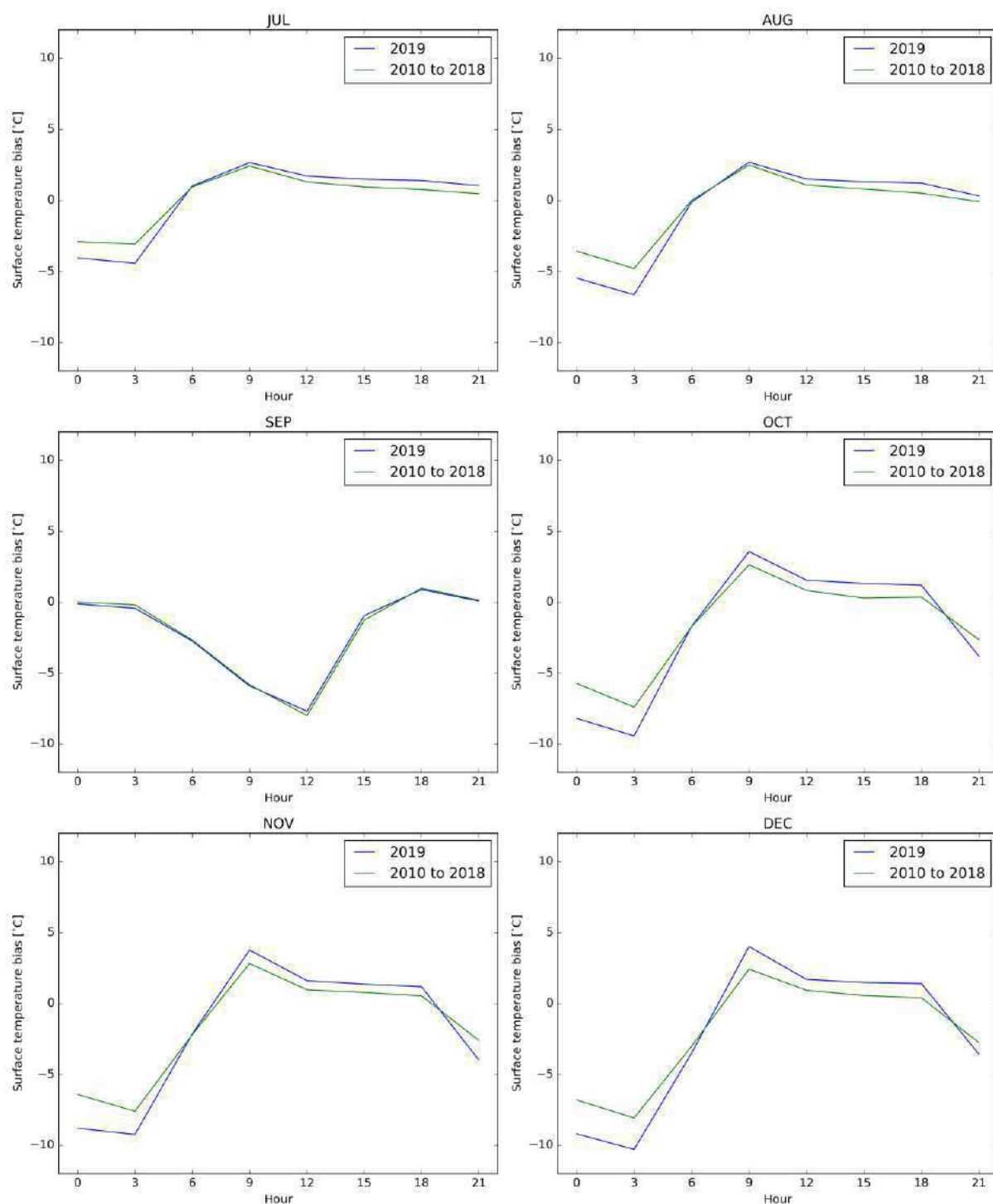


Figure 65: LST 3-hourly bias of the analysis over the Murray-Darling basin at 0.25° spatial resolution from July to December from 2010 to 2018 (green line) and for 2019 (blue line). [Note that 0300 UTC is close to noon at these longitudes.]

Table 7: LST annual scores of the model and analysis w.r.t. the LST observations at 1200 UTC (top) and 0600 UTC (bottom) over Southern Africa. Analysis-Model differences show the impact of assimilating LAI and SWI-001 on the simulated LST. The relatively unbiased average LST at 0600 UTC hides marked spatial and seasonal patterns (Figure 51 and Figure 59).

Period	Version	Bias	Correlation	RMSD	SDD	Nb_pts
2010	Model	-7.970	0.928	9.155	4.504	250605
2010	Analysis	-7.925	0.927	9.113	4.499	250605
2011	Model	-7.709	0.931	8.976	4.597	287344
2011	Analysis	-7.543	0.929	8.885	4.696	287344
2012	Model	-7.732	0.941	8.917	4.440	273181
2012	Analysis	-7.674	0.940	8.877	4.463	273181
2013	Model	-7.951	0.945	8.964	4.141	299945
2013	Analysis	-7.934	0.943	8.963	4.170	299945
2014	Model	-7.660	0.942	8.716	4.159	286564
2014	Analysis	-7.587	0.941	8.663	4.182	286564
2015	Model	-7.778	0.945	8.861	4.245	279790
2015	Analysis	-7.725	0.944	8.823	4.264	279790
2016	Model	-8.019	0.944	9.037	4.165	291123
2016	Analysis	-7.962	0.943	9.001	4.199	291123
2017	Model	-7.545	0.926	8.622	4.173	309747
2017	Analysis	-7.616	0.928	8.673	4.149	309747
2018	Model	-8.414	0.948	9.372	4.127	300796
2018	Analysis	-8.391	0.947	9.372	4.175	300796
2019	Model	-8.371	0.937	9.390	4.253	320940
2019	Analysis	-8.442	0.937	9.470	4.291	320940

Period	Version	Bias	Correlation	RMSD	SDD	Nb_pts
2010	Model	-2.225	0.965	3.266	2.391	264893
2010	Analysis	-2.199	0.965	3.247	2.389	264893
2011	Model	-2.133	0.963	3.180	2.359	317291
2011	Analysis	-2.136	0.962	3.190	2.369	317291
2012	Model	-2.003	0.966	3.148	2.429	304358
2012	Analysis	-1.999	0.966	3.148	2.432	304358
2013	Model	-2.295	0.967	3.243	2.292	336839
2013	Analysis	-2.278	0.967	3.231	2.291	336839
2014	Model	-2.206	0.966	3.159	2.262	329001
2014	Analysis	-2.199	0.966	3.157	2.265	329001
2015	Model	-2.063	0.968	3.047	2.243	316183
2015	Analysis	-2.060	0.968	3.045	2.241	316183
2016	Model	-2.215	0.967	3.150	2.239	326963
2016	Analysis	-2.208	0.968	3.143	2.237	326963
2017	Model	-2.172	0.965	3.127	2.250	342561
2017	Analysis	-2.138	0.965	3.100	2.245	342561
2018	Model	-2.438	0.968	3.354	2.303	335088
2018	Analysis	-2.448	0.968	3.363	2.306	335088
2019	Model	-2.524	0.964	3.438	2.335	346845
2019	Analysis	-2.503	0.964	3.423	2.336	346845

Table 8: LST annual scores of the model and analysis w.r.t. the LST observations at 0300 UTC (~noon) (top) and at 2100 UTC (~dawn) (bottom) over the Murray-Darling basin. Analysis-Model differences show the impact of assimilating LAI and SWI-001 on the simulated LST. The relatively unbiased average LST at 0600 UTC hides marked spatial and seasonal patterns (Figure 53 and Figure 61).

Period	Version	Bias	Correlation	RMSD	SDD	Nb_pts
2010	Model	-4.688	0.945	6.338	4.265	325542
2010	Analysis	-4.249	0.951	5.806	3.956	325542
2011	Model	-4.670	0.939	6.033	3.820	319690
2011	Analysis	-4.542	0.944	5.813	3.628	319690
2012	Model	-5.238	0.958	6.393	3.666	387556
2012	Analysis	-5.118	0.960	6.273	3.628	387556
2013	Model	-6.252	0.965	7.421	3.997	367295
2013	Analysis	-6.178	0.966	7.330	3.946	367295
2014	Model	-7.111	0.963	8.268	4.219	389410
2014	Analysis	-6.971	0.964	8.118	4.160	389410
2015	Model	-7.249	0.965	8.550	4.533	373684
2015	Analysis	-7.003	0.967	8.255	4.371	373684
2016	Model	-7.327	0.970	8.497	4.303	357970
2016	Analysis	-7.082	0.973	8.171	4.075	357970
2017	Model	-7.477	0.969	8.472	3.983	429899
2017	Analysis	-7.387	0.971	8.319	3.828	429899
2018	Model	-7.978	0.972	8.875	3.889	445760
2018	Analysis	-7.900	0.974	8.752	3.767	445760
2019	Model	-7.984	0.974	8.885	3.899	449132
2019	Analysis	-7.876	0.975	8.765	3.846	449132

Period	Version	Bias	Correlation	RMSD	SDD	Nb_pts
2010	Model	-1.197	0.958	2.737	2.462	414350
2010	Analysis	-1.136	0.958	2.710	2.461	414350
2011	Model	-1.016	0.964	2.644	2.441	418557
2011	Analysis	-0.982	0.964	2.621	2.430	418557
2012	Model	-1.048	0.970	2.448	2.212	456084
2012	Analysis	-1.039	0.970	2.452	2.221	456084
2013	Model	-1.234	0.970	2.546	2.227	460390
2013	Analysis	-1.210	0.970	2.539	2.232	460390
2014	Model	-1.368	0.971	2.796	2.438	451034
2014	Analysis	-1.351	0.971	2.785	2.436	451034
2015	Model	-1.240	0.970	2.790	2.499	457507
2015	Analysis	-1.194	0.971	2.752	2.479	457507
2016	Model	-1.746	0.953	3.188	2.667	384690
2016	Analysis	-1.700	0.953	3.153	2.655	384690
2017	Model	-1.434	0.975	2.827	2.436	475430
2017	Analysis	-1.390	0.976	2.783	2.411	475430
2018	Model	-1.287	0.972	2.974	2.681	485922
2018	Analysis	-1.259	0.973	2.932	2.649	485922
2019	Model	-1.350	0.970	2.993	2.671	498756
2019	Analysis	-1.340	0.970	2.974	2.655	498756

Conclusion for LST:

The simulated LST is generally smaller than the observed LST at daytime, for both Southern Africa and the Murray-Darling basin. At nighttime, the simulated LST tends to be slightly overestimated over the Murray-Darling basin (Figure 61, Figure 64, Figure 65).

The cold bias observed at noon is particularly large at summertime (from October to March) over both Southern Africa (down to -12°C in 2019) as shown in Figure 58, and over the Murray-Darling basin (down to -11°C in 2019) as shown in Figure 60.

These biases at noon are particularly noticeable in 2019 (Table 7, Table 8). Over the Murray-Darling basin, the mean yearly bias is about -8°C in 2019, against -4°C in 2010. Since 2010 is a very wet year compared to 2019 (see RZSM values in Figure 9), this result shows that LST biases are more pronounced in dry conditions over this area.

When the assimilation significantly reduces the simulated LAI (see Chapter 4), the LST noon bias is slightly reduced in the analysis. Reducing LAI tends to reduce plant transpiration cooling and to increase the simulated LST. Since the model is too cold at noon, the LST bias is reduced. This can be observed by comparing maps of differences between analysis and open-loop simulations for LAI and LST at noon over both Southern Africa (Figure 4 and Figure 42, Figure 5 and Figure 43) and the Murray-Darling basin (Figure 6 and Figure 46, Figure 7 and Figure 47): areas in red in Figures 4, 5, 6, 7 correspond to areas in blue in Figures 42, 43, 46, 47, respectively. Over the same areas, it can be observed that the assimilation tends to improve the temporal correlation of the simulated and observed LST as shown in Figure 54 and Figure 56. This shows the consistency of the observed LST with the observed LAI.

At dawn, the LST cold bias is smaller than at noon over Southern Africa (Figure 59) and is more marked in 2019 (Table 7). Over the Murray-Darling basin, the cold LST bias at dawn is only observed at summertime (Figure 61).

Possible causes of the spatial, diurnal and seasonal patterns of the LST bias are:

- hot-spot phenomenon (more sunlit than shaded elements are seen by the satellite) as described in Ermida et al. 2018,
- remaining biases in incoming solar (Urraca et al., 2018) and infrared radiation and in air temperature of ERA5.

9 LDAS STATISTICS

9.1 INCREMENTS AND IMPACTS OF THE ASSIMILATION ON WATER AND CARBON FLUXES

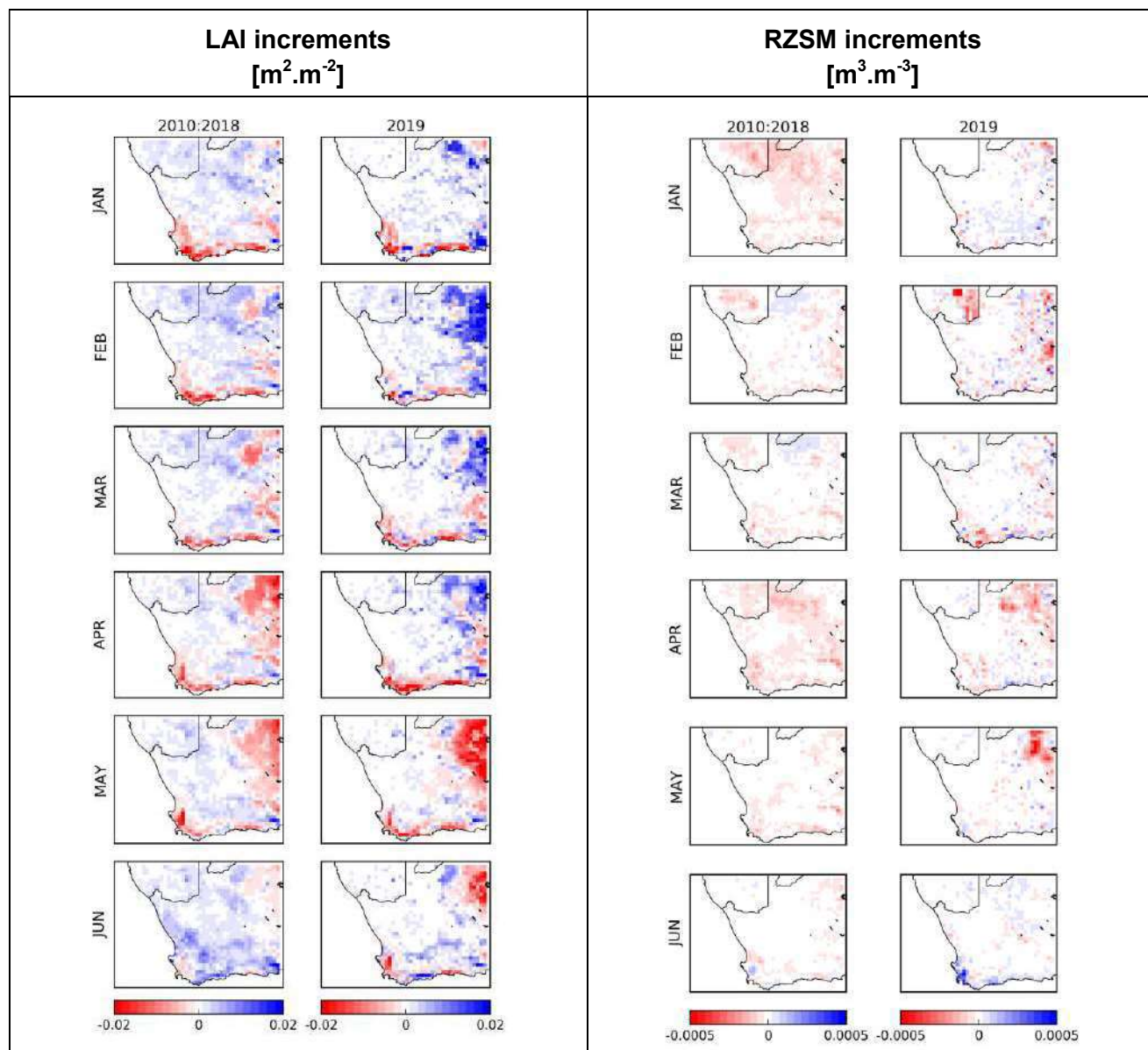


Figure 66: Monthly maps over Southern Africa from January to June of LAI (1st column), root-zone soil moisture (2nd column) increments: averages over 2010–2018 (left), and for 2019 (right).

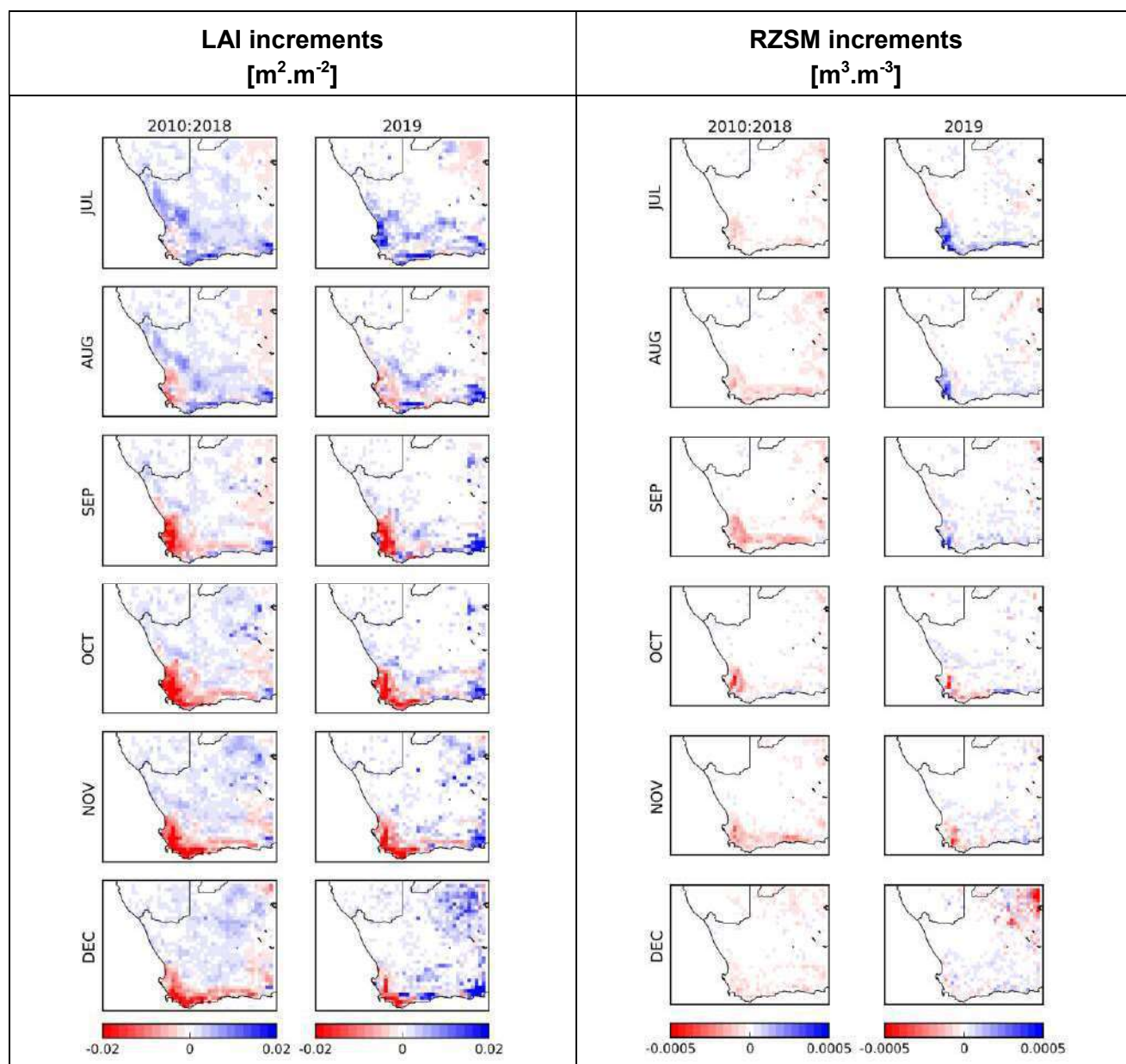


Figure 67: Monthly maps over Southern Africa from July to December of LAI (1st column), root-zone soil moisture (2nd column) increments: averages over 2010–2018 (left), and for 2019 (right).

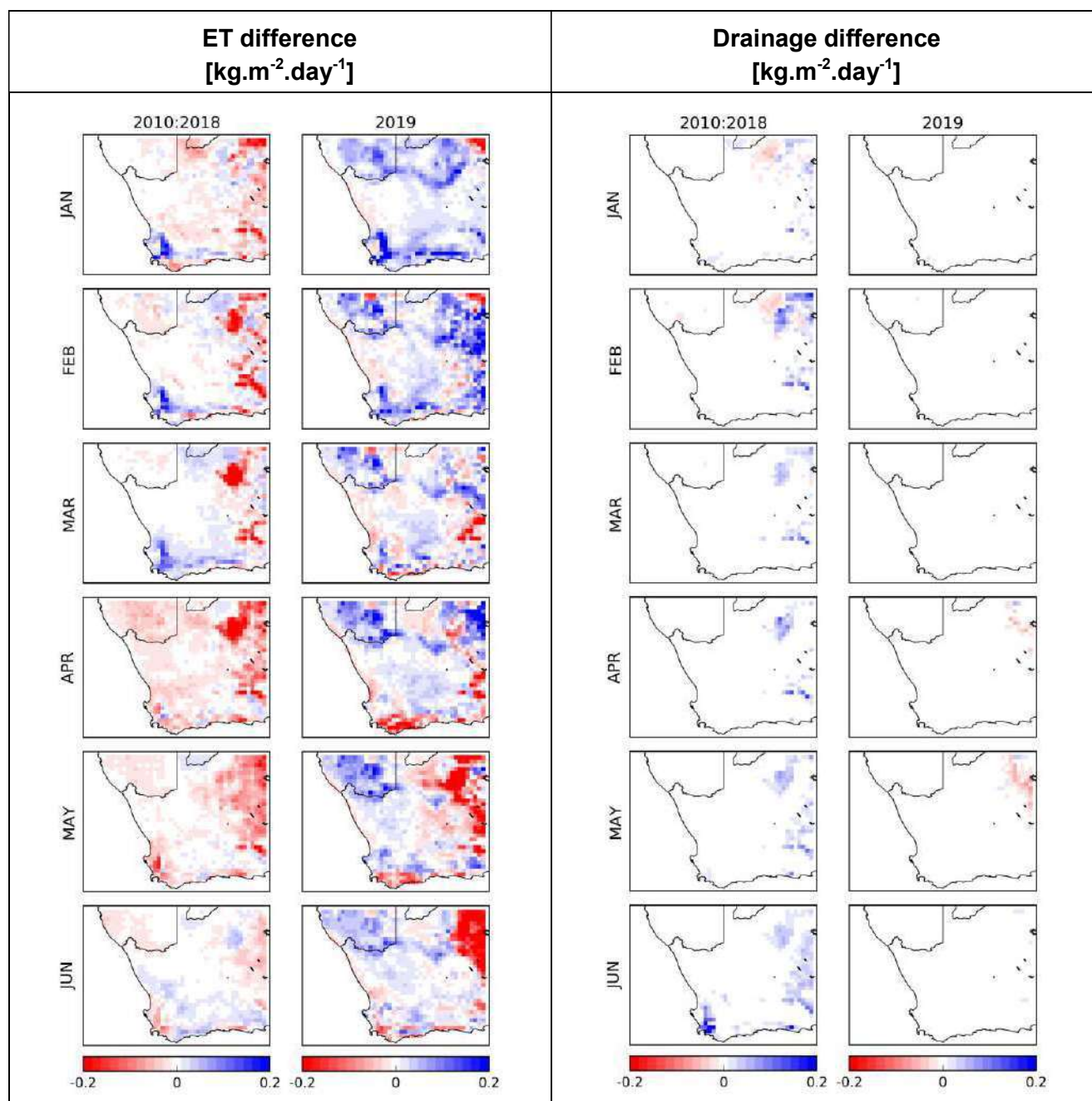


Figure 68: Monthly maps over Southern Africa from January to June of the differences (Analysis-Model) for evapotranspiration (ET, 1st column) and drainage fluxes (2nd column): averages over 2010–2018 (left), and for 2019 (right).

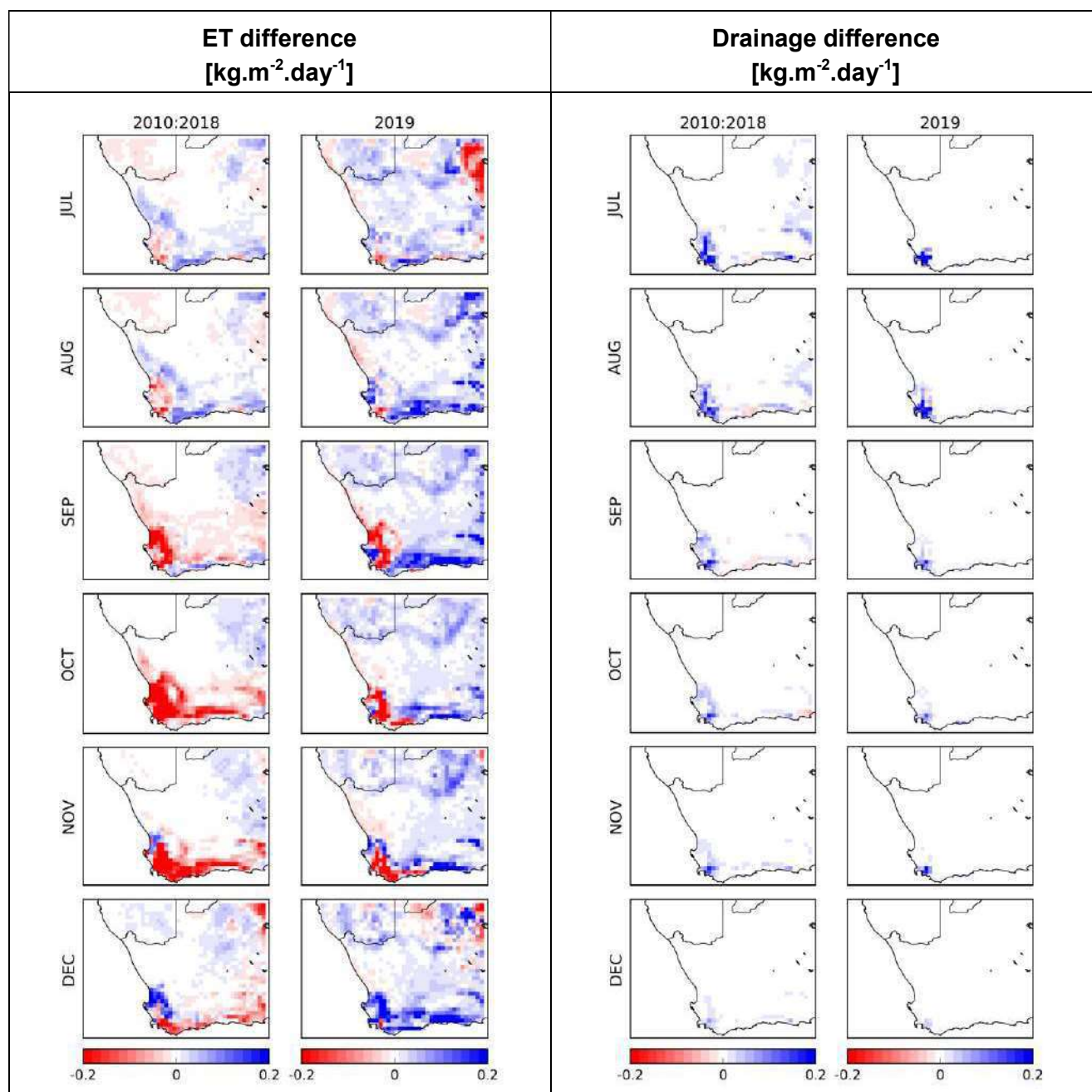


Figure 69: Monthly maps over Southern Africa from July to December of the differences (Analysis-Model) for evapotranspiration (ET, 1st column) and drainage fluxes (2nd column): averages over 2010–2018 (left), and for 2019 (right).

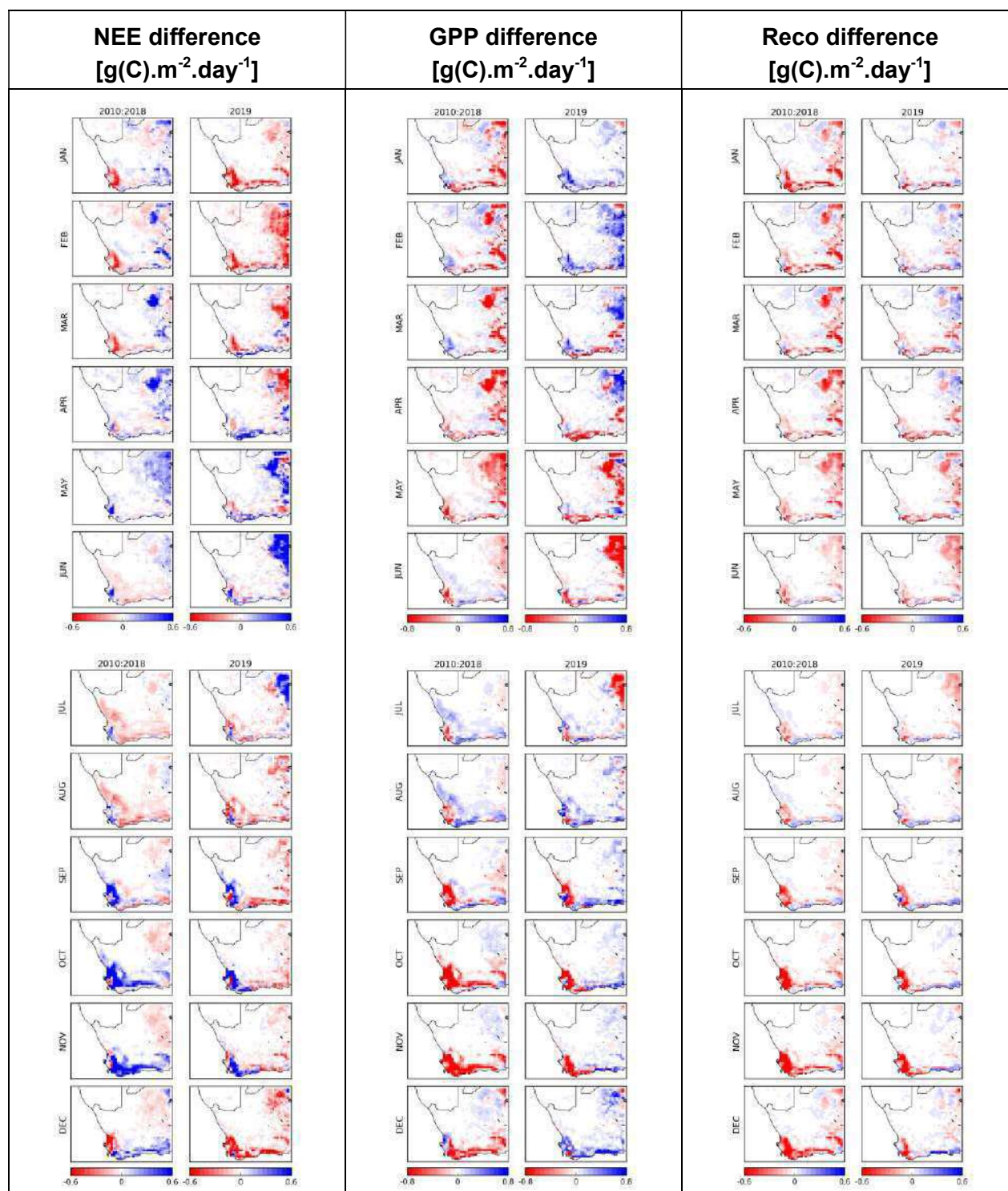


Figure 70: Monthly maps over Southern Africa from January to December of the differences (Analysis-Model) for NEE (1st column), GPP (2nd column) and Reco fluxes (3rd column): averages over 2010–2018 (left), and for 2019 (right).

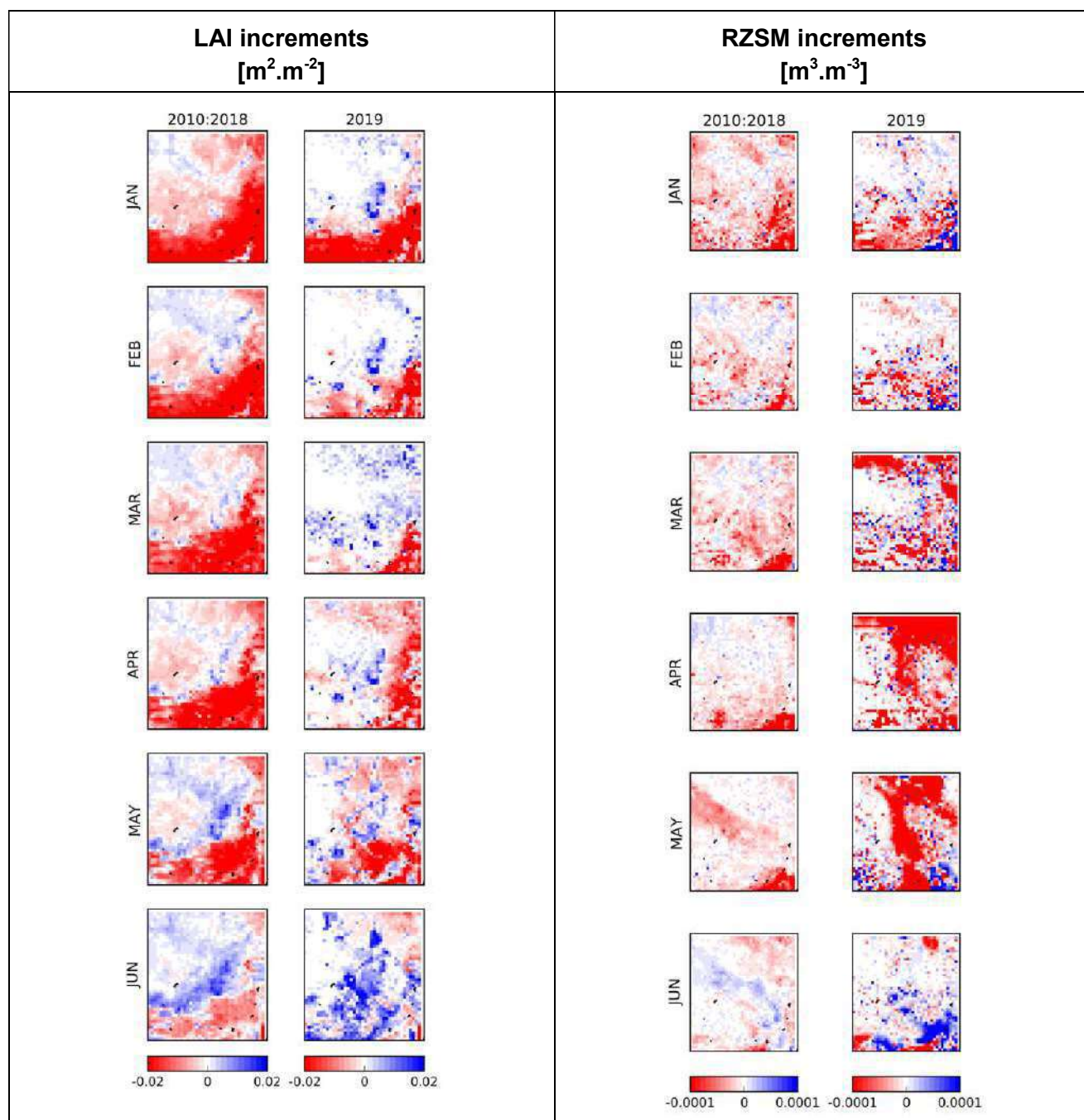


Figure 71: Monthly maps over the Murray-Darling basin from January to June of LAI (1st column), root-zone soil moisture (2nd column) increments: averages over 2010–2018 (left), and for 2019 (right).

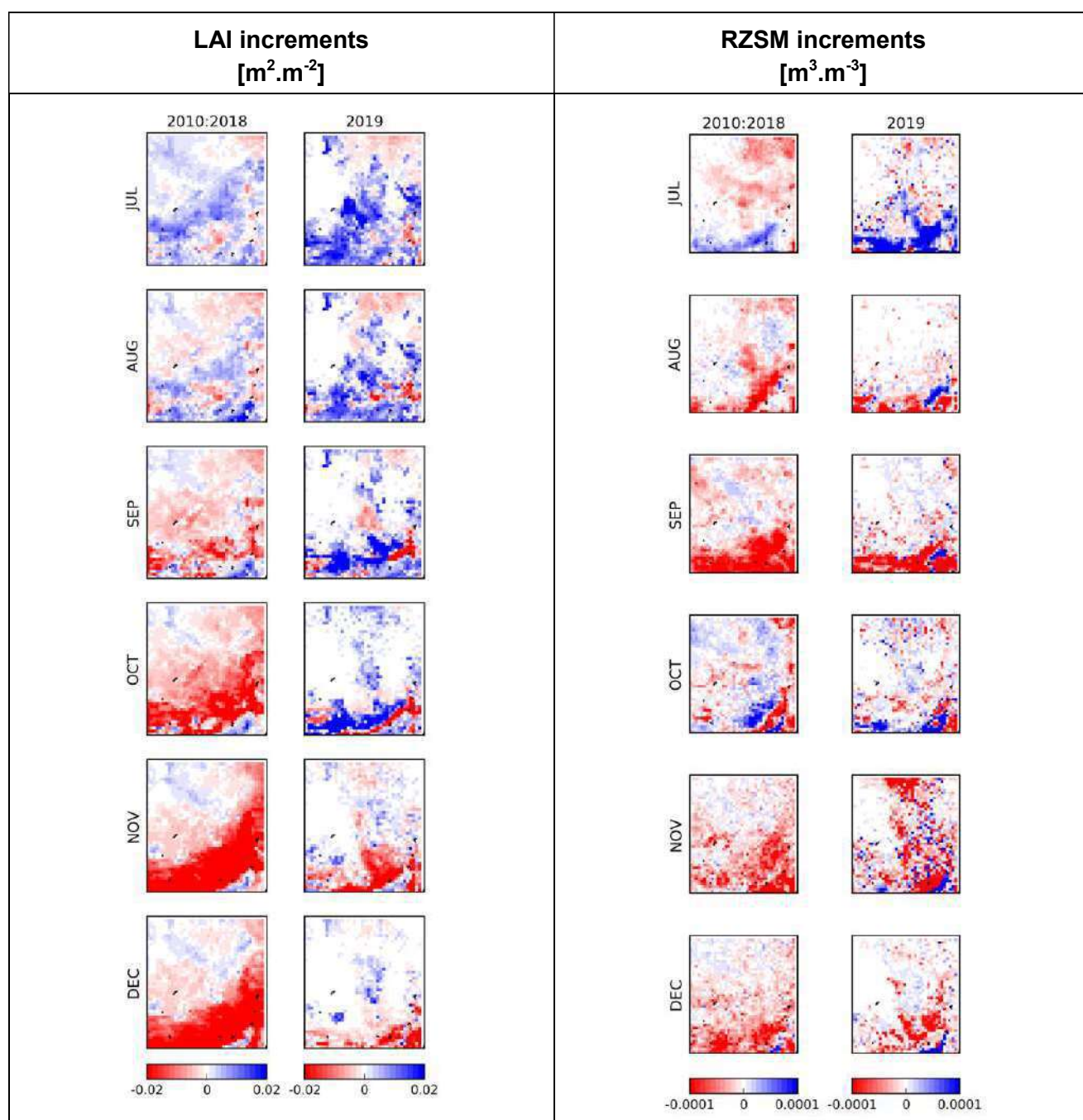


Figure 72: Monthly maps over the Murray-Darling basin from July to December of LAI (1st column), root-zone soil moisture (2nd column) increments: averages over 2010–2018 (left), and for 2019 (right).

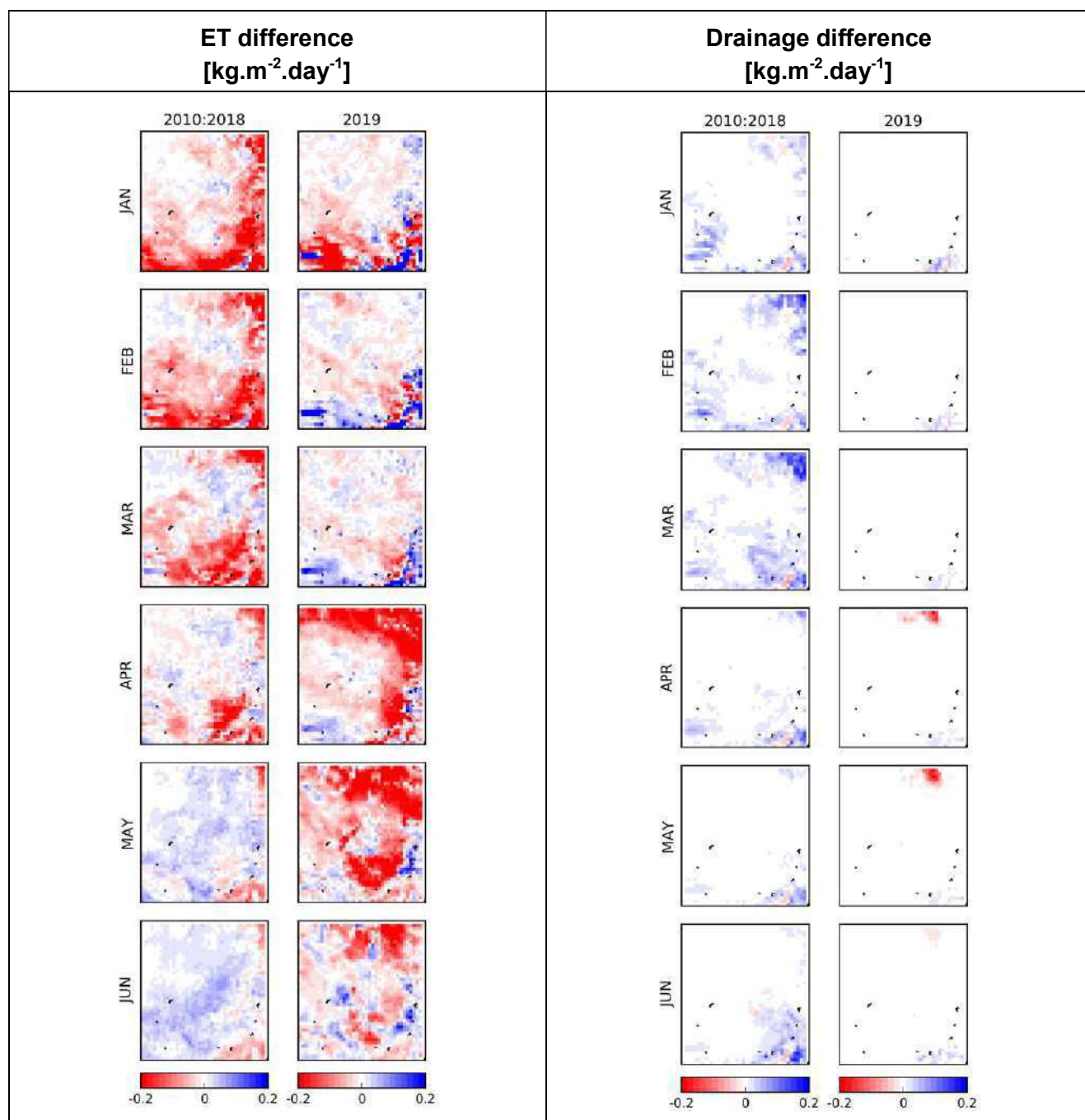


Figure 73: Monthly maps over the Murray-Darling basin from January to June of the differences (Analysis-Model) for evapotranspiration (ET, 1st column) and drainage fluxes (2nd column): averages over 2010–2018 (left), and for 2019 (right).

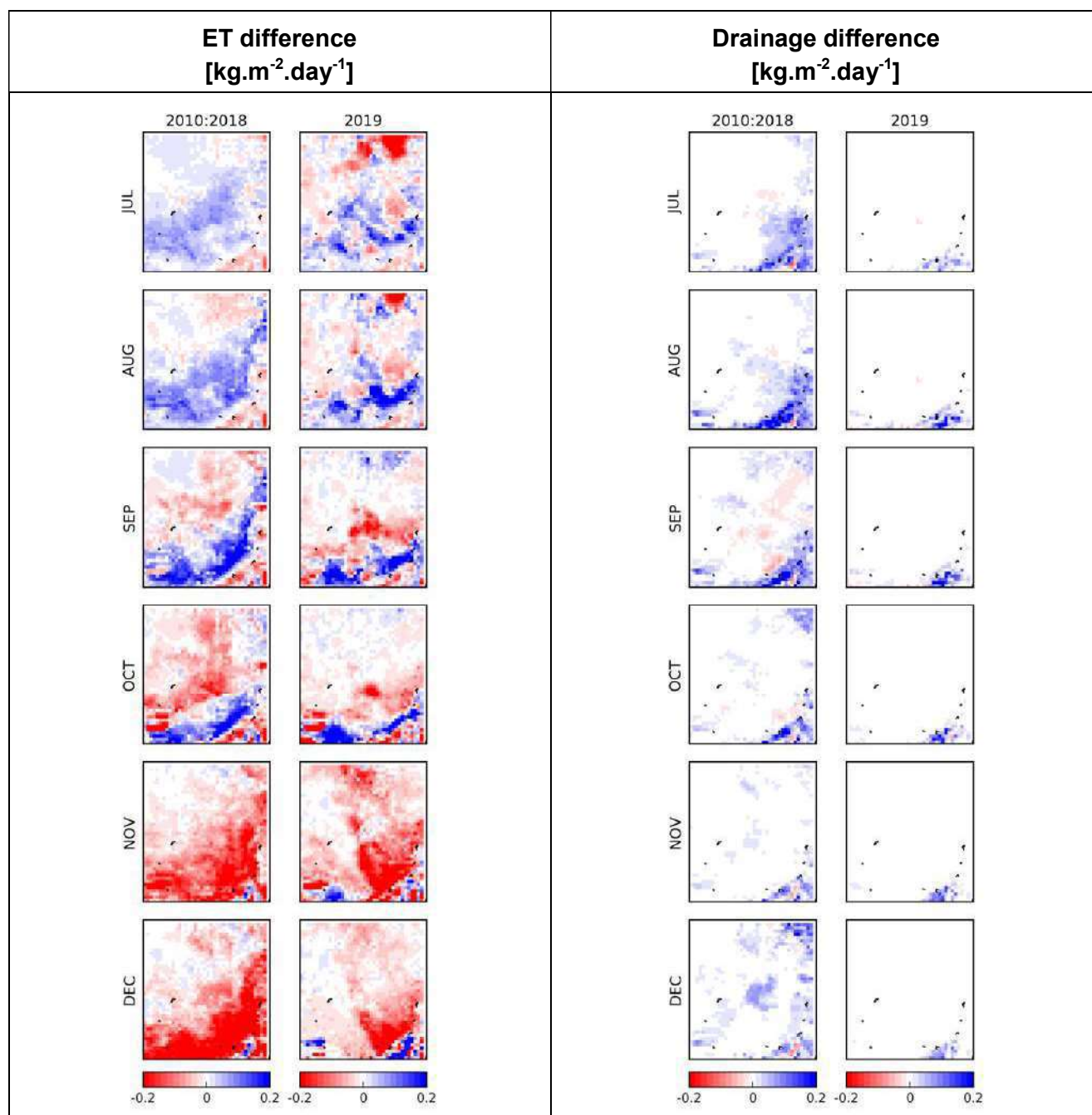


Figure 74: Monthly maps over the Murray-Darling basin from July to December of the differences (Analysis-Model) for evapotranspiration (ET, 1st column) and drainage fluxes (2nd column): averages over 2010–2018 (left), and for 2019 (right).

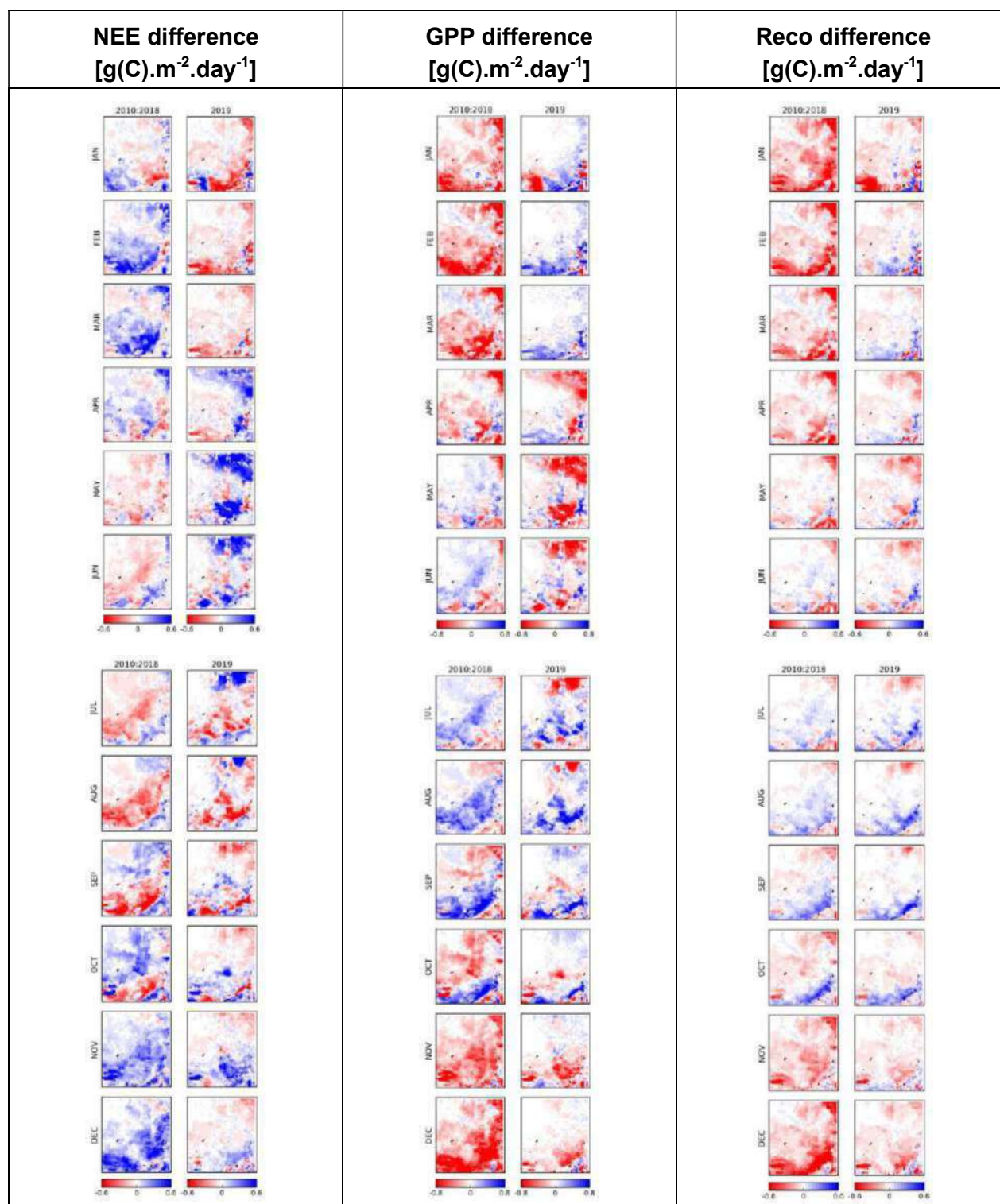


Figure 75: Monthly maps over the Murray-Darling basin from January to December of the differences (Analysis-Model) for NEE (1st column), GPP (2nd column) and Reco fluxes (3rd column): averages over 2010–2018 (left), and for 2019 (right).

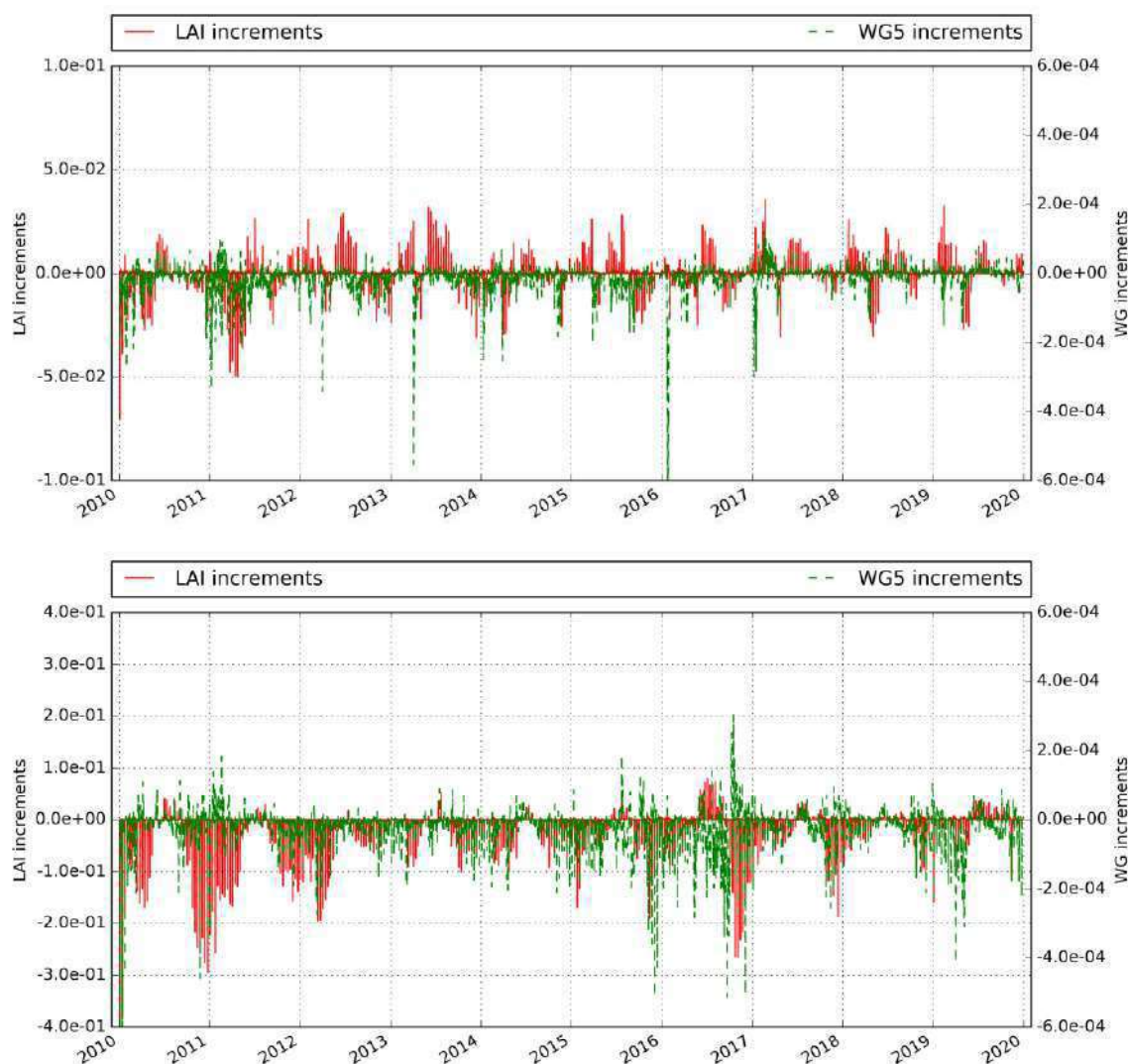


Figure 76: RZSM and LAI mean increments which result from the assimilation of both SWI-001 and LAI observations over Southern Africa (top) from 2010 to 2019, over the Murray-Darling basin (bottom) from 2010 to 2019.

Over Southern Africa, a striking feature is the marked impact of the assimilation over the cropland area around Cape Town. From January to March, ET is enhanced by the assimilation (Figure 68). This enhancement of plant growth by integrating observations into the model could be related to irrigation, which is not represented in the model simulations. On the other hand, ET is reduced from September to November (Figure 69) and this could be an indication of crop harvest, not represented in the model simulations. The smaller ET

values are related to negative LAI increments (Figure 67) resulting in smaller LAI values (Figure 5).

Over the Murray-Darling basin, marked positive LAI increments are observed in 2019 close to the Murray river in September and October (deep blue areas in the southern part of the domain in Figure 72). They result in larger LAI values in the analysis with respect to the open-loop simulation as observed in the right column of Figure 7. These areas correspond to irrigated areas as shown by the irrigation map of the Murray-Darling basin: <http://www.bom.gov.au/water/nwa/2016/mdb/regiondescription/geographicinformation.shtml>. Consistent with the positive LAI increments in Figure 72, the assimilation tends to increase ET over these areas in September and October (Figure 74). In the mountainous areas of the south-east, ET is decreased in January, February (Figure 73) and December (Figure 74), consistent with the smaller LAI in Figure 6. Overall, the assimilation tends to increase the drainage flux (Figure 73 and Figure 74). The impact of the assimilation on drainage is smaller in 2019 than for previous years because very dry conditions prevailed in 2019 and drainage is small in dry conditions. The same contrasting patterns in 2019 as for ET are observed for carbon fluxes (Figure 75).

Overall, Figure 76 shows that LAI and RZSM increments are rather small with respect to previous years for both Southern Africa and Murray-Darling basin.

Over the Murray-Darling basin, RZSM increments (either positive or negative values) after July 2015 are more pronounced than from 2010 to July 2015 (Figure 76). This coincides with the very large increase in the number of ASCAT observations used in the SWI algorithm, related to the use of METOP-B data in addition to METOP-A data. Over this area, the number of observations used in the SWI can be multiplied by a factor of 3 or more (Figure 86).

9.2 TRANSITION BETWEEN SPOT-VGT AND PROBA-V

The impact on analyzed LAI of transitioning from SPOT-VGT to PROBA-V is rather small (Figure 77). However, PROBA-V scores are nearly systematically better than those for SPOT-VGT during the dry season from May to August over Southern Africa, and from December to May over the Murray-Darling basin.

For SA (Figure 78), a very large increase in bias is observed for PROBA-V, of about 0.04 for both Southern Africa and for the Murray-Darling basin. The SA SDD score is nearly systematically better for SPOT-VGT. While correlation is better for PROBA-V over the Murray-Darling basin, the opposite result is found for Southern Africa.

It must be noticed that changes in LAI and SA scores over both areas could also be influenced by the marked trend in LAI and SA from 2010 to 2019 (Figure 23).

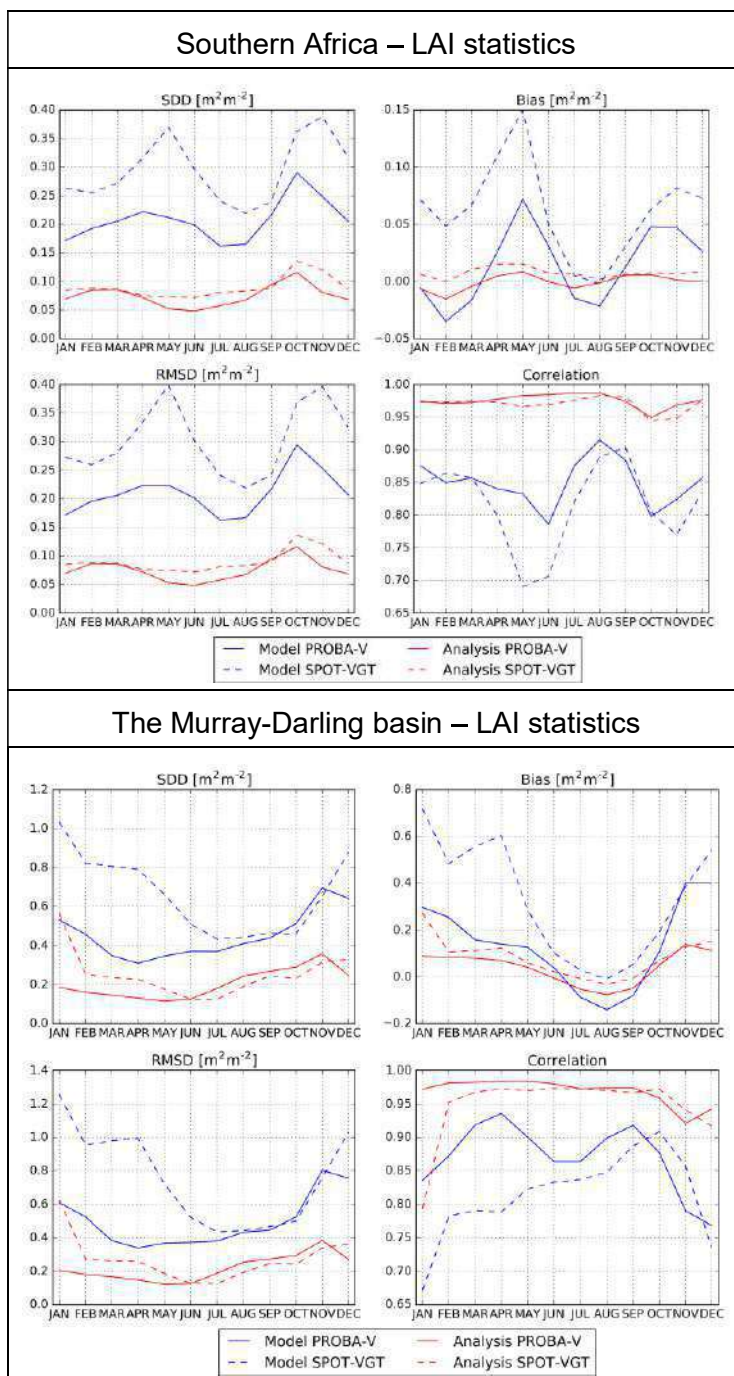


Figure 77: LAI scores for the time periods of SPOT-VGT observations over Southern Africa (top) (2010-2013, dashed lines) and the Murray-Darling basin (bottom) (2010-2013, dashed lines) and of PROBA-V observations (2015-2019, solid lines). Model performances are in blue and analysis performances are in red w.r.t. the appropriate observations. [NB: 2014 was not considered since it was the year of transition between the two instruments].

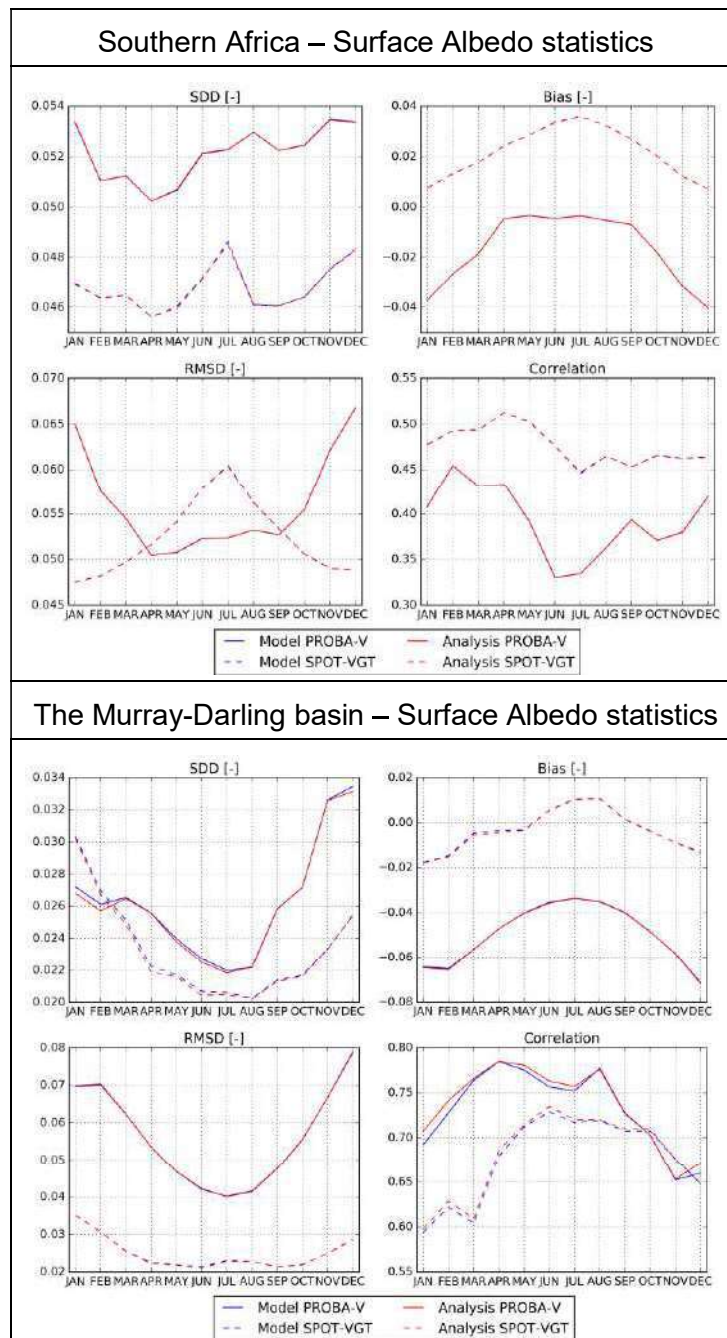


Figure 78: SA scores for the time periods of SPOT-VGT observations over Southern Africa (top) (2010-2013, dashed lines) and the Murray-Darling basin (bottom) (2010-2013, dashed lines) and of PROBA-V observations (2015-2019, solid lines). Model performances are in blue and analysis performances are in red w.r.t. the appropriate observations. [NB: 2014 was not considered since it was the year of transition between the two instruments].

9.3 LAI VERSION 1 (GEOV1) vs. LAI VERSION 2 (GEOV2)

A comparison between the GEOV2-RT6 and the GEOV1 NRT 1km x 1km LAI products was performed. The GEOV2-RT6 is a final consolidated as created by the LAI algorithm version 2 [CGLOPS1_ATBD_LAI1km-V2]. On the other hand, GEOV1 corresponds to the version 1 of algorithm, produced in NRT [GIOGL1_ATBD_LAI1km-V1]. Over Southern Africa (Figure 79) the GEOV1 RMSD scores are systematically better than the GEOV2 RMSD scores, for both model and analysis simulations. For all years from 2010 to 2019, the GEOV2 RMSD for LAI analysis is +53 % to +87 % larger than the RMSD of GEOV1. For the open-loop RMSD, the difference is smaller and ranges from +2 % to +7 %. The scores in 2019 tend to be better than for previous years.

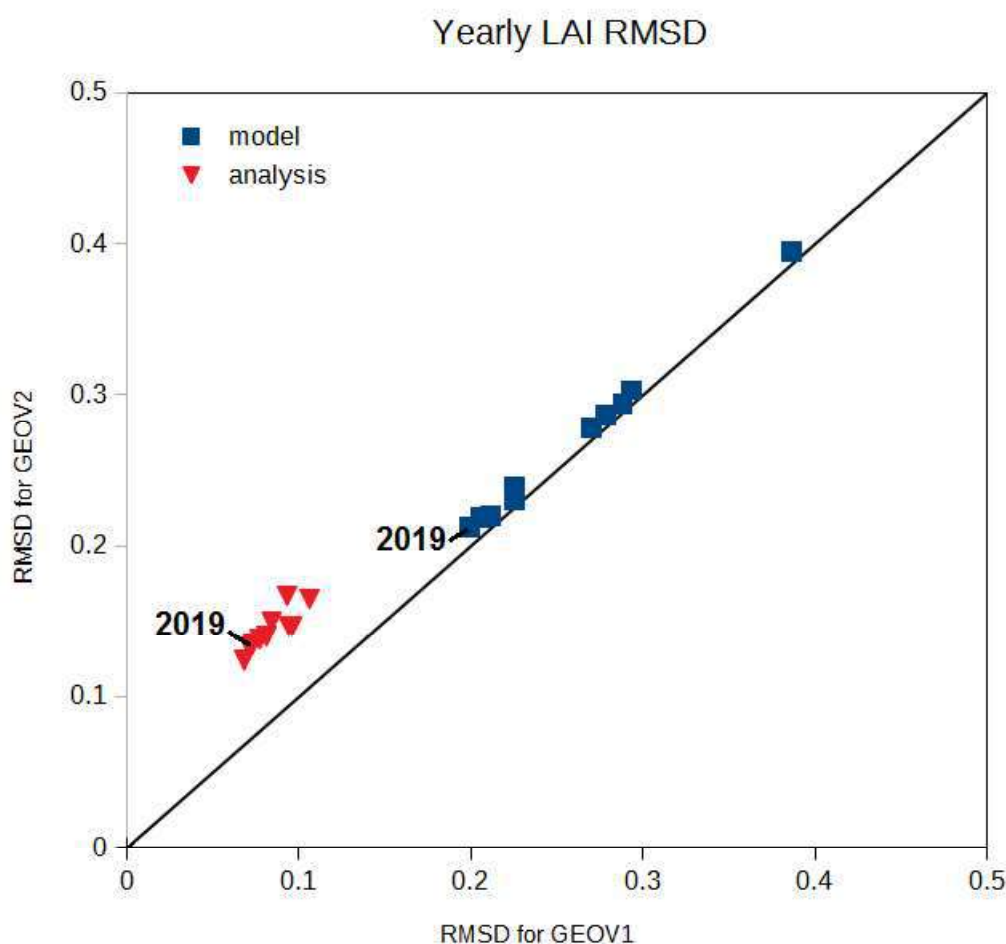


Figure 79: LAI GEOV2 vs. GEOV1 yearly RMSD score over Southern Africa for each year from 2010 to 2019, in m^2m^{-2} . Year 2019 is indicated.

The same comparison was made for the Murray-Darling basin (Figure 80). Contrary to Southern Africa, GEOV1 and GEOV2 RMSD scores are not very different. The GEOV1 LAI analysis RMSD is not markedly better than GEOV2 as over Southern Africa. On the contrary, the GEOV2 RMSD for LAI analysis is -22 % smaller than for GEOV1

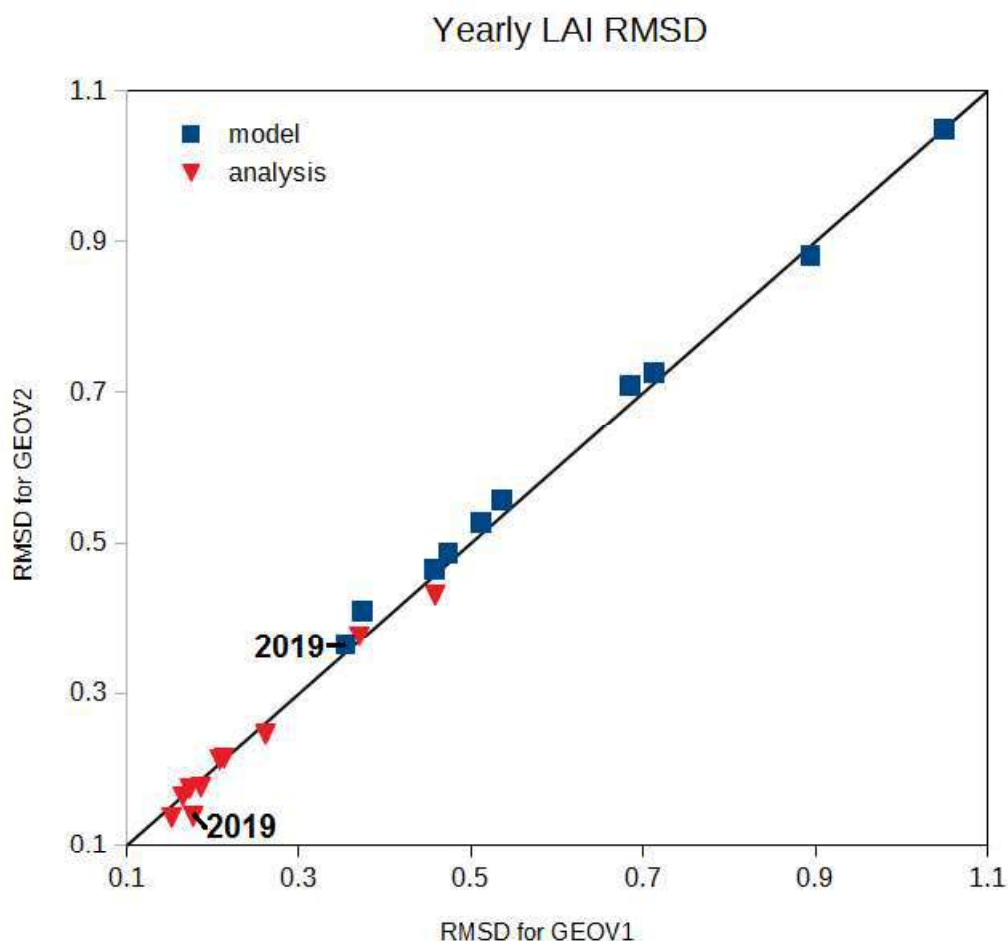


Figure 80: LAI GEOV2 vs. GEOV1 yearly RMSD score over the Murray-Darling basin for each year from 2010 to 2019, in m^2m^{-2} . Year 2019 is indicated.

9.4 ACCURACY ASSESSMENT

Using LDAS analysis simulations, it is possible to assess the accuracy of the observations by computing the RMSD and the relative RMSD and compare them to the user requirements of the products (e.g. GCOS accuracy requirements, based on RMSD). This was made for LAI and FAPAR over Southern Africa (Figure 81) and over the Murray-Darling basin (Figure 82). If the analysis simulation is considered as the “truth”, or at least the “reference”, RMSD between the observations and the analysis values can be used as an indicator of the observations accuracy. GCOS requirements are defined as (see GCOS document N°154, December 2011, on https://library.wmo.int/opac/doc_num.php?explnum_id=3710):

- LAI accuracy: max (20%,0.5)
- FAPAR accuracy: max (10%,0.05)

RMSD or relative RMSD values lower than the GCOS accuracy thresholds indicate that GCOS accuracy requirements are met. However, higher values do not mean that GCOS accuracy requirements are not met as RMSD incorporates model errors in addition to satellite product errors. In this case, one could consider that GCOS requirements may not be made.

RMSD values are considered for low LAI and FAPAR values (≤ 2.5 and ≤ 0.5 , respectively).

Relative RMSD values are considered for high LAI and FAPAR values (> 2.5 and > 0.5 , respectively).

Note: GCOS requirements were updated for LAI in 2016 (see GCOS document N°200, https://library.wmo.int/doc_num.php?explnum_id=3417) as:

- LAI accuracy: max (15%)

For the sake of consistency with our previous reports, the results for LAI presented below follow the original GCOS 2011 thresholds.

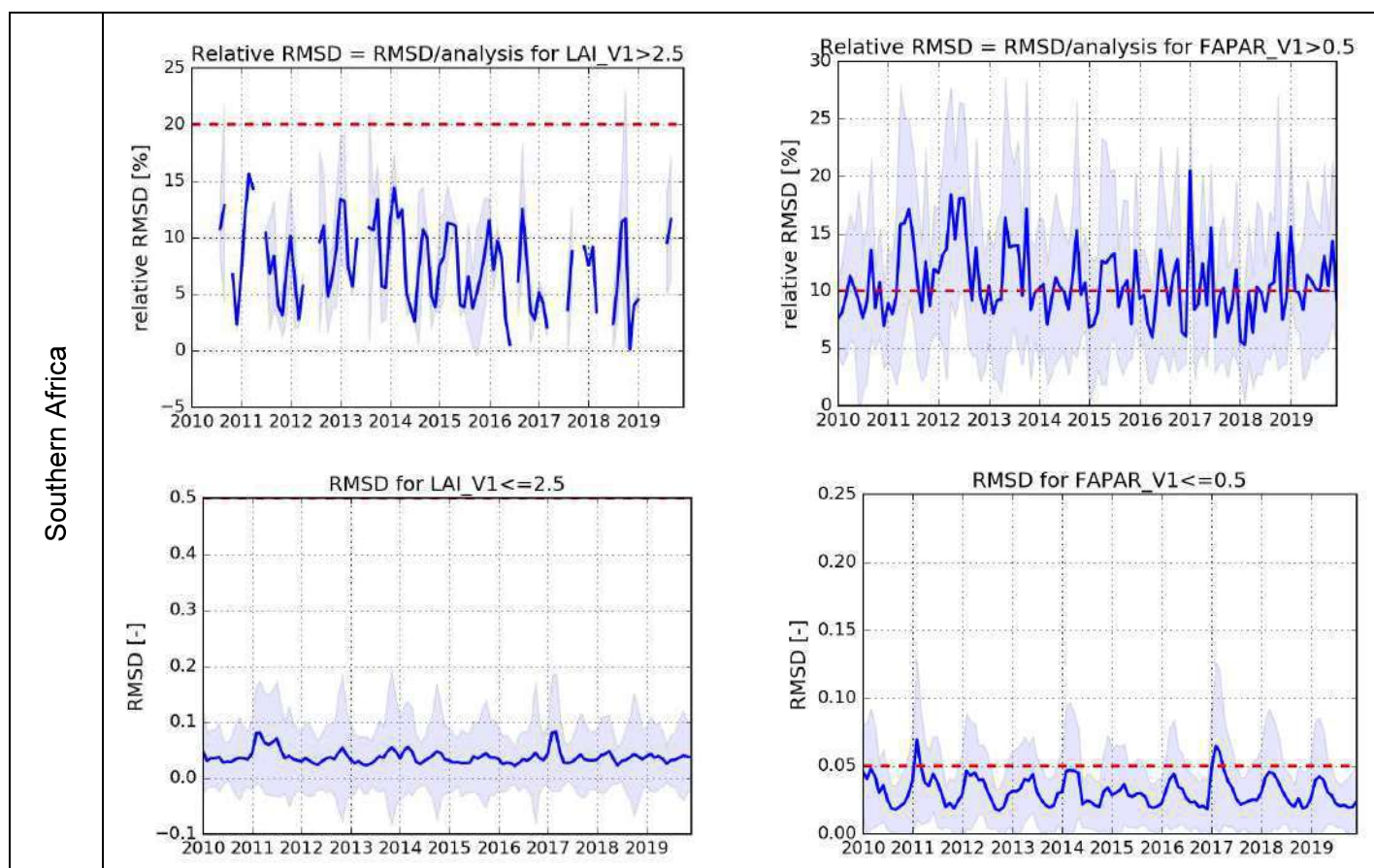


Figure 81: Relative analysis RMSD (RMSD divided by value) (top) and analysis RMSD (bottom) of LAI (left) and FAPAR (right) on average over Southern Africa. Dashed red line indicates the target accuracies: max(20%,0.5) for LAI and max(10%,0.05) for FAPAR. Shaded areas indicate 1 standard deviation.

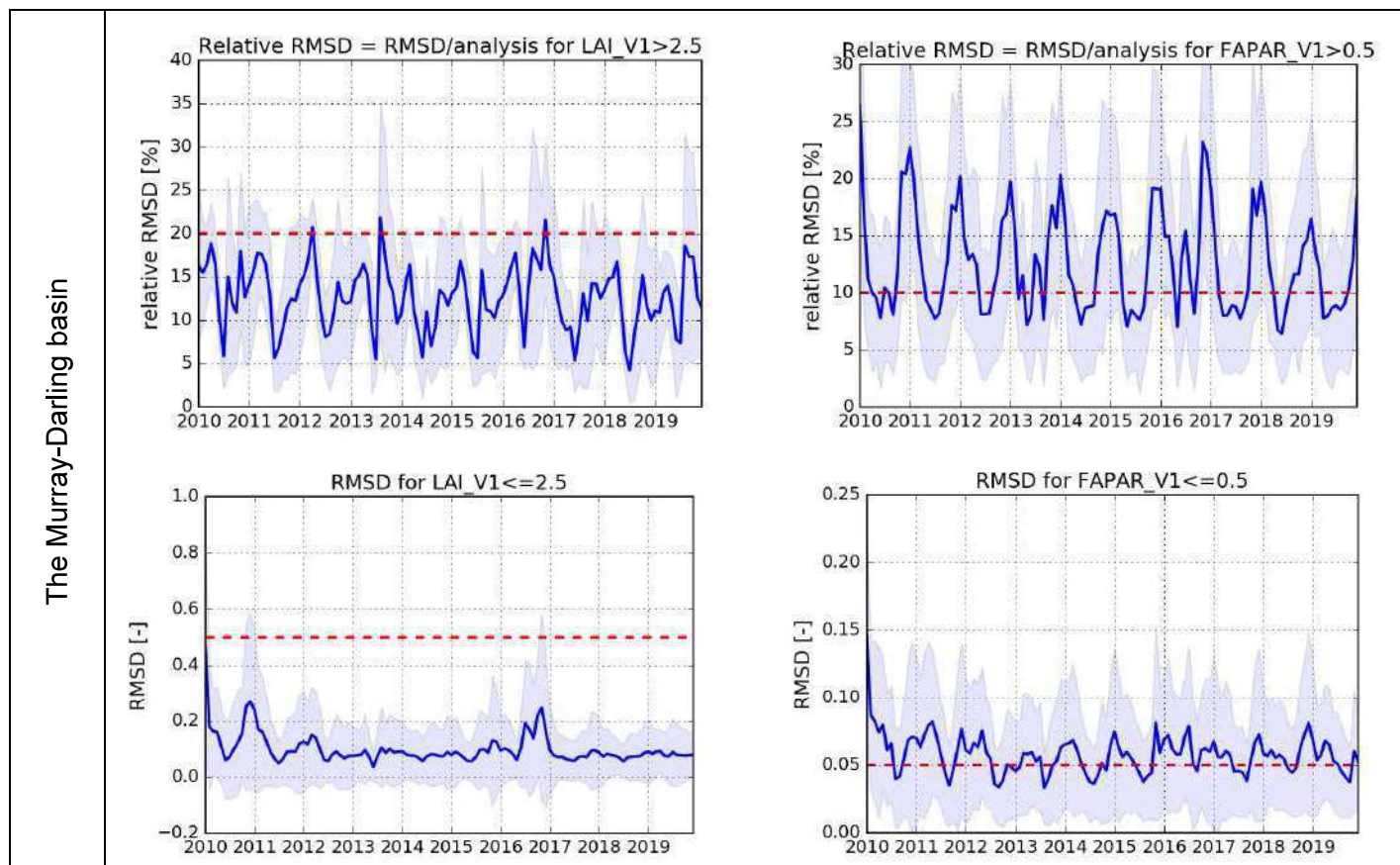


Figure 82: Relative analysis RMSD (RMSD divided by value) (top) and analysis RMSD (bottom) of LAI (left) and FAPAR (right) on average over the Murray-Darling basin. Dashed red line indicates the target accuracies: max(20%,0.5) for LAI and max(10%,0.05) for FAPAR. Shaded areas indicate 1 standard deviation.

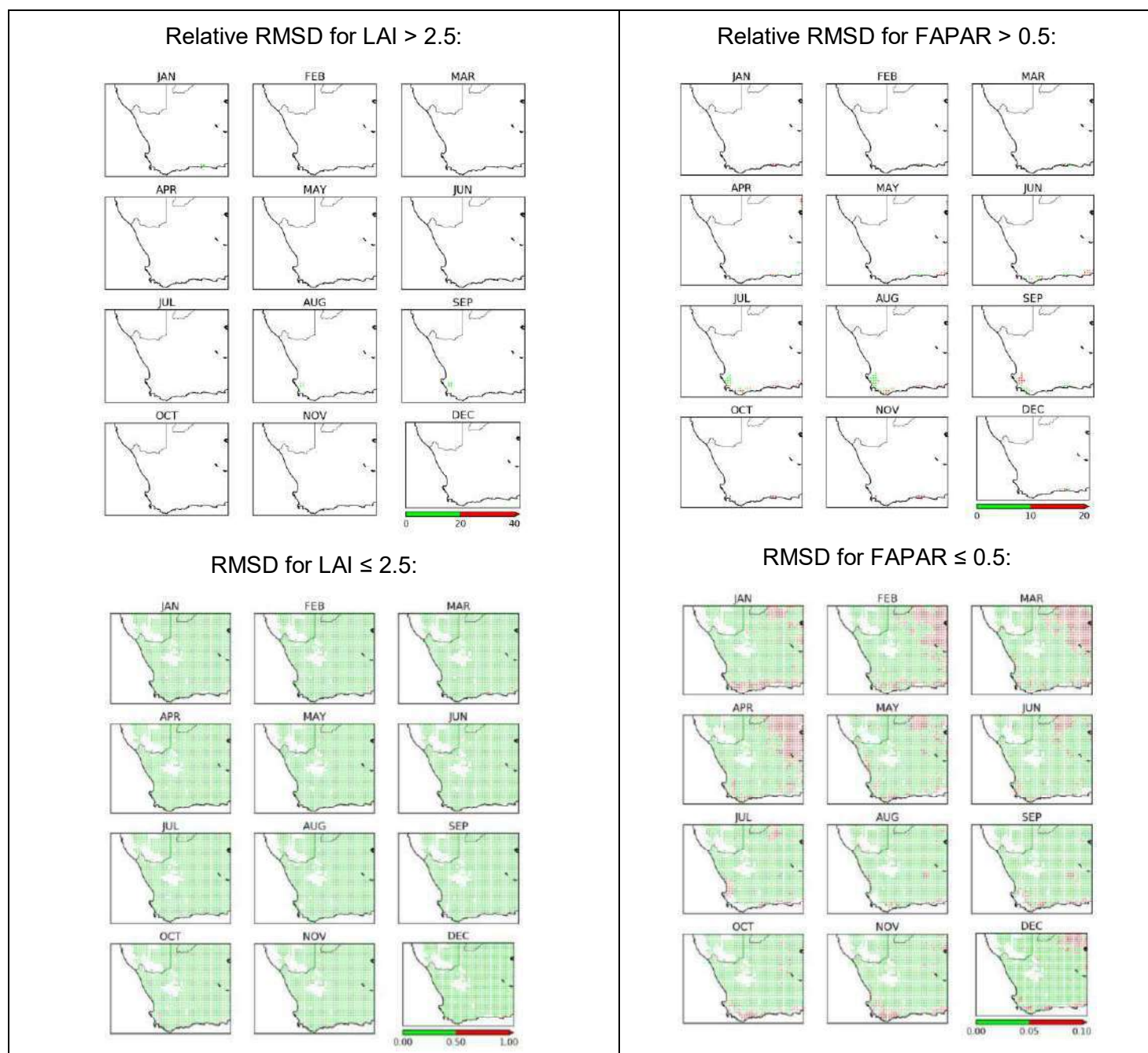


Figure 83: Maps over Southern Africa showing (in green) where GCOS accuracy requirements could be met (LAI: max(20%,0.5), FAPAR: max(10%,0.05)) or may have not be met (in red) for 2019.

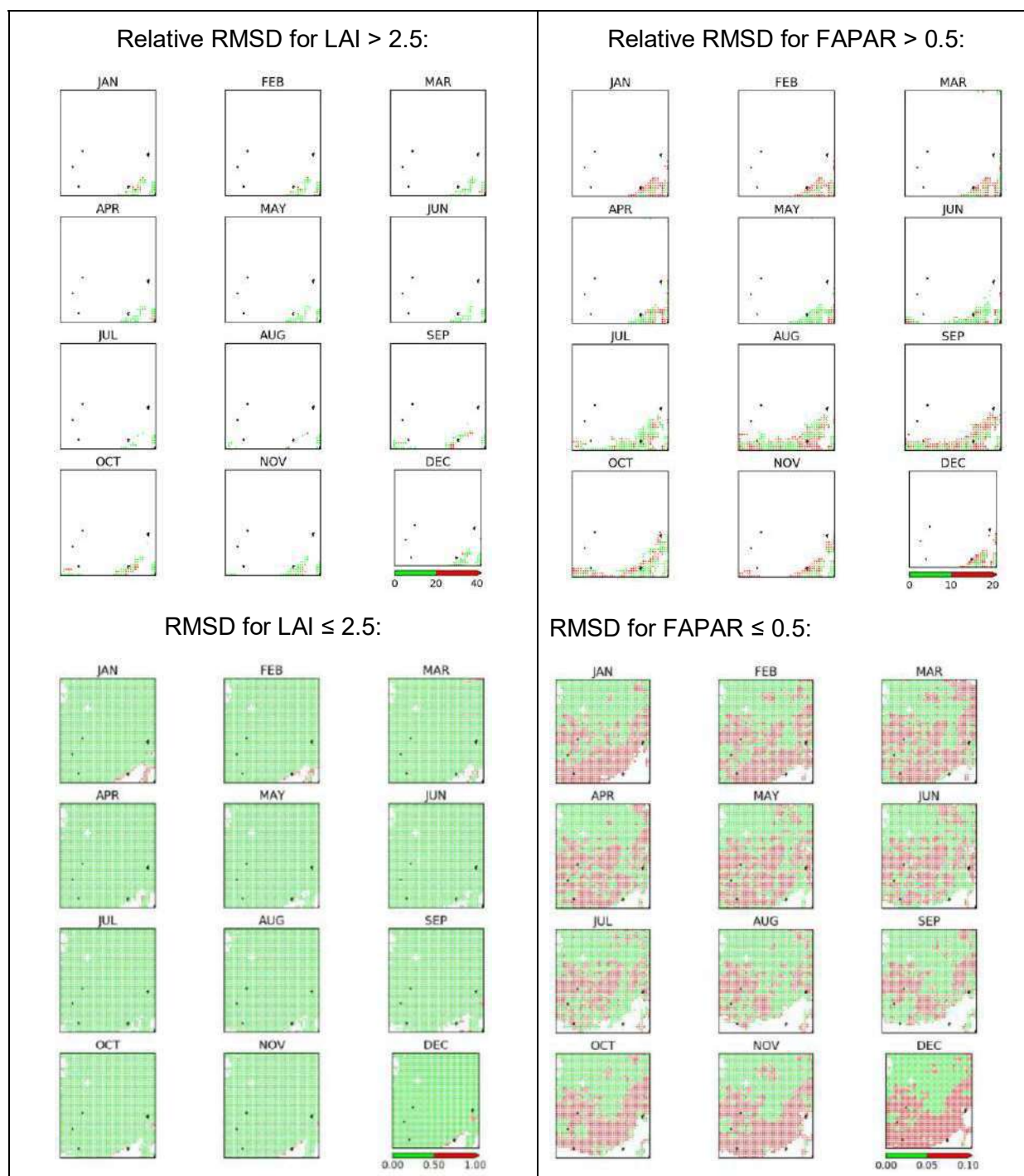


Figure 84: Maps over the Murray-Darling basin showing (in green) where GCOS accuracy requirements could be met (LAI: max(20%,0.5), FAPAR: max(10%,0.05)) or may have not be met (in red) for 2019.

On Figure 83, maps of LAI and FAPAR accuracy for 2019 show that for low product values, the GCOS accuracy criterion is met more often for LAI than for FAPAR. The latter finding is further illustrated in Figure 81: while the mean RMSD for $\text{LAI} \leq 2.5$ is always smaller than 0.5, the mean RMSD for $\text{FAPAR} \leq 0.5$ can be larger than 0.5. High values of LAI and FAPAR are not frequent over this area. Figure 81 shows that the FAPAR relative RMSD is often larger than the 10 % threshold value, especially at summertime. More often than not, the LAI relative RMSD is smaller than the 20 % threshold value.

Over the Murray-Darling basin, Figures 82 and 84 shows that low LAI values are generally more accurate than low FAPAR values, consistent with what is observed over Southern Africa. The highest LAI and FAPAR values are observed from July to September (Figure 7 and Figure 15, respectively). Figure 84 shows that fractional areas of accurate high LAI and FAPAR values are more or less equivalent over the Murray-Darling basin as a whole. However, Figure 82 shows that the mean LAI relative RMSD is often smaller than the 20% threshold. This is not the case for high FAPAR values, with mean relative RMSD values often larger than 10%.

9.5 NUMBER OF OBSERVATIONS

The following maps show the number of dates per year when observations are available for assimilation for the SWI-001 product only. Until 20 July 2015, only METOP-A observations were available. Now both METOP-A and METOP-B are operating and more observations are available. This difference in the number of available observations can introduce some errors in the interpretation of the statistics because they might not be representative of the same area. Contrasting values of the additional fraction of available data may lead to give more weight to the areas presenting the largest increase in available data. Over Southern Africa (Figure 85), the northern part of the domain is covered from 2016 onward more than twice more than from 2010 to 2014. The number of observations does not increase that much in other parts of the domain. Over the Murray-Darling basin (Figure 86), some parts are covered more than twice, especially at the western part of the domain, where areas were completely missing before 2015.

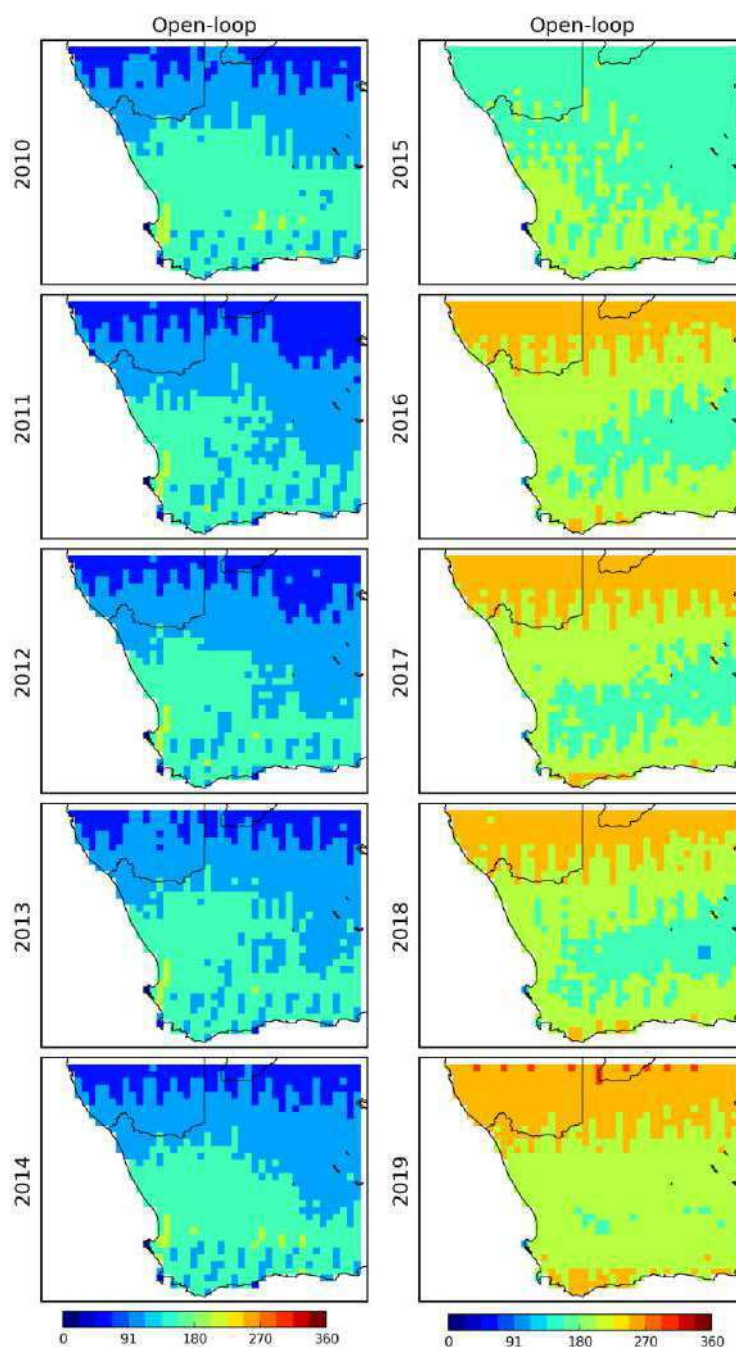


Figure 85: Annual number of SWI-001 observations available over Southern Africa (only METOP-A until July 20, 2015; after July 21, 2015 both METOP-A and B are used)

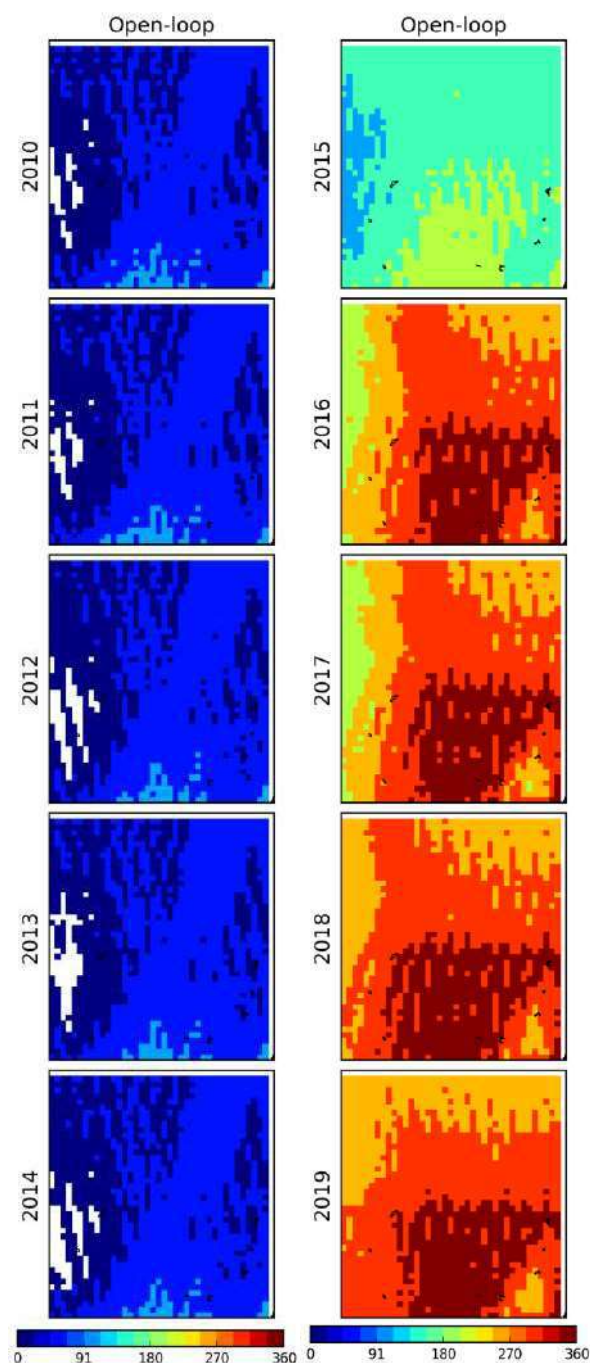


Figure 86: Annual number of SWI-001 observations available over the Murray-Darling basin (only METOP-A until July 20, 2015; after July 21, 2015 both METOP-A and B are used)

10 CONCLUSIONS

This document summarizes the results of the cross-cutting quality monitoring of the Copernicus Global Land Service for the period from 1st January 2019 to 31th December 2019. Both LAI and SWI-001 products were integrated into the ISBA-A-gs LSM using a LDAS platform over Southern Africa and over the Murray-Darling basin. An extensive analysis of the LAI, FAPAR, SA, SWI-001, and LST products was performed. Scores were obtained monthly (Figure 10, Figure 11, Figure 17, Figure 18, Figure 24, Figure 25, Figure 38, Figure 39, Figure 58, Figure 59, Figure 60, Figure 61) for 2019 and for previous years (the period from 2010 to 2018).

For **LAI**, over both Southern Africa and the Murray-Darling basin, the scores tend to present better values during the dry spells of 2019 than during previous years from 2010 to 2018. Overall, the RMSD scores of GEOV2-RT6 and GEOV1 are comparable in 2019. The impact on analyzed LAI of transitioning from SPOT-VGT to PROBA-V is small. Over Southern Africa, the seasonality of the LAI bias is caused by a delayed peak LAI date in the model simulations, and GEOV2-RT6 tends to present larger RMSD values than GEOV1 from 2010 to 2019.

For **FAPAR**, over both Southern Africa and the Murray-Darling basin, the scores tend to present slightly better values during the dry spells of 2019 than during previous years from 2010 to 2018. For both areas, the largest variability of simulated FAPAR scores is observed during the dry season, at the end of the plant senescence phase (e.g. June for Southern Africa and December for the Murray-Darling basin). Over the Murray-Darling basin, the same behavior is observed for the analysis FAPAR. FAPAR being a radiation variable, low FAPAR values are quite sensitive to illumination conditions and to soil directional assumptions (Claverie et al., 2013).

For **SA**, a striking result is that a large increase in the mean bias value is observed at the transition from SPOT-VGT to PROBA-V in May 2014, of about 0.02 for both Southern Africa and the Murray-Darling basin. There is a clear discontinuity in the SA time series, not observed for LAI nor for FAPAR. Contrary to LAI and FAPAR, the SA scores in 2019 do not always present better values than during the 2010-2018 reference period of time. Finally, the number of available observations is smaller than for LAI and FAPAR over the Murray-Darling basin.

For **SWI-001**, the impact of the seasonal SSM CDF-matching performed prior the assimilation is particularly striking for Southern Africa. Without a seasonal CDF-matching, the original SSM information would be misleading over Southern Africa. This is not observed over the Murray-Darling basin. Contrary to LAI and FAPAR products SSM scores in 2019 do not present significantly better values than for previous years from 2010 to 2018 and the

analyzed SSM does not present a reinforcement of the drought signal over Southern Africa with respect to the modelled SSM.

For **LST**, the model tends to underestimate LST, especially at daytime. The mean monthly cold bias observed at noon is particularly large (down to -12°C) at summertime in 2019 over both Southern Africa and the Murray-Darling basin. Over the Murray-Darling basin, the mean yearly bias is about -8°C in 2019 (a dry year), against -4°C in 2010 (a wet year). This result shows that daytime LST biases are more pronounced in dry conditions. Possible causes of the spatial, diurnal and seasonal patterns of the LST bias are hot-spot phenomenon (more sunlit than shaded elements are seen by the satellite), biases in the incoming solar and infrared radiation data used to force the model. When the assimilation significantly reduces the simulated LAI, the LST noon bias is slightly reduced in the analysis, for both Southern Africa and the Murray-Darling basin. Also, the assimilation tends to improve the temporal correlation of the simulated and observed LST. This shows the consistency of the observed LST with the observed LAI.

LDAS analyses were also used to assess the accuracy of LAI and FAPAR observations, with respect to GCOS requirements. Using the analysis RMSD score as a proxy to assess the LAI and FAPAR products accuracies, it is showed that small values of LAI observations tend to meet the GCOS requirements more often than large values of LAI observations and of FAPAR observations, for both Southern Africa and the Murray-Darling basin. Overall, low FAPAR values present more uncertainties than low LAI values.

11 REFERENCES

Albergel, C., S. Munier, D. J. Leroux, H. Dewaele, D. Fairbairn, A. L. Barbu, E. Gelati, W. Dorigo, S. Faroux, C. Meurey, P. Le Moigne, B. Decharme, J.-F. Mahfouf, J.-C. Calvet: Sequential assimilation of satellite-derived vegetation and soil moisture products using SURFEX_v8.0: LDAS-Monde assessment over the Euro-Mediterranean area, *Geosci. Model Dev.*, *Geosci. Model Dev.*, 10, 3889–3912, <https://doi.org/10.5194/gmd-10-3889-2018>, 2017.

Barbu, A., J.-C. Calvet, J.-F. Mahfouf, C. Albergel, S. Lafont, “Assimilation of soil wetness Index and Leaf Area Index into the ISBA-A-gs land surface model: grassland case study”, *Biogeosciences*, 8, 1971-1986, <https://doi.org/10.5194/bg-8-1971-2011>, 2011.

Barbu, A.L., J.-C. Calvet, J.-F. Mahfouf, and S. Lafont: Integrating ASCAT surface soil moisture and GEOV1 leaf area index into the SURFEX modelling platform: a land data assimilation application over Southern Africa, *Hydrol. Earth Syst.*, 18, 173–192, <https://doi.org/10.5194/hess-18-173-2014>, 2014.

Carrer D., J.-L. Roujean, S. Lafont, J.-C. Calvet, A. Boone, B. Decharme, C. Delire, and J.-P. Gastellu-Etchegorry: A canopy radiative transfer scheme with explicit FAPAR for the interactive vegetation model ISBA-A-gs: impact on carbon fluxes, *J. Geophys. Res. Biogeosci.*, 118, <https://doi.org/10.1002/jgrg.20070>, 2013.

Carrer D., C. Meurey, X. Ceamanos, J.-L. Roujean, J.-C. Calvet, and S. Liu: Dynamic mapping of snow-free vegetation and bare soil albedos at global 1 km scale from 10-year analysis of MODIS satellite products, *Remote Sens. Environ.*, 140, 420-432, <https://doi.org/10.1016/j.rse.2013.08.041>, 2014.

Claverie M., E. F. Vermote, M. Weiss, F. Baret, O. Hagolle, and V. Demarez: Validation of coarse spatial resolution LAI and FAPAR time series over cropland in southwest Southern Africa, *Remote Sens. Environ.*, 139, 216-230, <https://doi.org/10.1016/j.rse.2013.07.027>, 2013.

Ermida, S. L., Trigo, I. F., DaCamara, C. C., and Pires, A. C.: A methodology to simulate LST directional effects based on parametric models and landscape properties, *Remote Sens.*, 10, 1114, <https://www.doi.org/10.3390/rs10071114>, 2018.

Faroux, S., A. T. Kaptué Tchuenté, J.-L. Roujean, V. Masson, E. Martin, and P. Le Moigne: ECOCLIMAP-II/Europe: a twofold database of ecosystems and surface parameters at 1 km resolution based on satellite information for use in land surface, meteorological and climate models, *Geosci. Model Dev.*, 6, 563–582, <https://doi.org/10.5194/gmd-6-563-2013>, 2013.

Hersbach H. and D. Dee: “ERA-5 reanalysis is in production”. ECMWF newsletter, number 147, Spring 2016, p.7, 2016

Document-No. CGLOPS1_SQE-CCR

© C-GLOPS Lot1 consortium

Issue: **I1.00**

Date: 13.03.2020

Page: **133 of 134**

(<https://www.ecmwf.int/sites/default/files/elibrary/2016/16299-newsletter-no147-spring-2016.pdf>).

Urraca, R., T. Huld, A. Gracia-Amillo, F.J. Martinez-de-Pison, F. Kaspar, and A. Sanz-Garcia : Evaluation of global horizontal irradiance estimates from ERA5 and COSMO-REA6 reanalyses using ground and satellite-based data, Sol. Energy, 164, 339-354, <https://doi.org/10.1016/j.solener.2018.02.059>, 2018.